ABSTRACT

Title of Document: STRUCTURE TAILORED PROPERTIES AND FUNCTIONALITIES OF ZERO-DIMENSIONAL NANOSTRUCTURES

Yun Tang, Ph.D., 2009

Directed By: Professor Min Ouyang, Department of Physics

The field of nanoscience and nanotechnology has achieved significant progress over last thirty years. Complex nanostructures with tunable properties for novel applications have been successfully fabricated and characterized. In this thesis, I will focus on our recent efforts on precise controlled synthesis of zero-dimensional nanostructures as well as fundamental understanding of the physical behavior of as-synthesized nanostructures. Particularly, three topics are presented: (1) Nanoscale crystallinity engineering: we have achieved nanoscale crystallinity control of noble metal nanoparticles with 100% yield by molecular engineering. We have used silver nanoparticles as example to demonstrate synthetic strategy and importance of such control in nanoscale chemical transformation, fundamental electron and phonon couplings and surface plasmon resonance based biological sensors. Such nanoscale crystallinity engineering provides a new pathway for design of complex nanostructures, tailoring nanoscale electronic and mechanical properties as well as

controlling classical and quantum coupling interactions; (2) Precise control of core@shell nanostructures: we have developed a new universal strategy denoted as intermediated phase assisted phase exchange and reaction (*i*PAPER) to achieve layer-by-layer control of shell components in core@shell structures. Tunable plasmonic, optical and magnetic properties of core@shell structures enabled by our *i*PAPER strategy are further demonstrated. These characterizations are promising for understanding and manipulating nanoscale phenomena as well as assembling nanoscale devices with desirable functionality; and (3) Fundamental spin and structure manipulation of semiconductor quantum dots by hydrostatic pressure. Pressure provides a unique means of modifying materials properties. By measuring dependence of spin dynamics on pressure, we revealed that the spin states of semiconductor quantum dots are very robust. We further provided the first experimental evidence for the existence of a metastable intermediate state before the first-order phase transition of semiconductor quantum dots. Our results are crucial for the future development of quantum information processing based on spin qubits of quantum dots.

STRUCTURE TAILORED PROPERTIES AND FUNCTIONALITIES OF ZERO-DIMENSIONAL NANOSTRUCTURES

By

Yun Tang

Dissertation submitted to the Faculty of the Graduate School of the
University of Maryland, College Park, in partial fulfillment
of the requirements for the degree of
Doctor of Philosophy
2009

Advisory Committee:
Professor Min Ouyang, Chair
Professor Ellen D. Williams
Professor Lourdes G. Salamanca-Riba
Professor YuHuang Wang
Professor Bryan W. Eichhorn

Dedication

To

My Parents Fengjun Tang and Sujie Liu,
My Parents-in-law Fanqing Li and Yingying Zhang,
and My wife Shu Li.

Acknowledgements

First of all, I would like to thank my advisor, Professor Min Ouyang who guided me to achieve the successful completion of my thesis. He has been fully supportive of my research and has given me a lot of freedom, even when I seemed to be not as aggressive as he expected. I always benefit from the discussions with him which will be great helpful to me future research career. His enthusiasm for science has always invigorated me, and I feel that my success is directly linked to his guidance.

I would also like to thank Professor Michael A. Coplan, director of Chemical Physics Program. He has been always available and willing to help throughout my graduate study at Maryland.

I would also like to thank Professor Lourdes G. Salamanca-Riba, from whom I learned most of my knowledge of Transmission Electron Microscope, the essential characterization equipment for my graduate research. I would also like to thank Mr. Tiejun (Tim) Zhang, who is the most knowledgeable person I know on Electron Microscopes and any other scientific equipment. I benefit from his experience.

I would also like to thank all the members in Professor Ouyang Group: Dr. Jiatao Zhang, Mr. Kwan Lee and Mr, Lin Weng for their help whenever I needed.

Table of Contents

List of Tables

List of Figures

Chapter 1: Introduction

1. Nanoscience and Nanotechnology

Nanoscience and nanotechnology have attracted public attentions over thirty years, and are considered to be the next "industrial revolution". There are broad applications, ranging form health, environment to energy and information technology. To most of scientists and engineers, nanoscience and nanotechnology are the understanding and control of matter that is at least one nanometer to a few hundred nanometers in one or more dimensions. At nanoscale, it is a number of atoms and molecules which play the role, but the system is still small enough to behave differently from their bulk counterparts. The quantum size effect and surface/interface effect are the important factors that regulate the properties of materials, leading to unique phenomena and novel applications.

The term of "nanotechnology" was first coined by Professor Norio Taniguchi in 1974 [1], but as early as 1959, physicist Richard Feynman for the first time sketched the framework of nanoscience and nanotechnology in his famous lecture, "There is Plenty of Room at the Bottom", at the annual American Physical Society meeting [2]. He noted that scaling issues would arise from the changing magnitude of various physical phenomena and predicted its various potential applications in such as bio-engineering and information technology. He also described a method by which to

manipulate and characterize matter at the atomic scale. These ideas were realized by Gerd Binnig and Heinrich Rohrer at IBM in 1981 [3]. They invented scanning tunneling microscope (STM), a powerful tool for viewing surfaces at the atomic level using quantum tunneling effect. In 1985, Gerd Binnig, Christoph Gerber and Calvin Quate further developed atomic force microscope (AFM) to overcome STM's basic drawback that only conducting surfaces could be investigated. From the material view point, Buckyball (C60) was discovered by Harold Kroto, Robert Curl and Richard Smalley in the same year of 1985 by using mass spectrometry [4]. Nanoscience and nanotechnology have been advanced in more vast and far-reaching ways by two of the most fundamental building blocks: one-dimensional carbon nanotubes and zero-dimensional colloidal semiconductor quantum dots which were discovered by Sumio Iijima and Louis Brus, respectively [5, 6]. These two works play a key role in the recent tremendous improvements of nanoscience and nanotechnology that are made almost daily by scientists and engineers from across the world.

My graduate research has focused primarily on the precise and tunable control of size, shape, composition and structure of zero-dimensional nanoparticles (NPs), aimed at serving as model systems for exploring fundamental science as well as building blocks of practical device applications. This thesis is outlined as follows: The first chapter begins with an overview of some basic concepts and current progresses of NPs, including semiconductor, metal and magnetic NPs, and their related optical, electronic and magnetic properties and applications. It also covers the general synthetic strategies and basic measurements; The focus of the second chapter

is an efficient synthetic strategy we have developed to control nanocrystallinity of noble metals with 100% yield, which has enabled tailoring and optimization of nanoscale chemical transformation, fundamental electron and phonon couplings and surface plasmon resonance based sensors [7]; The third chapter introduces a facile and general intermediate phase assisted phase exchange and reaction methodology to achieve layer-by-layer precise control of metallic shell growth over versatile core NPs. Core@shell nanostructures prepared by such precise control provide model systems to investigate nanoscale optics, plasmonics and magnetism in a very accurate manner; The fourth chapter describes our discovery of a pressure induced spin metastable state of semiconductor NPs by a novel experimental method combining all optical spin measurements and high pressure diamond anvil cell; Finally this thesis is concluded by a summary and future outlook.

2. Zero-dimensional Nanoparticles

Zero-dimensional nanostructures, also known as nanoparticles are of great scientific interest because they can serve as a bridge between bulk materials and isolated atoms or molecules. A bulk material has constant physical properties, regardless of its size, which can be successfully described by classical theories, while the properties of a single atom or molecule and the interactions among them are quantum mechanical in nature. At the nanoscale, NPs consisting of a finite number of atoms possess significant surface to volume ratio and discrete electronic density of

states, which lead to many unique properties. One example is the tunable optical properties of semiconductor and metal NPs, without which nanoscience and nanotechnology would not be as attractive and exciting as it is today.

In the next I would like to overview some basic concepts, unique properties, practical applications as well as current experimental status of zero-dimensional NPs, based on their functionalities of semiconductor, metal and magnet.

2.1 Semiconductor Nanoparticles

Figure 1.1 shows the colorful image of semiconductor NPs in a series of sample vials. The origin of rainbow colors is the tunable band gap structure of semiconductor NPs.

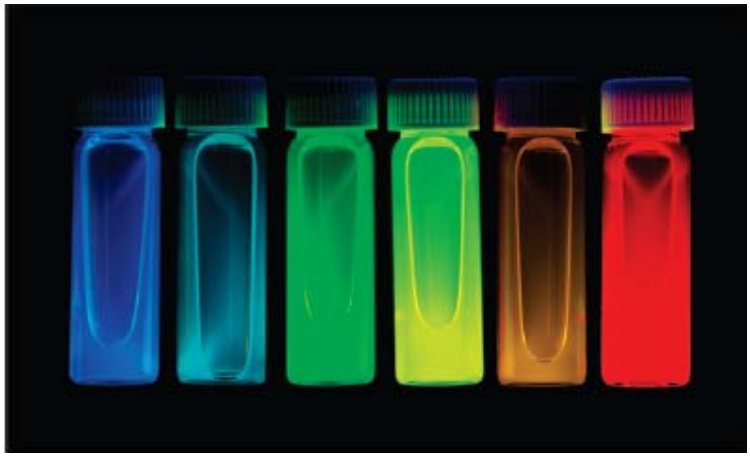

Figure 1.1 Size dependent photoluminescent colors of colloidal CdSe NPs dispersed in hexane. Photography by Felice Frankel, from the website of Bawendi group at the MIT Department of Chemistry [8].

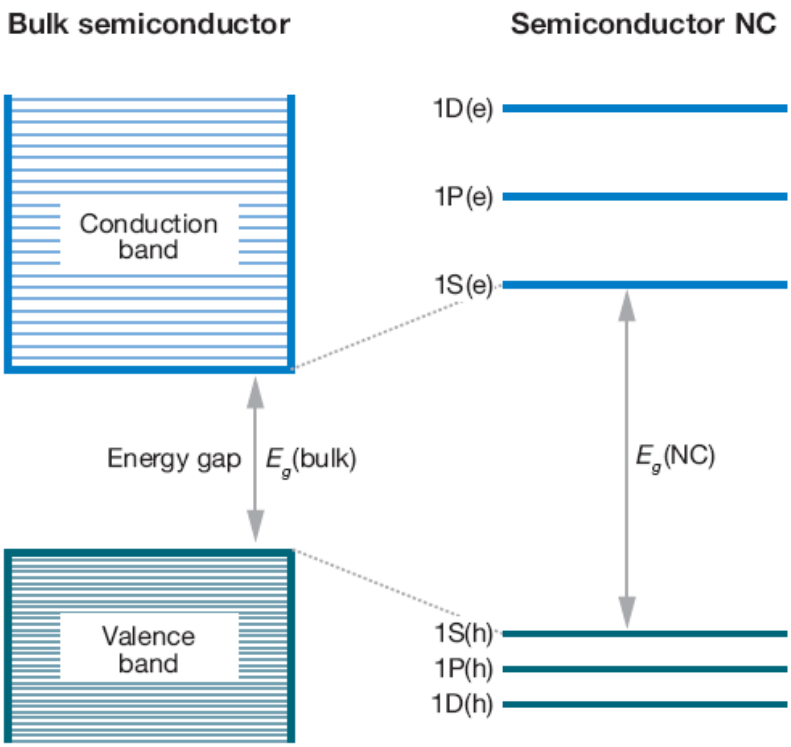

Figure 1.2 The continuous conduction and valence energy bands of a bulk semiconductor are separated by a fixed energy gap, E_g(bulk), whereas a semiconductor nanocrystal (NC) has discrete atomic-like states and a NC size-dependent energy gap. (From Ref. [9])

The energy band gap width of semiconductor materials that separates the conduction band from the valence band is important for both fundamental science and practical device applications (Figure 1.2). In bulk materials, the energy band gap is a fixed parameter and is only determined by the nature of materials. Absorption of a photon by semiconductor materials promotes an electron from the valence band into the conduction band, which creates an "electron-hole" pair. If the size of semiconductor materials is reduced to be comparable to or smaller than the natural length scale of electron-hole pair (Bohr radius), it is confined by the boundaries of the

materials, which leads to an interesting atomic- (or molecular-) like optical behavior. This phenomenon is known as "quantum size effect", which arises solely due to the finite size of NPs. Therefore, semiconductor NPs with the size smaller than Bohr radius are also named as quantum dots (QDs).

The relation between the electron energy band gap and the size of semiconductor NPs was first developed by Louis Brus by using the simple "particle-in-sphere" model assuming an arbitrary particle inside a spherical potential well with a series of approximations [9, 10]. The first approximation is the "effective mass approximation" which completely ignores the semiconductor atoms in the lattice and treats the electron and hole as "free particles". The second approximation is the "envelope function approximation" [11] which considers the NP as a "bulk" compared to the size of electron and hole. The third one is the "strong confinement approximation" which justifies the Coulomb attraction between the negatively charged electron and positively charged hole in the strong confinement regime [12]. Therefore, the electron-hole pair (*e*-*h*) states in a semiconductor NP can be given as

$$\Psi_{e-h}(\vec{r}_e,\vec{r}_h)=\Psi_e(\vec{r}_e)\Psi_h(\vec{r}_h)=u_c f_e(\vec{r}_e)u_v f_h(\vec{r}_h)$$
$$=C\left[u_c\frac{j_{L_e}(k_{n_e,L_e}r_e)Y_{L_e}^{m_e}}{r_e}\right]\left[u_v\frac{j_{L_h}(k_{n_h,L_h}r_h)Y_{L_h}^{m_h}}{r_h}\right]$$

with energies,

$$E_{e-h}(n_h L_h n_e L_e) = E_g + \frac{\hbar^2}{2a^2}\left\{\frac{\varphi^2_{n_h,L_h}}{m^v_{eff}} + \frac{\varphi^2_{n_e,L_e}}{m^c_{eff}}\right\} - E_c$$

Where, e is the electron, h the is hole, v means the valence bonds, c means the conduction bonds. $Y^m_\ell(\theta,\phi)$ is a spherical harmonic, $j_\ell(k_{n,\ell}\, r)$ is the ℓ^{th} order spherical Bessel function. $m^{c,v}_{eff}$ means the "effective mass". u is a function with the periodicity of the crystal lattice. The states are labeled by the quantum numbers $n_h L_h n_e L_e$. The lowest pair state is written as $1S_h 1S_e$. E_g is the semiconductor band gap and the energies are relative to the top of the valence band. E_C is the first order Coulomb attraction energy correction, which is 1.8 $e^2 / \varepsilon a$ for the electron in the $1S_e$ level, where ε is the dielectric constant of the semiconductor material [13]. The selection rules for an optical transition from the ground state to a particular electron-hole pair state can also be obtained by this "particle-in-sphere" model. The rules are Δn=0 and ΔL=0.

The equation describes that the band gap width decreases as the NP size (a^2) increases. It is true that the real band structure of semiconductor NPs is more complicated than the "particle-in-sphere" model [14-16]. The more accurate band gap structure in semiconductor NPs can be explored by combining theoretical calculations with optical spectroscopic techniques. The first technique is transient differential absorption (TDA) spectroscopy [17], which is also called pump-probe or hole-

burning spectroscopy. It measures the absorption change in semiconductor NPs induced by a spectrally narrow pump beam. The advantage of TDA is its high resolution, while the disadvantage is that its strong absorption features overlap with the interesting complicated features of the semiconductor NPs. In addition, a more convenient technique, photoluminescence excitation (PLE) [18] is widely used in today's semiconductor NP research. The origin of photoluminescence of semiconductor NPs is the recombination of photo activated electron-hole pair (exciton) at the band edge and the deactivation of excited electron or hole at the surface states [19].

While the single NP photoluminescence spectra can be obtained by such as low-temperature near-field scanning optical microscopy [20], well controlled and high quality semiconductor NPs samples are the essential for all the characterizations and applications. Over the last three decades, significant efforts have been made by scientists and engineers to achieve various kinds of semiconductor NPs with controlled size, shape, surface, structure and impurity.

The first successful synthesis of CdSe NPs with narrow size distribution was demonstrated by Christopher Murray and coworkers by high temperature colloidal synthesis [9, 21]. The CdSe NPs ranging from 1.5 nm to 12 nm in diameter have absorption in the visible light range (Figure 1.3).

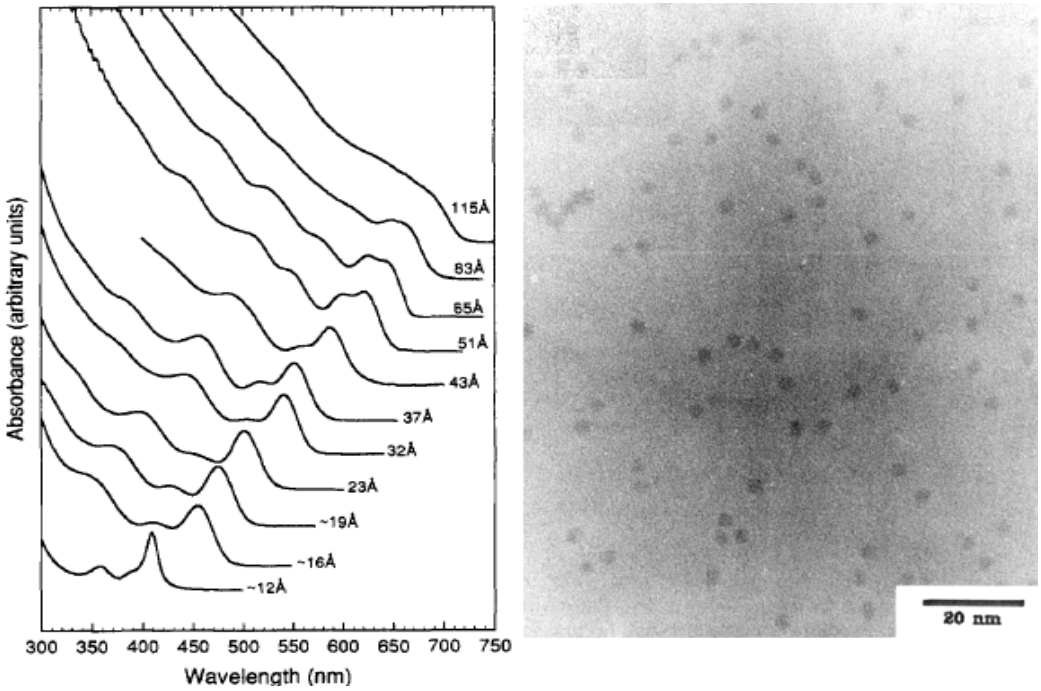

Figure 1.3 (Left) Optical absorption spectra of CdSe NPs ranging from 1.2 to 11.5 nm in diameter dispersed in hexane at room temperature. The experimental observed relationship between energy band gap and semiconductor NPs size fits the simple "particle-in-sphere" model at the large size. For small NPs, more complicated models are needed. (Right) A typical Transmission Electronic Microscope (TEM) image of CdSe NPs averaging 3.5nm ± 5% in the direction of the (002) wrtzite axis and 3.0nm ± 6% perpendicular to the (002) axis. (From Ref. [21])

Later, CdS, CdSe and CdTe NPs are synthesized by the similar process with controllable passivated surface to achieve better photoluminescence with high quantum yields [22]. Other II-VI NPs are also well developed, such as ZnSe for ultraviolet emitting [23] and PbSe for infrared [24] showing in Figure 1.4 and Figure 1.5.

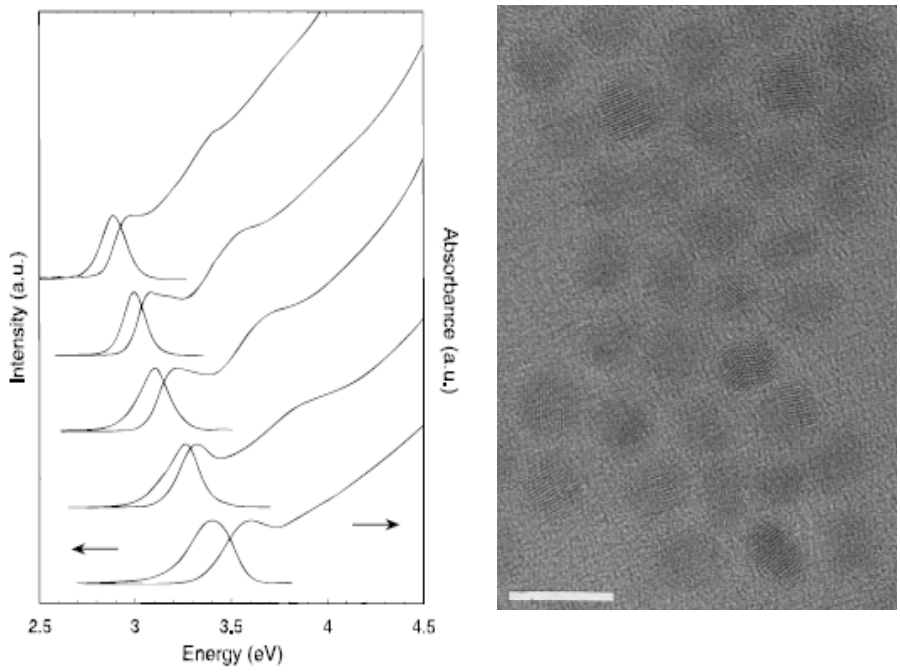

Figure 1.4 (Left) Optical absorption and luminescence spectra of ZnSe NPs ranging from 6.0 nm (uppermost) and 4.3 nm (next down) in diameter dispersed in hexane at room temperature. (Right) A High-resolution TEM (HR-TEM) image of ZnSe NPs with an average diameter size of 6.0 nm. The size bar represents 10 nm. (From Ref. [23])

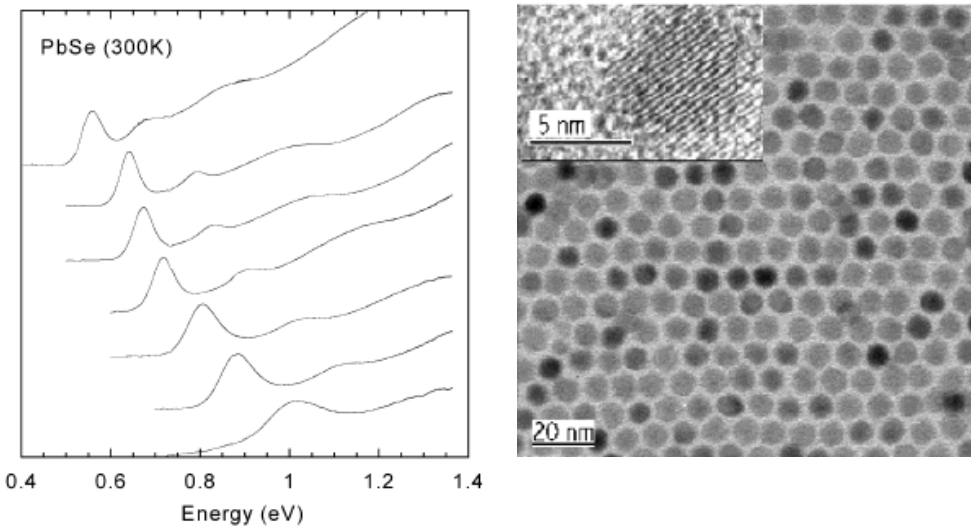

Figure 1.5 Optical absorption spectra (left) and TEM images (right) of PbSe NPs synthesized by high temperature colloidal synthetic strategy. (From Ref. [25])

The similar high temperature colloidal synthetic strategy is not limited to II-VI NPs, but can also be extended to more covalent III-V semiconductor NPs with larger Bohr radius, for examples InP, GaP and $GaInP_2$ with tunable size and narrow distribution [19, 26]. Silicon NPs are also generated by the colloid method [27]. Detailed methods will be discussed in the third section of this chapter. Other approaches to semiconductor NPs, such as molecular beam epitaxy (MBE), chemical vapor deposition (CVD), and room temperature aqueous based reactions, inverse-micelle techniques have been also applied.

Surface/interface effect plays a critical role in nanoscience and nanotechnology because the surface to volume ratio increases remarkably when the size of NPs shrinks. Controlled passivated surface by organic molecules on semiconductor NPs impacts the electric and optical properties [22, 23]. Core@shell structure is another pathway to modify the surface, which can be realized by coating semiconductor NPs with epitaxial layers of different semiconductors (Figure 1.6) [28].

CdSe core with ZnS or CdS shell shows an order of magnitude enhancement in photoluminescence comparing with plain CdSe NPs (Figure 1.7) [29]. A series of combinations of II-VI and III-V semiconductor core@shell NPs have been achieved such as InAs@InP and InAs@CdSe and more complicated multi-shell structures such as CdS@HgS@CdS and ZnS@CdS@ZnS with different band gap structures [30].

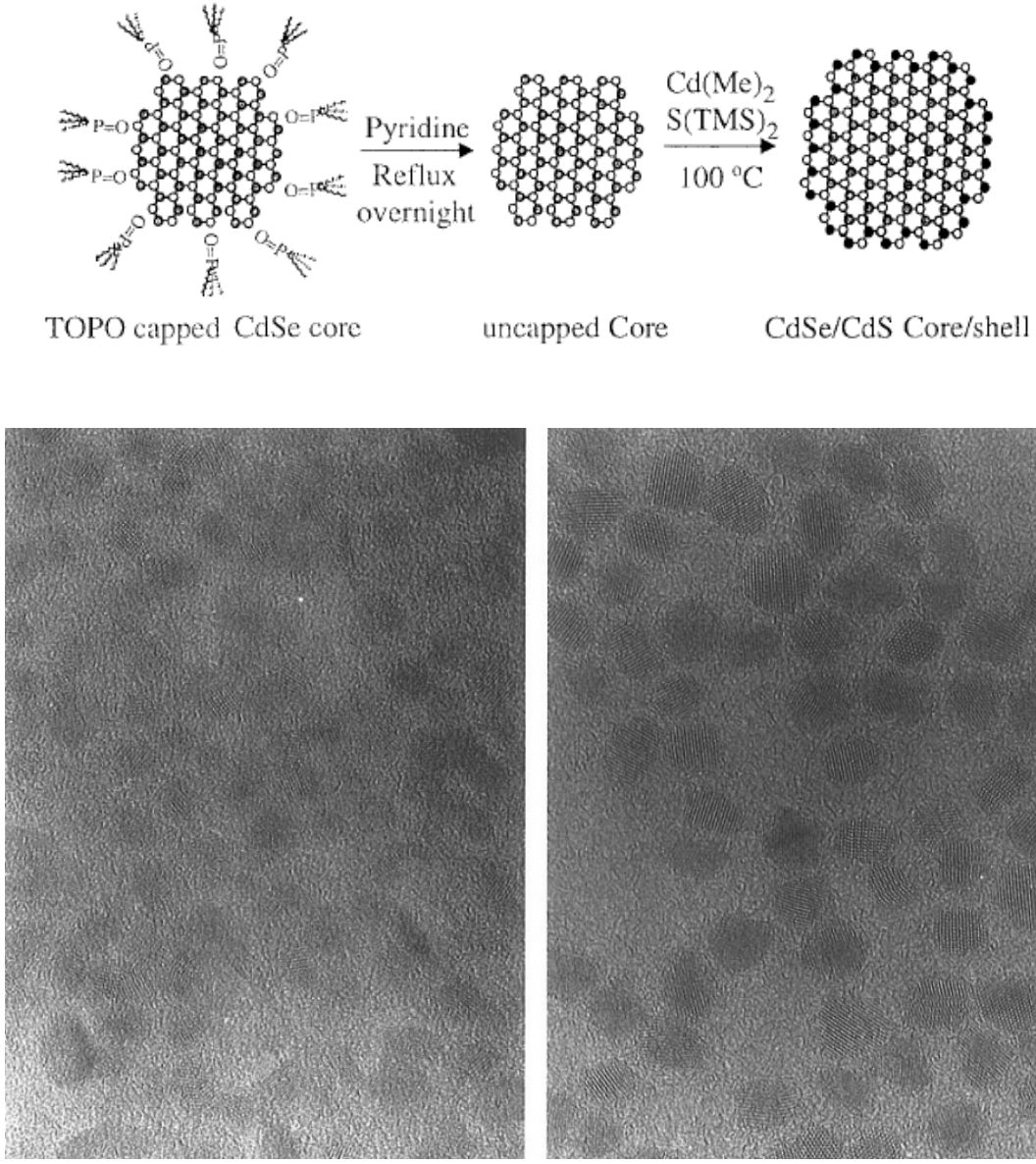

Figure 1.6 (Top) Schematic synthesis of CdSe@CdS core@shell NPs and TEM images of 3.4 nm CdSe plain core NPs (bottom left), and CdSe@CdS NPs with 0.9nm CdS shell overcoating on 3.4nm CdSe NPs (bottom right) (From Ref. [28])

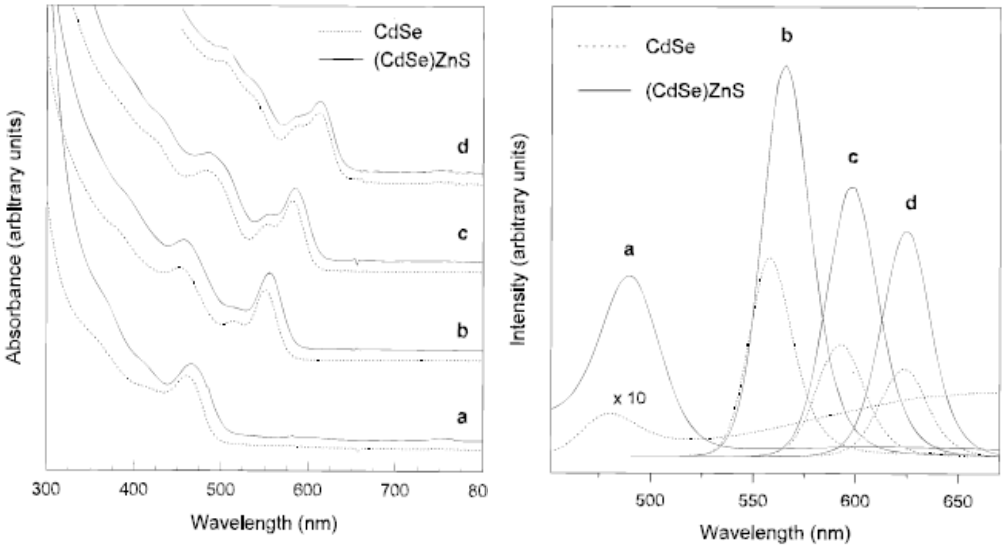

Figure 1.7 Absorption (left) and photoluminescence (right) spectra for plain CdSe NPs and CdSe@ZnS NPs, respectively. The sizes of CdSe core NPs are (a) 2.3, (b) 4.2, (c) 4.8, (d) 5.5 nm. The ZnS shell is one or two monolayer. (From Ref. [29])

Surface energy also can be modified by anisotropic morphology of semiconductor NPs, which have much higher energy than spherical NPs. Synthesis of rods, arrows, stars, teardrops, even tetrapods of II-VI semiconductor NPs have been successfully developed by many groups [31, 32]. Impurities doping into NPs is also an effective way to change the band gap structures in semiconductors. There has been a great deal of activity on this subject: Mn^{2+} and Co^{2+} have been shown to modify photoluminescence of CdSe, ZnSe and CdS with higher quantum yields [33].

The application of hydrostatic pressure represents a crucial means to modify material parameters such as the lattice spacing and the crystal structure that could not

be easily achieved by other methods [34]. Alivisatos group at Berkeley found a first-order solid-solid phase transition from wurtzite to rock-salt structure, first identified by X-ray diffraction measurements [35]. Our group observed a long-lived metastable intermediate phase before the first-order solid-solid phase transition by combining spin dynamics with high pressure technique, which will be discussed in detail in the Chapter 4.

Semiconductor NPs have also created a lot of interest for various device applications, including biological and energetic applications. Size-tunable color, broad absorption and narrow emission, as well as easy functionalization by biological molecules on the surface make semiconductor NPs a competitive candidate for cell labeling and tracking, DNA detection and in vivo imaging [36]. Compared with organic dye molecules, semiconductor NPs have bright photoluminescence and high endurance. For low cost, large area and manufacturable solar cells, hetero-junctions are the key which make charge separation possible. Band gap engineered semiconductor NPs are promising for making charge separation more efficient because of their large surface/interface in related hetero-junctions. Beyond this, such structures can create opportunities to explore new generation of solar cells with multiple excitons and energy up-conversions [37, 38].

2.2 Metal Nanoparticles

The beautiful colors of small metal particles have been noticed since the fourth century A.D. The famous Lycurgus cup changes color when held close to light: The opaque green cup turns to a glowing translucent red when light is shone through it. At that time, it was not known that small amount of gold and silver NPs embedded in the glass could give the cup unusual optical properties, until Michael Faraday recognized the physical processes of colors in the nineteen century [39]. When a small spherical metal particle is photoactivated, the conduction electrons inside are driven to a coherent oscillation by the oscillating electric field of the light and the Coulomb attraction with nuclei in the particle. This phenomenon is called localized surface plasmon resonance (LSPR), which is the origin of color of small metal particles. (Figure 1.8)

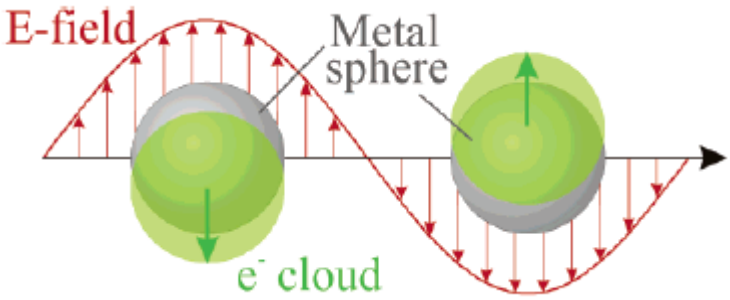

Figure 1.8 Schematic of localized plasmon oscillation of free electrons in a small spherical metal particle. (From Ref. [40])

In the early twenty century, Gustav Mie first precisely calculated the interactions between the incident light and the small spherical metal particle by solving Maxwell's equations [41]. Briefly, a quasi-static approximation is used when the radius of spherical NPs (a) is much smaller than the wavelength of the irradiated z -polarized light (λ), i.e. a <0.1 λ . The electromagnetic field outside of the NP is determined by,

$$\overrightarrow{\boldsymbol{E}}_{out} = E_0 \hat{\mathbf{z}} - \left[\frac{\varepsilon_{in} - \varepsilon_{out}}{\varepsilon_{in} + 2\varepsilon_{out}} \right] a^3 E_0 \left[\frac{\hat{\mathbf{z}}}{r^3} - \frac{3z}{r^5} \left(x\hat{\mathbf{x}} + y\boldsymbol{y} + z\hat{\mathbf{z}} \right) \right]$$

Where, ε_{in} is the dielectric constant of the metal NP, and ε_{out} is the external environment dielectric constant. ε_{in} is strongly dependent on λ , the approximate resonance condition is $\varepsilon_{in} = -2\varepsilon_{out}$, which means the electromagnetic field is enhanced relative to the incident light. The extinction spectrum is given by,

$$E_{ext}(\lambda) = \frac{24\pi^2 N a^3 \sqrt{\varepsilon_{out}^3}}{\lambda \ln(10)} \left[\frac{\varepsilon_i(\lambda)}{\left(\varepsilon_r(\lambda) + 2\varepsilon_{out} \right)^2 + \varepsilon_i(\lambda)^2} \right]$$

Where, $\varepsilon_{in}(\lambda) = \varepsilon_r(\lambda) + i\varepsilon_i(\lambda)$ [42]. The scattering term or radiative damping effect has been omitted and only dipolar terms are considered for the whole calculation, more accurate expression can be developed by such as the discrete dipole approximation and the finite-difference time-domain methods. This expression is

valid only for small spherical NPs. It should be modified when calculated for NPs with high aspect ratio geometries, and higher multipoles especially the quadrupole terms should be considered for larger NPs [40].

The maximum of LSPR extinction wavelength, $\lambda_{\max}$ is sensitive to the dielectric constant (or refractive index, $n = \sqrt{\varepsilon}$). The relationship between the shifts in $\lambda_{\max}$ and the changes of the local environment is given as follows [43],

$$\Delta\lambda_{\max} = m_{bulk}[1 - e^{(-2d/l_d)}](\Delta n)$$

Where m_{bulk} is the refractive index of NPs bulk counterpart material, d is the effective adsorbate layer thickness and l_d is the approximated decay length of electromagnetic field.

The enhanced electromagnetic field is useful for spectroscopic characterizations of physical and chemical structures and processes. There are four main kinds of spectroscopies, surface enhanced absorption, surface enhanced fluorescence, surface enhanced Rayleigh scattering and surface enhanced Raman scattering (SERS). The SERS spectroscopy is holding a great deal of research interest because the signals from molecules functionalized on metal NPs can be enhanced by a factor up to 10^{14}~10^{15} [44]. The mechanism of this pronounced SERS effect is a long-debated subject. Briefly, two different mechanism categories have been proposed: the first is

electromagnetic enhancement and the second is chemical enhancement [45]. The enhancement of Raman scattering only happens when molecules are adsorbed on rough metal surfaces, which means the smooth surface is not active for the enhancement.

To understand LSPR and the surface enhanced spectroscopy deeply, ultrafast (femtosecond) laser technique has been used to explore electron dynamics in metal NPs, such as the energy decay processes of the electromagnetic enhancement [46]. In a typical process: the energy of incident light is absorbed by electrons, and then is redistributed among electrons by electron-electron (*e*-*e*) scattering, eventually leading to an established electron temperature in less than one picosecond; The energy is continually transferred to the lattice (phonon) by electron-phonon (*e*-*ph*) interaction leading to thermalization of the lattice and the electron gas which takes place in several picoseconds; Finally the energy is dispersed into the surrounding media (matrix) by phonon-phonon (*ph*-*ph*) and phonon-matrix interactions. The whole process is described as the "Two-Temperature Model" (Figure 1.9), by which various properties of the conduction band electrons especially the quality of the plasmon resonance can be defined. The detailed technique and calculation will be discussed in the Chapter 2.

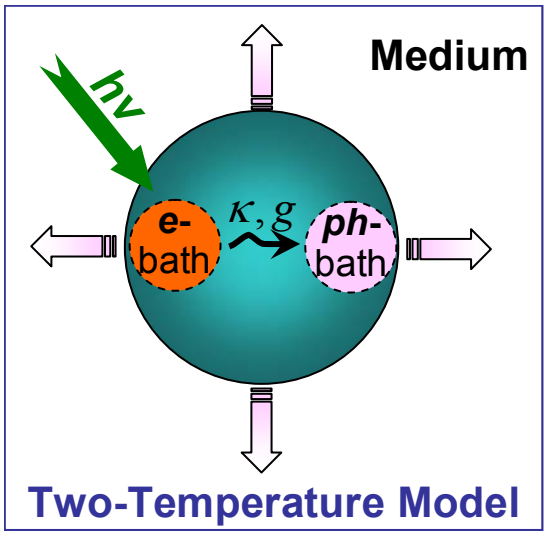

Figure 1.9 Schematic illustration of "Two-Temperature Model" in a metal NP.

As the discussion above, the electron oscillation frequency is the heart of electronic and optical properties of metal NPs, and it is determined by the density of electrons at the Fermi Level, the effective electron mass, and the shape, size of the electron distribution [40]. The highly controlled NP samples are playing the key role for fully understanding and application of electromagnetic enhancement. Various novel methods such as wet chemical synthetic techniques, electronic- and ion- beam lithography have been developed to fabricate large quantities of metal NPs with controlled size, shape and component (Figure 1.10). Many interesting electromagnetic enhancements have been investigated (Figure 1.11) [47-49]. Beyond these, crystallinity control of metal NPs is a relatively new topic. In the Chapter 2, the remarkable contribution to this subject achieved by my graduate research will be described in detail [7].

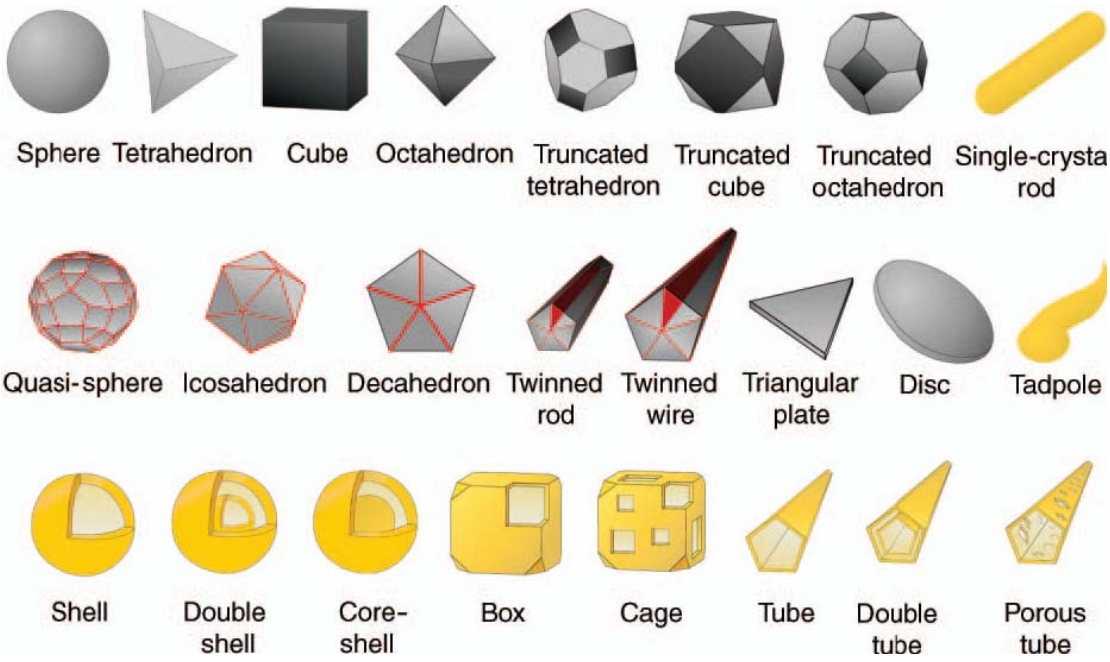

Figure 1.10 Schematic diagrams illustrating the artificial shapes of metal nanostructures. (From Ref. [50])

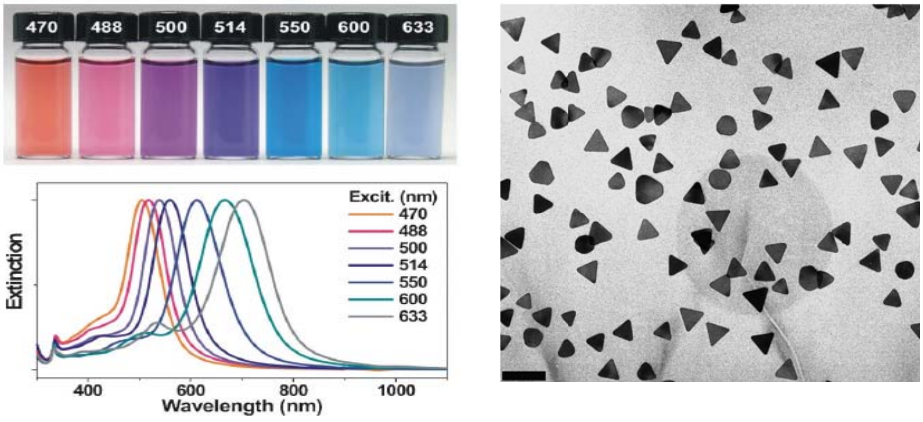

Figure 1.11A (Left) Extinction spectra and corresponding solutions photographs of Ag nanoprisms with varying edge length. (Right) A typical TEM image of Ag nanoprisms (scale bar is 100nm). (From Ref. [47])

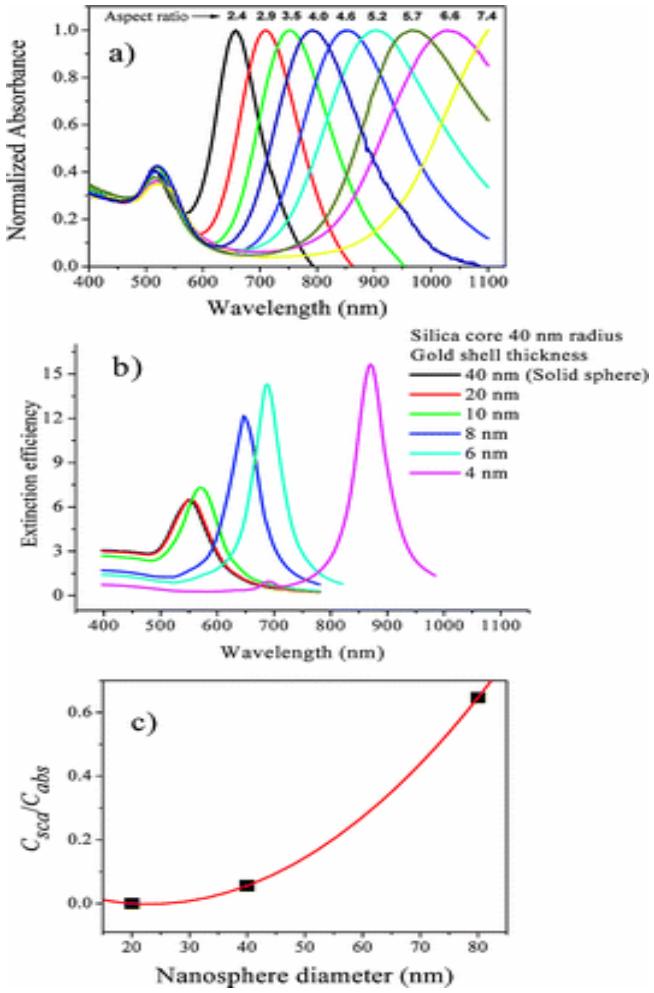

Figure 1.11B Size, shape, and composition tunability of the LSPR of noble metal nanostructures. (a) Tuning the LSPR frequency of the gold nanorod long-axis mode by synthetically controlling aspect ratio. (b) Si@Au core@shell NPs show LSPR frequency tunable from the visible to the near-IR by changing the shell thickness relative to the core size. (c) Increase in the plasmon scattering to absorption ratio by increasing the size of gold NPs. (From Ref. [48])

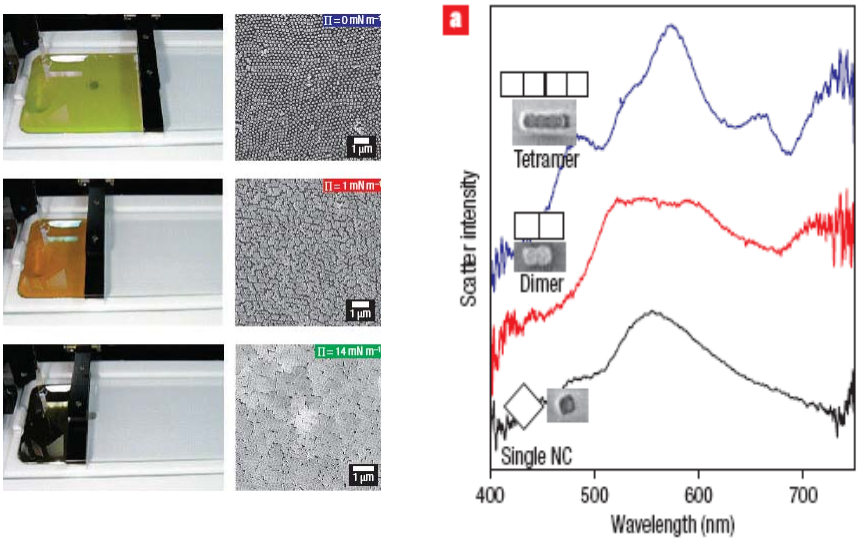

Figure 1.11C (Left) Tunable plasmon response of Ag cuboctahedra NP assembles achieved by the Langmuir–Blodgett technique. (Right) Dark-field scattering spectra of different Ag NPs pairs or chains. (From Ref. [49])

The LSPR of metal NPs is typically in the range of ultraviolet or visible wavelength without blinking or bleaching features, which offers opportunities to apply gold and silver NPs as biological probes. One of the examples is the "molecular ruler" by Paul Alivisatos and coworkers to measure the length of DNA [51]. And non-isotopic and non-toxic gold and silver NPs with bio-conjugations are promising for SERS imaging of the structures and functions of cells and tissues [36]. Enabled by the near-field couplings between LSPR with individual NPs, silver and gold NP chains/arrays have been demonstrated both theoretically and experimentally to guide the flow of electromagnetic energy over hundreds of nanometers without significant loss [52]. This creates lots of opportunities for nanoscale photonic devices.

2.3 Magnetic Nanoparticles

Our pursuit of better magnetic materials has continued for thousands years, because they are everywhere in our life from huge planets to small credit cards. Both the length of atomic exchange interaction and the width of domain wall in ferromagnetism are in the nanoscale region. Obviously, magnetic NPs are promising not only for the miniaturization of practical devices but also for the exploration of new properties and fundamental mechanisms. Like the semiconductor and metal NPs discussed above, size and surface effects play the key role when the size of magnetic NPs is comparable to the size of magnetic domains.

It is well known that the size of magnetic domains, the width of domain walls and their inner structure are continuously changing due to the reduced volume of the bulk magnetic system with multidomain structure. Eventually, the NP can possess only one single domain structure, when its size is below a certain critical size (D_c), in which the energy for supporting the external magnetostatic stray field of the single domain is smaller than the energy for creating a domain wall. The critical size is determined by the saturation magnetization of particle, anisotropic energy and exchange interactions between individual spins. The critical size is a few tens of nanometers for most magnetic materials and a few hundreds of nanometers for some high anisotropy materials. In the single domain regime, the relationship between the magnetic coercivity (H_c) with the NP volume (V) is given by [53],

$$H_c = 2\frac{K_u}{m_s}\left[1 - 5\sqrt{\frac{k_B T}{K_u V}}\right]$$

Where, K_u is the magnetic anisotropic constant, m_s is the saturation magnetization, and k_B is the Boltzmann's constant and T is the temperature. The magnetic coercivity of a single domain is larger than that of multidomain, and it decreases as the size of the NP decreases (Figure 1.12).

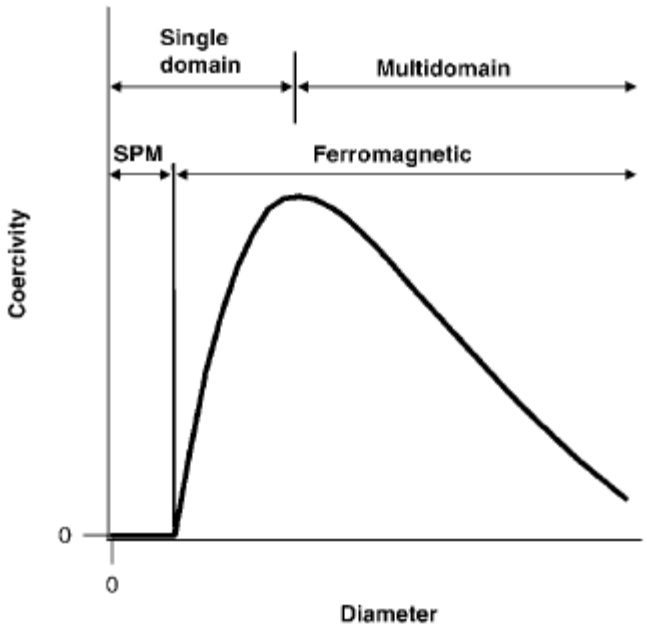

Figure 1.12 Schematic diagram illustrating size-dependent magnetic domain structures from superparamagnetism (SPM) to single domain and multidomain ferromagnetism. (From Ref. [54])

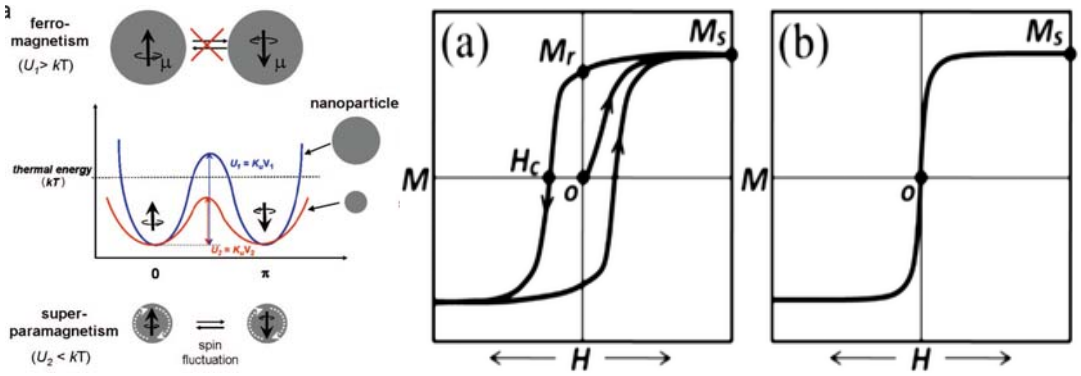

Figure 1.13 (Left) Schematic diagrams illustrating energy of magnetic NPs with different magnetic spin alignment. (From Ref. [54]). (Middle and right) Diagrams illustrating a typical hysteresis loop of a single domain ferromagnetic NP and a typical curve for a superparamagnetic NP, respectively. (From Ref. [55])

Furthermore, the energy barrier (K_uV) decreases as the size of NPs decreases, which means the smaller amount of energy is required to reverse the magnetization for smaller NPs. When the thermal energy (k_BT) exceeds the energy barrier, the easy magnetic fluctuation makes the NPs behave like a conventional paramagnet without hysteresis in the magnetization curve. This phenomenon is called "superparamagnetism" (Figure 1.12 and 1.13). The temperature corresponding to the transition from ferromagnetism to superparamagnetism is referred to as the blocking temperature (T_b). The blocking temperature depends on the size of NPs, the effective anisotropy constant, the applied magnetic field, and the experimental measuring timescale. The blocking temperature is the essential parameter defining the magnetic behavior of NP devices.

Over the last thirty years, a large family of magnetic NPs with precise and tunable size and components has been achieved by various research groups worldwide, such as Co, Ni, Fe, FePt, CoPt, $CoPt_3$, FeCoPt, γ-Fe_2O_3, Fe_3O_4, $CoFe_3O_4$, $MnFe_2O_4$, MnO, Fe_2P and etc. [56]. Figure 1.14 highlights a few examples of magnetic NPs achieved by colloidal synthesis.

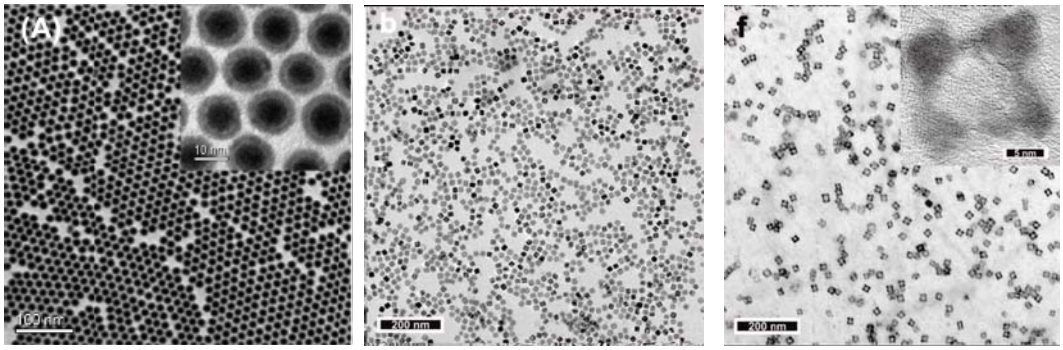

Figure 1.14A (From left to right) TEM images of spherical Fe@Fe_3O_4 Core@Shell NPs, cubic Fe NPs and Fe Nanoframes (From Ref. [57] and [58]).

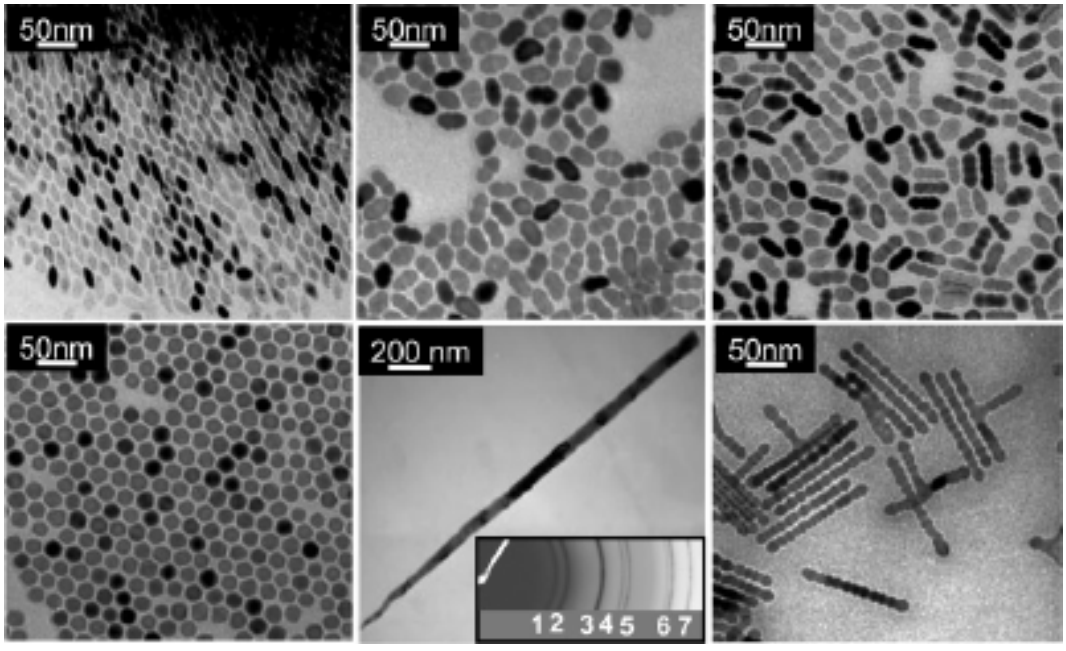

Figure 1.14B TEM images of MnO NPs with different shapes (From Ref. [59]).

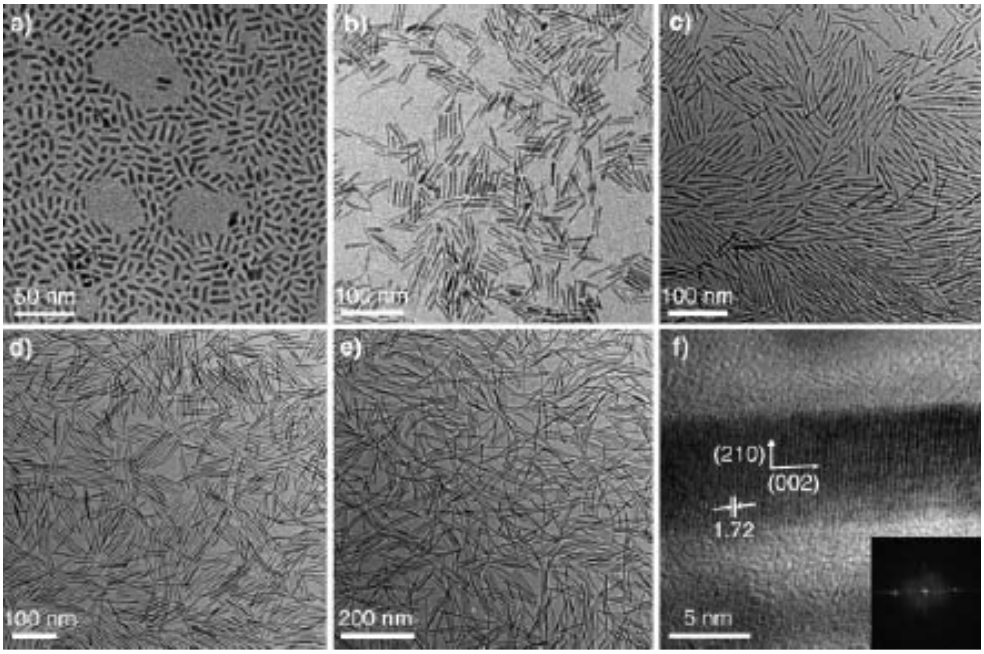

Figure 1.14C TEM images of rod shaped Fe_2P NPs with different dimensions. (From Ref. [60])

On the other hand, the existence of large surface to volume ratio of magnetic NPs plays an important role in determining the magnetism of NPs. The effect could be more significant than the crystalline and shape anisotropy effects. However, the exact mechanism of such surface effects remains an open question due to the contradictory experimental results: an enhancement of the magnetic moment with decreasing size of small metal magnetic NPs was reported [61], while oxide NPs have reduced magnetic moment compared with their bulk counterparts [62]. Many explanations have been proposed, including the existence of uncompensated surface spins, the existence of a disordered spin glass like layer near the surface, the existence of a magnetically dead layer on the surface, and the influence of organic ligand capping with surface metal atoms and etc. [63]. Magnetic NPs with precise and

tunable non-magnetic shell layer might server as good model systems to systemically explore the mechanism, which will be discussed in the Chapter 3. As mentioned in the beginning of this chapter, magnetic NPs have demonstrated for various applications, and all of them are very close to human daily life. Here several examples are given, such as ultra high density magnetic recording media for information storage; ultra strong permanent magnets for energy efficiency, conservation, and self-sufficiency; and ultra sensitive magnetic sensor for biomedical diagnosis and therapy [64].

3. Principle of Colloidal Synthetic Strategies of Nanoparticles

For nanoscience and nanotechnology, the importance of sample quality can never be overemphasized. Almost all the unique properties and novel applications of nanoscale materials dramatically depend on their size, shape, component and structure. Generally, there are two main categories for nanoscale materials fabrication: “top-down” and “bottom-up”.

The easiest picture for the “top-down” approach is the sculpture, the raw materials is cut into desired structure. The knives in nanoscience and nanotechnology are focused ion beams, atomic force microscope tips (Dip-pen) as well as some other techniques descended from conventional solid-state silicon methods. However, it is not easy to achieve the nanostructures with very small size by the “top-down”

strategy due to technological challenges. On the contrary, the "bottom-up" approach uses atoms or molecules as bricks to build nanostructure, therefore there is no theoretical size limitation.

Wet chemical colloidal synthesis is a typical "bottom-up" approach for NPs. Compared with the other main approach, clean room technique, wet chemical colloidal synthesis is cheap and facile, the as-synthesized nanostructures are free standing and easy functionalized.

Figure 1.15 shows a typical apparatus employed in colloidal synthesis of NPs. The designs can enable flexible control of all necessary parameters for versatile materials by different synthetic routes. More importantly, the kinetics of NPs growth can be monitored through the whole process by simply taking out partial reactant from the solution.

The mechanism of colloidal NPs growth can be described by the model developed by La Mer and Dinegar, and the general processes are shown in Figure 1.16.

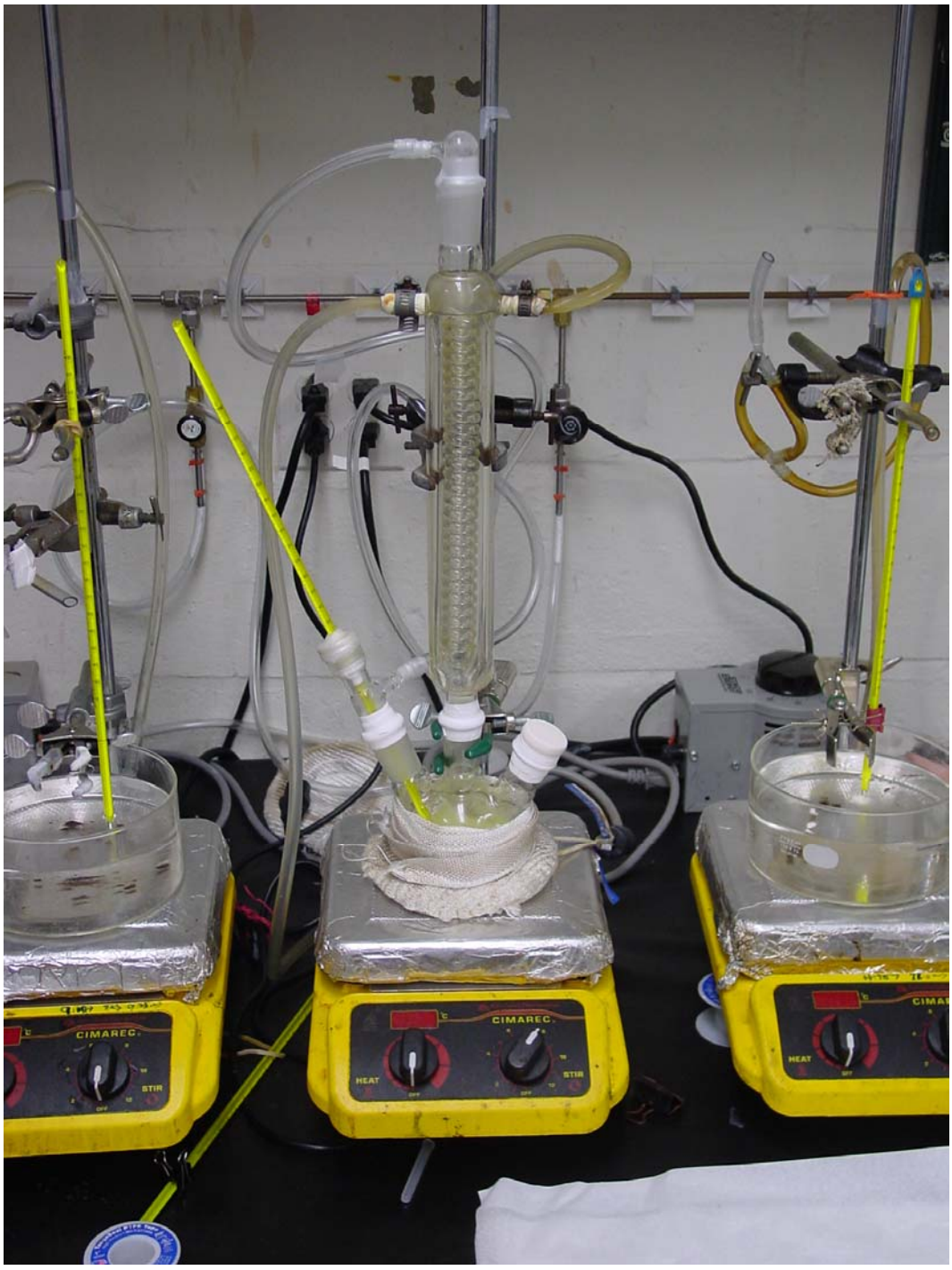

Figure 1.15 A typical set-up for colloidal synthetic strategies of NPs.

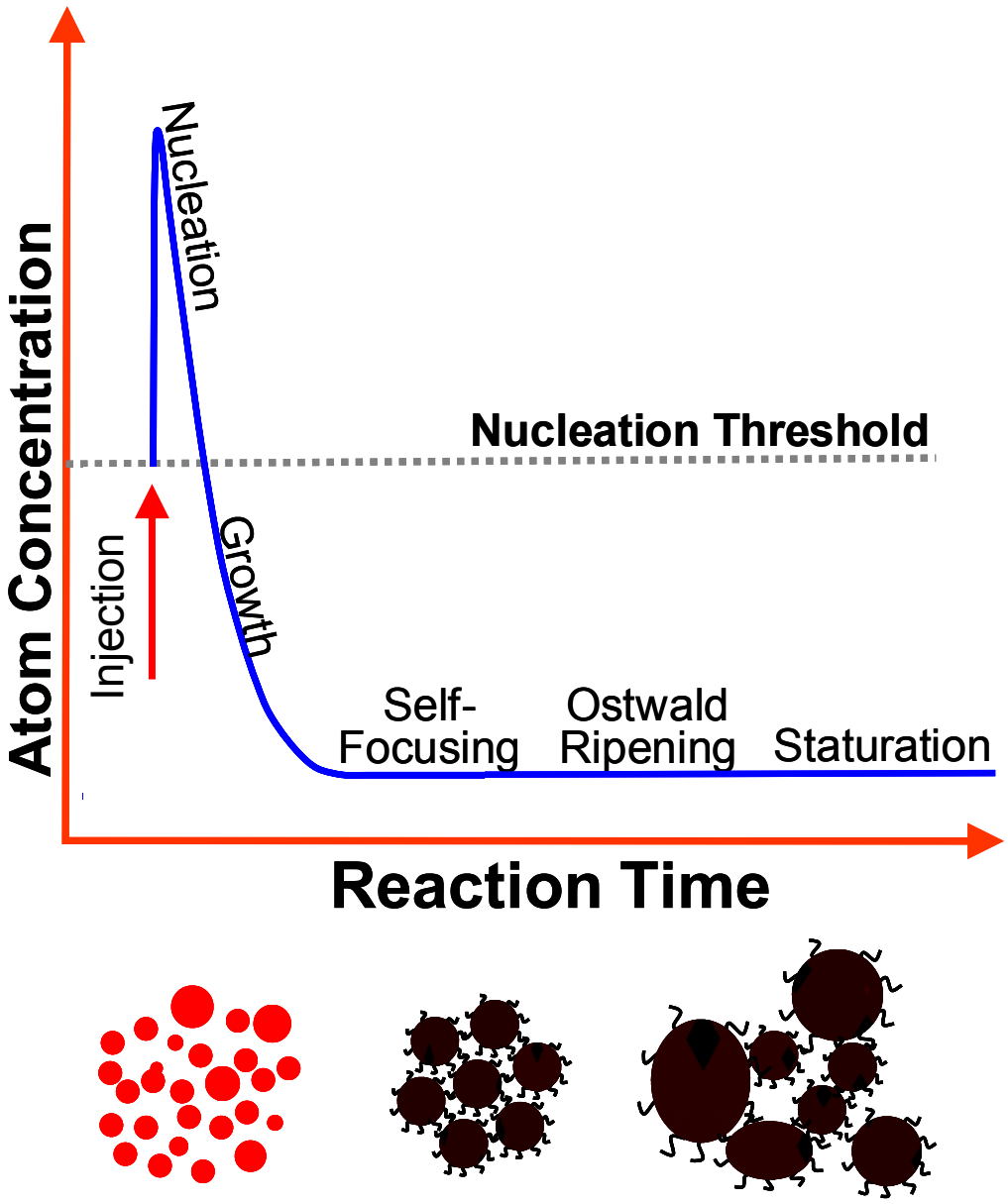

Figure 1.16 Schematic illustrating La Mer model for the general growth processes for colloidal synthesis of NPs

In a typical synthesis: After the precursors, organic surfactants and solvents are mixed, the precursors chemically transform into “monomers”, which are composed by active atoms or molecules; When the concentration of monomers is higher than the critical concentration (nucleation threshold), monomers could aggregate to form “nuclei”; After the formation of nuclei, the concentration of monomers deceases to a value below the critical concentration, and then monomers can only add to the existing nuclei for continuous growth onto NPs; Then monomers exchange among NPs to reduce the whole system energy, which is referred to the “self-focusing” process and lead to the narrowest size distribution; When the organic surfactants is not sufficient for passivating NPs from aggregation, the “Ostwald ripening” happens, and eventually the huge NPs precipitate out from the solution.

The key point for achieving mono-dispersed NPs is the balance of the chemical reaction speed and the growth speed. The concentration of precursor and the capping ability of organic surfactants determine the NP size. The shape controlled NPs can be achieved by selective adhesion of organic surfactants on particles.

Once synthesized, the NPs can be “washed” by polar solvents and be precipitated out by centrifuge. Sometime, further treatments such as thermo annealing and ligand exchange are used for specified applications of NPs. The more detailed procedure of colloidal NP synthesis is described in latter chapters when needed.

4. General Characterization of Nanoparticles

The size, structure and composition of as-synthesized NPs need confirmations and characterizations. In this section, three main widely used techniques for basic characterizations of NPs are introduced.

4.1 Transmission Electron Microscope

Transmission Electronic Microscope (TEM) is a powerful tool for morphology characterizations of NPs, which uses highly energetic electron beam instead of light to "image" the specimen. Resolution of TEM is much higher than optical microscopes because the wavelength of an electron is much smaller than that of a photon of visible light. The point-to-point resolution of a commercial Field Emission TEM is as low as 0.19 nm. Beyond size and distribution measurements, the crystal structure and element information also can be obtained by analytical techniques associated with TEM, including the “Diffraction Mode” of TEM, combined energy dispersive x-ray spectrometer (EDS) and electron energy loss spectrometer (EELS).

Samples for TEM characterization are prepared by adding one drop of NP dispersion in volatile solvent onto copper grids with carbon support film. The samples are ready for use after the solvent is dry.

4.2 Ultraviolet-visible Spectroscopy

The function of this instrument is relatively straightforward. A beam of light from a visible and/or ultraviolet (UV) light source is separated into monochromatic beams by a prism or diffraction grating. Each monochromatic beam in turn is split into two equal intensity beams by beam splitter. One beam, i.e. the sample beam, passes through a small transparent container (cuvette) containing a solution of NPs in a transparent solvent. The other beam, also called the reference beam, passes through an identical cuvette containing only the solvent. Both the intensities of these light beams are then measured by light detectors and compared. In our measurement, the UV scan region is normally from 200 to 400 nm, and the visible portion is from 400 to 800 nm.

4.3 SQUID Magnetometer

SQUID or Superconducting Quantum Interference Devices are very sensitive magnetometers used to measure extremely small magnetic fields, based on superconducting loops containing Josephson junctions. A commercial SQUID usually has the following features: AC Susceptibility Measurement from - 0.1 Hz to 1K Hz with the sensitivity as 2 x l0-8 emu at 0 T; Ultra-Low Field Capability from ± 0.05 G for the 5 T or 7 T magnets; Reciprocating Sample Option (RSO)-DC Magnetization absolute with the sensitivity as 1 x 10^{-8} emu at 2,500 Oe and Continuous Low

Temperature Control/Temperature Sweep Mode (CLTC) with the Sweep rate as 0.001 ~ 10 K/min.

The NP sample for magnetic characterization is in powder form and kept in a lock-ring capsule.

5. Summary

In this chapter, the basic and general concepts of semiconductor, metal and magnetic NP synthesis, characterizations and their related optical, electronic and magnetic properties are reviewed. Based on these introductions, in the next few chapters I will focus on a few specific topics related to zero-dimensional NPs that were carried out in my graduate research.

Chapter 2: Crystallinity Controlled Metal Nanoparticles: Synthesis and Properties [1]

In this chapter I will focus on one important topic of metal nanoparticles (NPs), i.e., how to achieve crystallinity control at the nanoscale. I will start by reviewing the current status of this field. Then I will highlight recent experimental progress towards realization of absolute nanocrystallinity control by using silver NPs as an example. Lastly, I will present three examples to emphasize the importance of nanocrystallinity control, and provide an outlook for future research.

1. Introduction

Metal NPs with size close to or smaller than their electron mean free path (typically 10-100 nm) show many unusual properties and functionalities [9] and can serve as model systems to explore fundamental quantum and classical coupling interactions as well as provide building blocks of many practical applications including catalysis, molecular- and bio-sensing/regulation, photonics [44, 51, 52, 65-69]. The intrinsic properties and functionalities of these NPs depend strongly on their size, composition, shape, structural and electronic defects. Under this context, controlled synthesis of well-defined metal NPs has been a top research interest.

1. This chapter was adapted from: Yun Tang and Min Ouyang. "Tailoring Properties and Functionalities of Metal Nanoparticles through Crystallinity Engineering", *Nature Materials* (2007), 6(10), 754-759.

While recent advances in strategies for chemically synthesizing metal NPs have enabled excellent control of size, composition and even shape [70-79], defect control at the nanometer scale, to ensure essential perfect nanocrystallinity for physics modeling as well as device optimization, has posed outstanding challenges. Because of their small size, NPs typically show unusual crystalline properties as compared with their bulk counterpart [80]. There are a few issues needed to be considered for nanoscale crystallinity, including (1) the constraint of translational invariance on a lattice that does not apply for very small sized nanostructures (<10 nm) and (2) surface energy due to very high surface/volume ratios. In order to analyze NP energetics, the thermodynamics and growth kinetics have to be taken into account. The first question to be considered is what is the most favored structure a NP can possess at low temperature, given its size and composition? For this determination, the potential energy surface global minimum needs to be calculated under different conditions. Theoretically, the binding energy E_b of a NP of size N (with a given structure) can be expressed by considering both volume and surface (from facets, edges and vertices) contributions [80]:

$$E_b(N) = aN(volume) + bN^{2/3}(facets) + cN^{1/3}(edges) + d(vertices)$$

where a, b, c and d are factors related to the sturcture. The stability of NPs in different size ranges can be evaluated by another useful parameter, $\Delta(N)$, defined as follow:

$$\Delta(N) = \frac{E_b(N) - N\varepsilon_{coh}}{N^{2/3}}$$

where ε_{coh} is the cohesive energy per atom in the bulk. $\Delta(N)$ represents the excess energy with respect to N atoms in a perfect crystal. Figure 2.1A shows comparison of $\Delta(N)$ among single crystal face-centered cubic, icosahedron and decahedron NPs, showing that within a small size range, noncrystalline structure may be energetically more stable than a single crystal. This agrees qualitatively with experimental results (Figure 2.1B) [80-83].

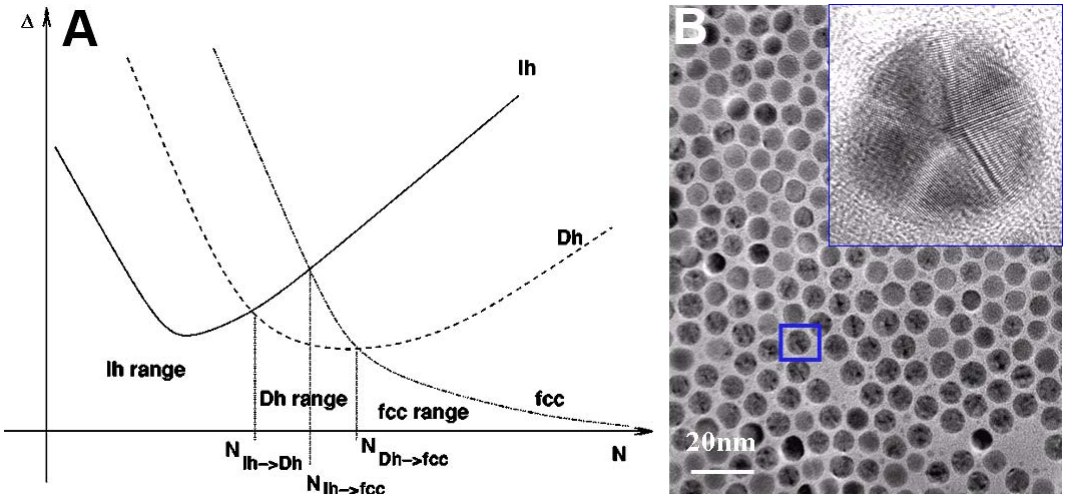

Figure 2.1 (A) Qualitative behavior of Δ(N) for NPs with different crystalline property. This curves show the qualitative relationship between size and stability of small nuclei within a small size range. Icosahedron (Ih) should be the more favored at small size than the other two structures, face-centered cubic (fcc) and decahedron (Dh). Also the potential energy barriers between these morphologies are low enough that thermal fluctuations could provide sufficient energy to provoke shifts between the twinned and single crystal morphologies. So the small nuclei are mixture of Multiple-twinned (*MT*) and Single-crystalline (*SC*) structures, and they continue growing to *MT*- and *SC*-NPs. (B) Silver NPs synthesized from traditional Polyol method showing existence of various structural defects, including five-fold twinning defects (inset).

Crystallinity control of NPs requires efficient ways to adjust the thermodynamic energy during synthesis. Recently, Xia's group at the University of Washington at Seattle demonstrated that by introducing a small amount of chloride and oxygen species into the conventional polyol synthesis, twinned seeds could be selectively etched and dissolved thus promoting the formation of single crystal metal nanostructures [84]. However, this method typically led to large sized nanostructures with a broad size distribution. Our goal is to seek a facile synthetic route that can achieve efficient nanocrystallinity in a highly controlled manner while maintaining less than 5% size variation.

2. A Novel Chemical Synthetic Scheme

We have developed a single-phase synthetic route to achieve mono- dispersed metal NPs with well-defined crystallinity. Figure 2.2 shows examples of both perfect single crystalline (*SC*-) and disorder multiply twinned (*MT*-) structures. We start with a series of organometallic single molecules (such as silver-phosphine complexes, $Ag(PPh_3)_3$–R with *R*= –Cl and $–NO_3$, in the Figure 2.2) as the precursors for synthesizing metal NPs. During the synthesis these molecular precursors not only provide metal chemical sources for growing NPs but also simultaneously release functional groups to guide the synthesis: because of different atomic energy sites on the crystallographic facets, the chemical activity of *MT*-NPs shows a substantial difference with respect to the *SC*- counterpart, or a slight difference among various

twinning configurations. The method provides a general synthetic route for the modification of the thermal barrier (Figure 2.1A) and the nucleation and growth of metal NPs with desired crystallinity. There are two main reasons for choosing the phosphine complex as a precursor in our synthesis: it is a well defined general organometallic complex that can accommodate many different metals and different functional *R* groups can be incorporated and/or combined into the molecules leading to kinetic control of NP synthesis [85-88].

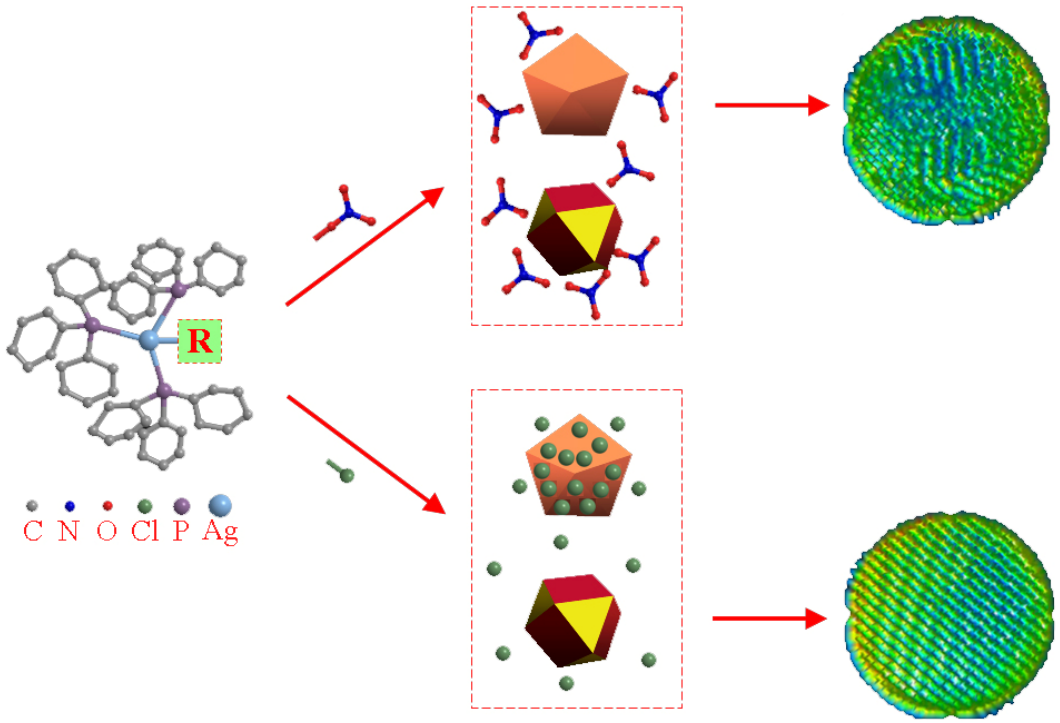

Figure 2.2 A novel synthetic strategy for controlling the crystallinity of silver NPs.

In Section 2.1, silver NPs will be used as an example to describe synthesis and characterization procedures.

2.1 Synthesis and Characterizations of $(PPh_3)_3Ag–R$

Precursor ***1*** (*R*= $–NO_3$): Solution of 17.0 mg silver nitrate (209139, Sigma-Aldrich) in 2 mL anhydrous acetonitrile (271004, Sigma-Aldrich) is added to the solution of 78.7 mg triphenylphosphine (T84409, Sigma-Aldrich) in 8 mL acetonitrile. Crystals slowly precipitate out with gentle agitation. The white crystals are stored in a dark, dry atmosphere after washing several times with acetonitrile and drying in the dark.

Elemental Analysis: Calcd. for $C_{54}H_{45}NO_3P_3Ag$: C, 67.79; H, 4.74; N, 1.46. Found: C, 67.91; H, 4.72; N, 1.53.

^{31}P NMR (Dichlormethane-d_2, 444324, Sigma-Aldrich) δ(chemical shift): 8.06ppm.

Precursor ***2*** (*R*= –Cl): Stoichiometric quantities of silver nitrate (17.0 mg), triphenylphosphine (78.7 mg) and tetraethylammonium chloride hydrate (113042, Sigma-Aldrich) (33.2 mg) are added to warm acetonitrile (10 mL). Crystals form by slowly cooling the solution. After washing with acetonitrile and drying under nitrogen, the white crystals are stored in a dark, dry atmosphere.

Elemental Anallysis: Calcd. for $C_{54}H_{45}P_3ClAg$: C, 69.73; H, 4.88; P, 9.99; Cl, 3.81. Found: C, 69.55; H, 4.82; P, 10.01; Cl, 3.68.

^{31}P NMR (Dichlormethane-d_2) δ(chemical shift): 3.34ppm.

2.2 Synthesis and Characterization of *MT*- and *SC*- NPs

We have discovered that mono-dispersed silver NPs (the size variation is less than 5%) with size between 8 to 20 nm can be obtained by one-step single phase synthesis, by the reduction of air stable $(PPh_3)_3Ag–R$ with amine molecules $(–NH_2)$ at elevated temperature in organic solvents. In a typical experiment, the $Ag(PPh_3)_3–R$ molecular precursor is dissolved in anhydrous *o*-dichlorobenzene (240664, Sigma-Aldrich) under helium. After the clear solution is heated to the desired temperature oleylamine (129540010, Acros) is quickly injected into the solution with vigorous stirring. The synthesis conditions for selected sized twinned and single crystalline NPs are summarized in Table 2.1 and 2.2 below. Oleylamine serves as both reducing agent and capping ligand for the NPs. Compared with other inorganic reducing agents, oleylamine has a less reducing ability. This slows the reducing rate of silver cations, allows control over the growth and ultimately leads to narrow size distribution [70]. Once the concentration of reduced silver monomers in solution is high enough, silver monomers follow the conventional synthetic scheme, which involves rapid homogeneous nucleation and growth, followed by self size focusing to achieve the narrowest size distribution and slower ripening which means the size distribution gets broader. The formation of Ag NPs is evidenced by slow color change of the solution from clear to bright yellow. The NPs can be precipitated out of solution by adding methanol after the reaction is stopped by cooling to room temperature. The NPs can also be re-dispersed in other non-polar organic solvents, such as toluene, for later use.

Table 2.1 Synthesis of different sized *MT*-NPs follows the general procedure described above with precursor ***1***.

Size (nm)	8.8 ± 0.3	13.9 ± 0.5
Precursor *1* (mmol)	0.05	0.19
***o*-dicholorbenzene (ml)**	17.0	19.0
Oleyamine (mmol)	7.2	3.6
Temperature (°C)	174.0	150.0
Reaction time (mins)	30	120

Table 2.2 Synthesis of different sized *SC*-NPs follows the general procedure described above with precursor ***2***.

Size (nm)	14.0 ± 0.6	20.0 ± 0.9
Precursor *2* (mmol)	0.19	0.19
***o*-dicholorbenzene (ml)**	19.0	19.0
Oleyamine (mmol)	3.6	3.6
Temperature (°C)	140.0	150.0
Reaction time (mins)	120	240

2.3 Electron Microscopy Characterizations

In order to characterize synthesized NPs and to understand their structure we used the JEOL 2100F and 4000FX field emission transmission electron microscopes (TEM) at the Maryland NanoCenter.

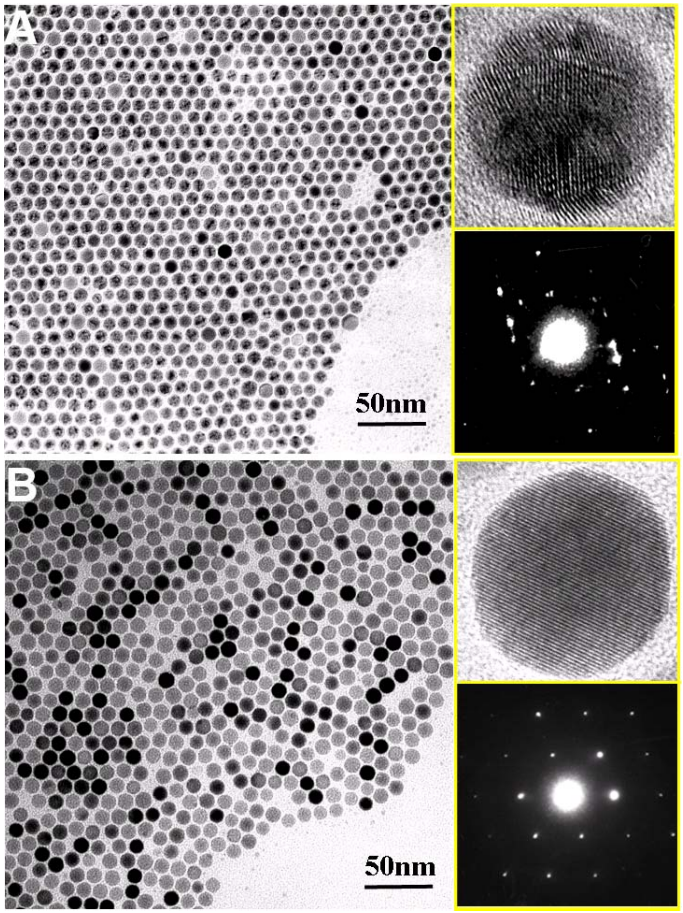

Figure 2.3 Large scale (left) and high resolution TEM (top-right) images and SPED patterns (bottom-right) for two identical sized (A) *MT*- and (B) *SC*-silver NPs. In the large scale images, the NPs having twinning defects can diffract the electrons into the angular range selected by the objective aperture, the remaining parts of the NP show darker contrast. The different contrast of the *SC*-NPs is caused by different crystal orientation. From the measurements, we can safely conclude that nearly 100% of the silver NPs synthesized by precursor ***1*** possess *MT*- structure, while nearly 100% of the NPs with *SC*- structure are obtained by precursor ***2***.

Figure 2.3 A and B (left), show typical large scale TEM images of silver NPs with an average diameter of 10.6 ± 0.4 and 10.5 ± 0.4 nm, synthesized from precursors with R*1* and R*2*, respectively, These NPs have not undergone size selection. The difference between these two large scale TEM images can be immediately addressed. The clear inhomogeneous feature developed in all the NPs presented in the Figure 2.3A can be attributed to the existence of twinning defects in silver NPs, while all the NPs in Figure 2.3B are homogeneous.

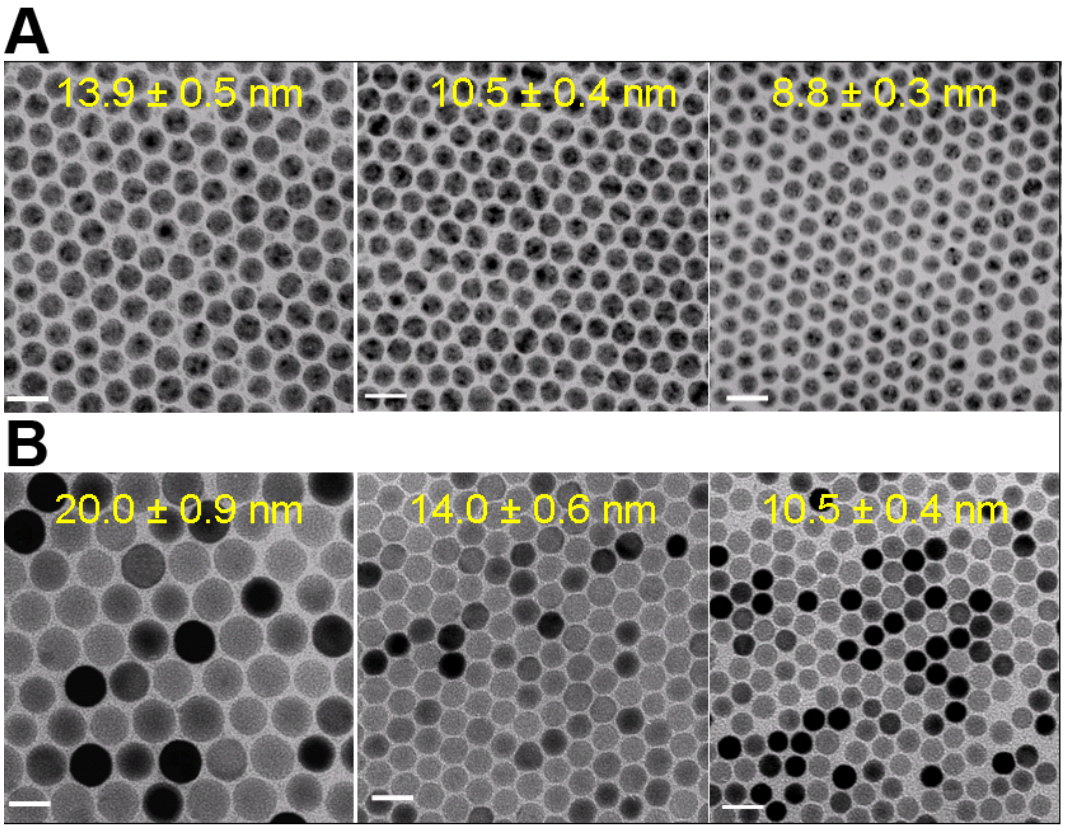

Figure 2.4 TEM images of different sized (A) *MT*- and (B) *SC*- silver NPs. The white scale bars in the images are all 20 nm. The yellow number is the average size of NPs shown in the images.

In the TEM experiment, the NPs with twinning defects can diffract the electrons into the angular range selected by the objective aperture and the remaining parts of the NP show darker contrast. The different contrast of the *SC*-NPs is caused by different crystal orientation [83]. The single crystallinity of silver NPs can be further indentified with high resolution TEM and Single Particle Electron Diffraction (SPED) characterization shown in Figure 2.3 A and B (right). Different size NPs with well defined crystallinity can also be synthesized, shown in Figure 2.4.

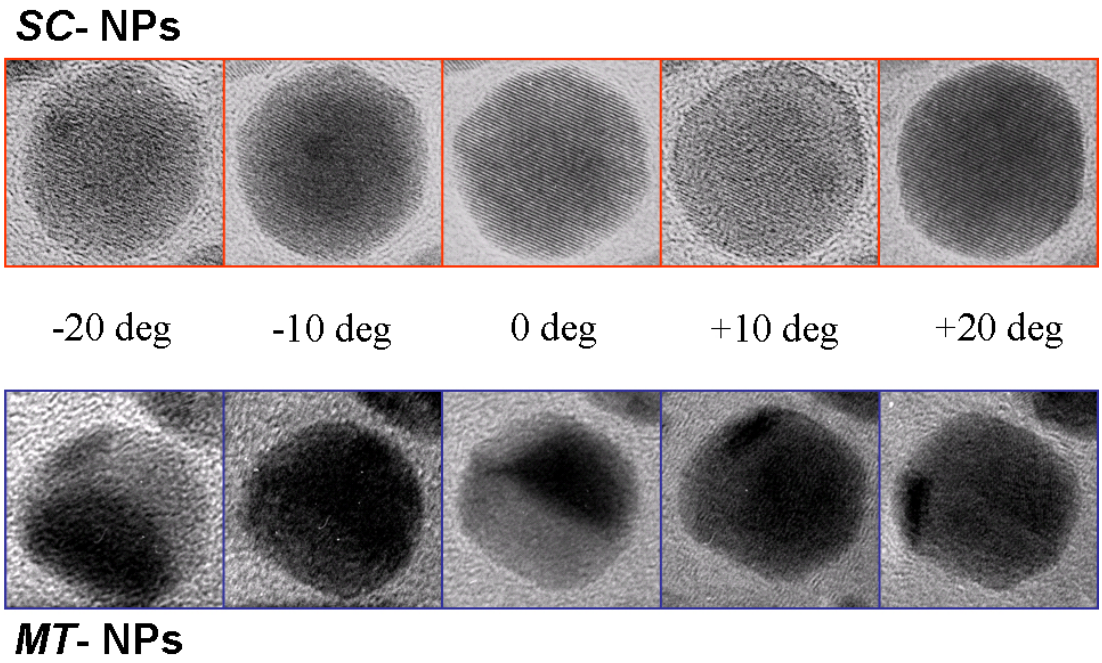

Figure 2.5 Angle dependent TEM images of 10.5 nm *SC*- and *MT*- silver NPs. It is clear that the perfect lattice of the *SC*-NP does not depend on the angle, but the contract of the *SC*-NP does. The image is dark when the *SC*-NP is at +20 deg, and lighter at +10 deg. For the *MT*-NP, the twinning defects can not been noticed clearly on some of angles (-10 deg and +20 deg, for examples).

Occasionally TEM and SPED images are not sufficient to provide accurate information on the crystallinity of NPs due to, for example, chemical coatings on the surfaces or NP orientation. In order to characterize and define unambiguously crystallinity of as-synthesized NPs, we also have carried out angle dependent TEM measurements to confirm the difference between *MT*- and *SC*- NPs, as shown in Figure 2.5. For *SC*-NPs homogeneous atomic lattice structure can be observed at all angles, while the contrast of inhomogeneous lattice structures in *MT*-NPs is angle dependent.

2.4 Discussion on Mechanism

To elucidate the mechanism of crystallinity control, we characterize the time evolution of growth of both silver *MT*- (Figure 2.6) and *SC*- (Figure 2.7) NPs. For the synthesis with both precursor ***1*** and ***2***, we observed very small silver *SC*- and *MT*-nuclei (~3 nm) at the early growth stage (the top-left images of Figure 2.6 and 2.7). This agrees with previous theoretical and experimental studies (Figure 2.1). It is believed that *MT*- nuclei typically possess smaller surface and volume energies that favor growth to large size [9, 80]. With time, the *MT*-NPs follow the conventional synthetic scheme [9, 70, 78]. When the functional group of the precursor is replaced with –Cl, precursor ***2*** not only serves as a silver source but also provides abundant Cl^- ions after reduction. The Cl^- ion is easily bound to defect sites (due to higher energy) and thus inhibit continuing growth of nuclei with *MT*- structure. Therefore only

nuclei with *SC*- structures can continue to grow to large size and participate in the conventional synthetic scheme (Figure 2.2). This mechanism is further supported by our control experiments showing that if the growth rate of NPs is increased by either higher reaction temperature or higher oleyamine concentration the Cl^- ion may not efficiently inhibit the growth of all *MT*- structure thus leading to mixtures of *SC*- and *MT*- NPs (Figure 2.8).

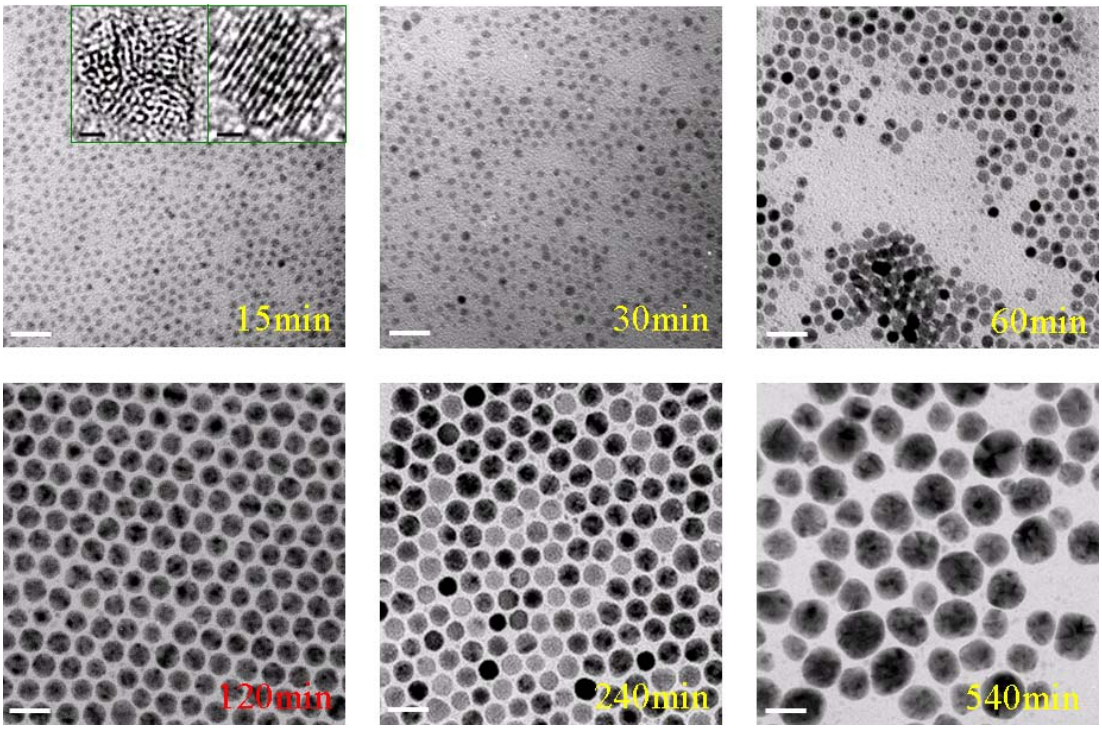

Figure 2.6 Time evolution of growth of *MT*-NPs characterized by TEM. The white scale bars in the images are all 20 nm, and the black bars in the small inset images are 3 nm. Time dependent TEM images are taken after the injection of 3.6 mmol oleylamine into 0.19 mmol precursor ***1*** in 19 ml of o-dichlorobenzene at 140°C. The 15min image shows the coexistence of *SC*- and *MT*- nuclei. With time, nuclei grow to large size which following a conventional synthetic scheme. The narrowest size distribution (≤5%) for this synthesis occurs at 120mins. After that, the NPs keep growing but the size distribution becomes broader slowly.

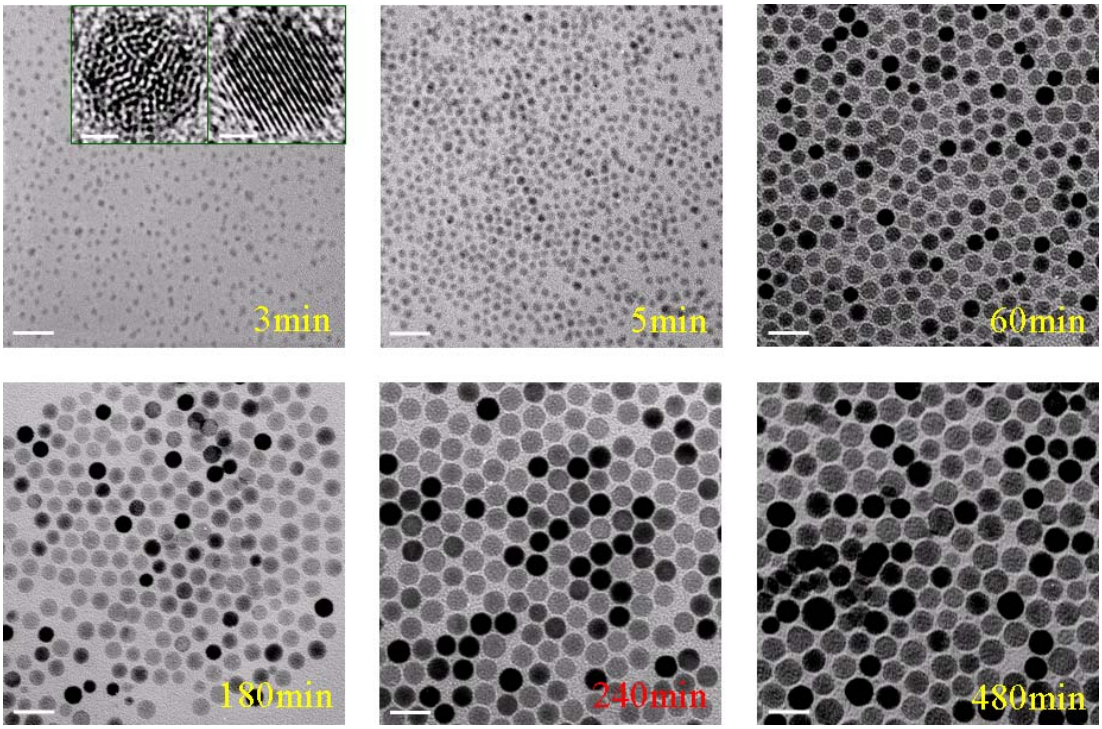

Figure 2.7 Time evolution of growth of *SC*-NPs characterized by TEM. The white scale bars in the images are all 20 nm, and the black bars in the small inset images are 3 nm. Time dependent TEM images are taken after the injection of 3.6 mmol oleylamine into 0.19 mmol precursor ***2*** in 19 ml of o-dichlorobenzene at 140°C. The 3min image also shows the coexistence of *SC*- and *MT*- nuclei. With time, only *SC*- nuclei grow to large size which follows conventional synthetic scheme, The Cl^- ions inhibit continuing growth of *MT*-nuclei. The narrowest size distribution (≤5%) for this synthesis occurs at 240mins. After that, the NPs keep growing but the size distribution becomes broader slowly.

The advantages of using metal-phosphine complexes as silver sources for NP synthesis include: facile synthesis, well-defined molecular structure and stoichiometry, solubility in organic solvents, a key point for the syntheses of mono-dispersed NPs, and flexible choice of central metal ion and functional R group. These provide a new and versatile route to kinetically controlled synthesis of metal NPs.

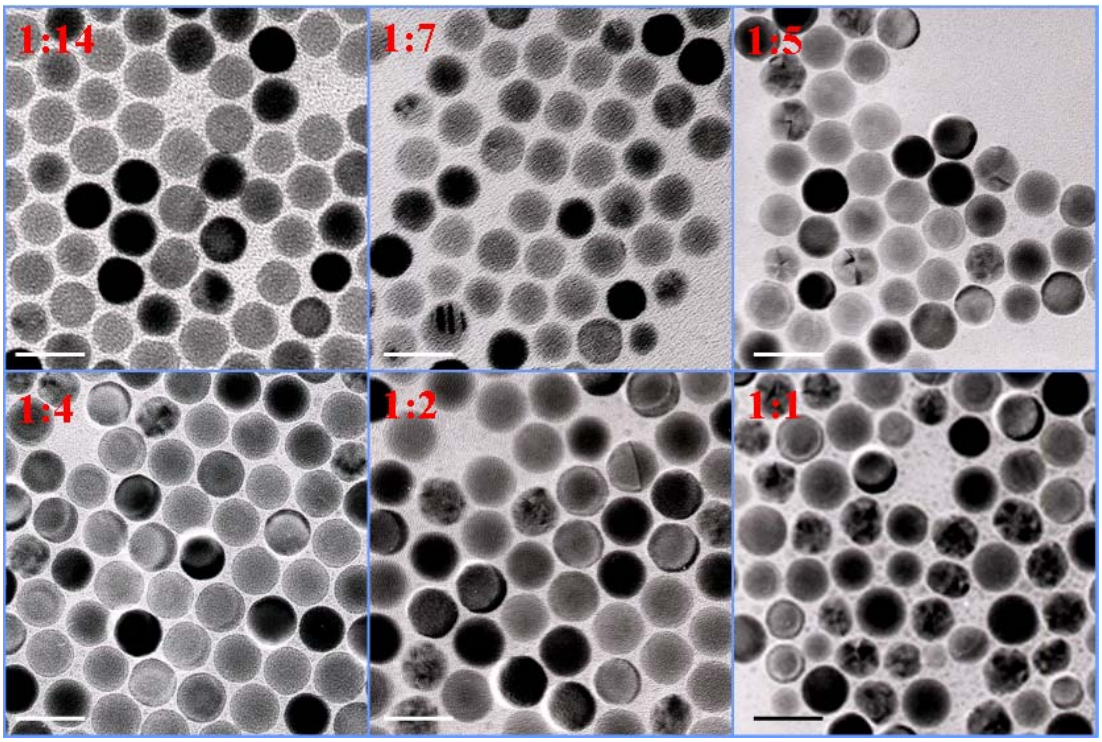

Figure 2.8 Mixture of *MT*- and *SC*- NPs. Mixture of *MT*- and *SC*- NPs can be achieved in a single reaction with different ratio of *MT*- to *SC*- NPs (the red number) by simply tuning the ratio of reducing agent to precursor amounts. (The scale bars in the images are all 20 nm.)

3. Significance of Nanocrystallinity Control

As compared with current available techniques, our technique has an additional level of synthetic nanocrystallinity control through judicious choice of the functional group of the organic molecular precursors. Our technique should facilitate the investigation of NPs for fundamental chemistry and physics as well as for practical device applications. Using a variety of experimental techniques we have carried out

in- depth investigations of synthesized silver *SC*- and *MT*- NPs, revealing how structural defects govern chemical functionalities, electron-phonon interactions and mechanical properties as well as performance of molecular sensing devices at the nanoscale. These studies provide a rational pathway for the understanding and controlling the intrinsic properties and functionalities of metal NPs through nanocrystallinity engineering and for further optimizing device performance fabricated from these nanoscale building blocks.

3.1 Role of Nanocrystallinity on Nanoscale Material Chemistry

Recent progress in the synthesis of NPs has sparked significant interest for template directed solid state chemistry at the nanometer scale in which the NPs can be chemically transformed into novel complex nanostructures. At the nanometer scale, the thermodynamics and kinetics of the chemical reactions are dramatically different from those in bulk materials due to the different free energy and reactivity of atomic sites within the NPs. Understanding how chemical transformation can be manipulated by defect engineering within NPs will be vital for the optimal use of chemical transformations to create building blocks with novel properties and functionalities [89-92]. We start with as-synthesized 10.5 nm silver *SC*- and *MT*- NPs as templates and perform a direct chemical reaction of these two different kinds of Ag NPs with Se powder in *o*-dicholorbenzene solution at 45 °C. Figure 2.9 highlights the HRTEM image and SPED characterizations of single NPs before and after the reaction.

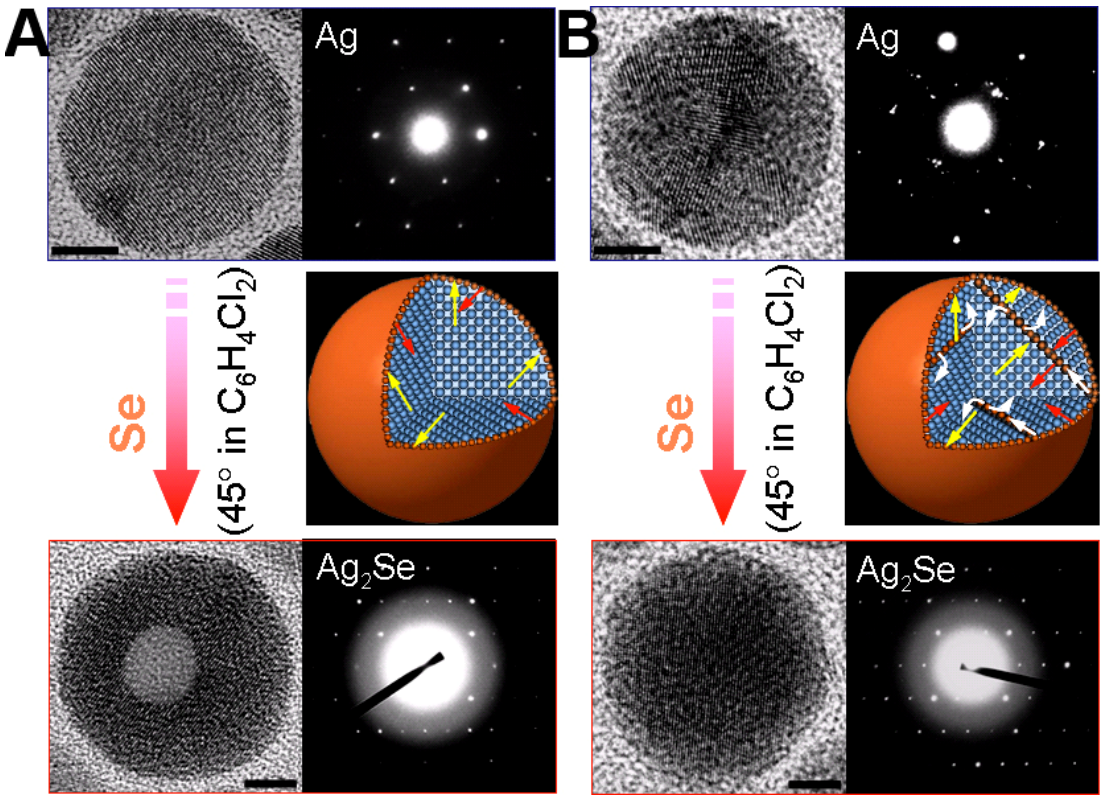

Figure 2.9 Chemical transformation of 10.5 nm silver *SC*- and *MT*- NPs to Ag_2Se nanostructures at 45°C in *o*-dicholorbenzene. (A) Typical High Resolution Transmission Electron Microscope (HRTEM) image (top-left) and Single Particle Electron Diffraction (SPED) (top-right) of *SC*-NP and schematic diagram of atom diffusion paths (middle); typical HRTEM image (bottom-left) and SPED (bottom-right) of *SC*-Ag_2Se NP with hollow core. (B) Typical HRTEM image (top-left) and SPED (top-right) of *MT*-NP and schematic diagram of different atom diffusion paths (middle); typical HRTEM image (bottom-left) and SPED (bottom-right) of solid *SC*-Ag_2Se NP. Blue and orange spheres represent silver and selenium atoms, respectively. Yellow and red arrows represent outward silver diffusion and inward selenium diffusion through the lattice, respectively. The dark grey spheres (behind some of the orange spheres) highlight silver atoms in the twinning boundaries, providing another fast atom diffusion path for both silver and selenium atoms (white arrows). Scale bars in the HRTEM images are all 5 nm.

For the silver *MT*-NPs we observe formation of solid, perfect single crystalline Ag_2Se (Figure 2.9, Right), while for the reaction started with *SC*-NPs single crystalline Ag_2Se with a well defined hollow core can be obtained (Figure 2.9, Left). For the selenization process with silver *SC*- NPs we find that the diameter of the hole inside the NPs is 20-40% of the final particle size.

The observed differences in Figure 2.9 suggest two different nanometer scale chemical transformations. We believe that formation of hollow cores after chemical transformation of *SC*-NPs follows a mechanism analogous to the Kirkendall effect, in which the diffusion speed of Ag atoms is faster than that of Se atoms during the reaction. This leads to vacancy formation and vacancy condensation into a single hole by crystal relaxation [92]. However, when many twinning defects exist in the silver NPs, the outward and inward transport of atoms and vacancies may take place in a hierarchical order: (i) transport along the surface (and surface layers) (ii) lattice diffusion; and (iii) transport along the twinning boundaries. The first two cases resemble the kinetics of the Kirkendall effect. The third case may be important for atom diffusion when Se reacts with *MT*-NPs because twinning boundaries are believed to act as easy diffusion paths called "Pipe Diffusion" [93] for both Se and Ag, which may balance the outward and inward flows of atoms and diminish the formation of vacancies. In addition, defects in the core of *MT* Ag NPs will also help to anneal vacancies. Perfect single crystalline Ag_2Se NPs are the only products of the chemical transformation of *MT*-NPs.

3.2 Role of Nanocrystallinity on Fundamental Physical Processes

Knowledge of fundamental electron and phonon interactions at the nanometer scale is central for understanding many new properties of nanomaterials and represents the key for fully exploiting quantum confinement effects. Extensive studies have been carried out on metal NPs, yielding, for example, information on intrinsic electron and phonon coupling, however, the results are contradictory [46, 94-101].

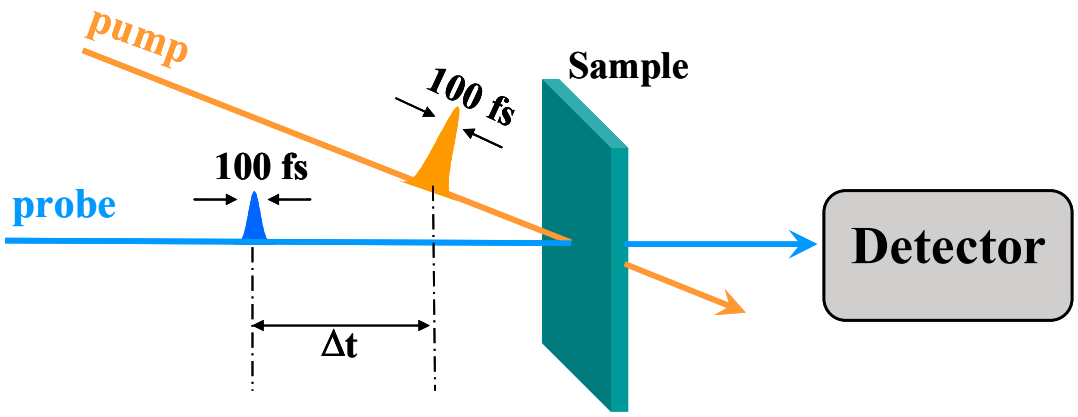

Figure 2.10 Schematic drawing of two-color (Pump-probe) time-resolved optical measurement setup. A first energetic pump pulse, resonant with an electronic or vibrational transition of the system under study, perturbs the absorption by the sample; the system evolution following excitation is monitored by measuring the transmission change of a delayed, weak probe pulse. The probe can be either an attenuated replica of the pump pulse, obtained by a beam splitter (degenerate pump–probe) or a pulse with a different color (non-degenerate or two-color pump–probe). One usually detects the pump-induced variation of the probe energy, measured by a slow detector, as a function of the time delay (Δt) between pump and probe pulses.

Using time resolved spectroscopy, we show for the first time that fundamental electron and phonon properties of silver NPs are dramatically modified at the nanometer scale by defect engineering. Two-color femtosecond pump-probe measurements (Figure 2.10) are systematically performed in both silver *SC*- and *MT*-NPs dissolved in toluene solution at room temperature. For 10.5 nm sized silver NPs, the Localized Surface Plasmon Resonance (LSPR) energy (~3.1eV) is well separated from the interband transition (~4.0eV, $4d \rightarrow 5sp$ transition), allowing measurements at off-resonance to achieve a weak perturbation regime. A 100-fs laser pulse with 250-kHz repetition rate is used to excite electrons from below to above the Fermi energy, generating a non-thermal equilibrium electron distribution (Insert, Figure 2.11A). At a delay time Δt, a probe pulse with energy tuned to around LSPR (providing high sensitivity due to the remarkable strength of the LSPR absorption) measures the time dependent pump induced transmission change ($\Delta T/T$, T is the temperature). Typical time resolved $\Delta T/T$ data obtained from two control *SC*- and *MT*- samples under similar experimental condition are shown in Figure 2.11A. For both samples, time resolved data clearly show inter-correlated energy transfer processes with different dominant interactions in characteristic timescale as follows: (1) the short time delay ($t \leq 0.5$ps) behavior of $\Delta T/T$ corresponds to electron-electron (*e*-*e*) scattering and correlated thermalization dynamics of non-equilibrium conduction electrons after pump excitation; (2) the follow-up fast exponential decay ($0.5 \leq t \leq 4$ps) can be attributed to energy exchange of electrons with the lattice mainly through electron-phonon (*e*-*ph*) coupling process, whose decay constant allows direct measurement of *e*-*ph* interaction time; (3) on a longer time scale ($t \geq 4$ps) the process is

mainly dominated by phonon-phonon (*ph-ph*) interactions and energy (heat) dissipation from NPs to the local environmental matrix.

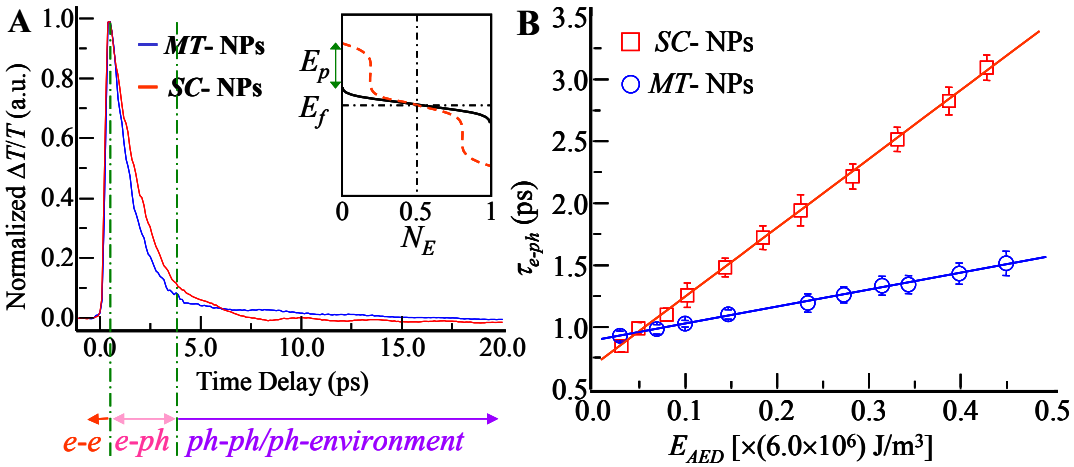

Figure 2.11 Time-resolved measurements of 10.5 nm silver *MT*- and *SC*-NPs. (A) Normalized optical transmission change ($\Delta T/T$) as a function of time delay (Δt). Red and blue curves are experimental data from *SC*-NPs recorded at the absorbed pump laser energy density E_{AED} =1.38×106 Jm^{-3} (which is near to the Localized Surface Plasmon Resonance of the 10.5nm *SC*-NPs) and from *MT*-NPs acquired at E_{AED} =1.44×106 Jm^{-3}, respectively. The inset shows the equilibrium electron distribution of NPs (blue line) and the perturbed one after absorption of pump pulse energy (E_p) (orange dashed line); E_f and N_E represent the Fermi energy and the density of states, respectively. (B) Experimental E_{AED} (the absorbed pump laser energy density) dependence of τ_{e-ph} (the *e-ph* relaxation time) for both *MT*- and *SC*-NPs. τ_{e-ph} is obtained by fitting to the time-resolved $\Delta T/T$ trace. Red and blue lines are linear fits to data for *SC*- and *MT*-NPs, respectively. The error bars are derived from the best fit to the experimental data set.

As known, the *e-ph* coupling constant (G) is important for understanding the nature of nonequilibrium electron relaxation. The superconducting transition temperature depends most strongly on the electron-phonon coupling constant G. Large G causes faster dynamical response, which provides efficient scattering of the

excited electrons. To further quantify *e-ph* interaction within NPs and gain more physical insight we estimate based on a two-temperature model by relating the *e-ph* relaxation time (τ_{e-ph}) to the absorbed pump laser energy density (E_{AED}) by a single particle as [99]:

$$\tau_{e-ph} = \left(\frac{\gamma T_0}{G}\right) + \left(\frac{1}{T_0 G}\right) E_{AED}$$

where γ is electronic specific heat and T_0 is room temperature. Experimentally, $\tau_{e\text{-}ph}$ can be determined by fitting the experimental of ($\Delta T/T$) data (Figure 2.11A) with the convolution of the theoretical response function and instrument response function. In previous studies G values were obtained by extrapolating experimental data to obtain intercept and then obtaining G in order to eliminate ill-characterization and non-reproducibility of experimental conditions (such as sample concentrations and laser intensity). In our measurement we can determine sample concentration accurately (3%) and carry out all measurements under the same conditions, therefore we are able to normalize our pump laser intensity to the absorbed energy density (E_{AED}) of a single particle and obtain G by fitting with slope by the given equation , which we believe provides a more accurate value of G. Indeed, our experimental data fit well the predicted linear dependence (Figure 2.11B) and yield a G value of $(1.49\pm0.22)\times10^{16}$ $JK^{-1}m^{-3}s$ and $(3.66\pm0.54)\times10^{15}$ $JK^{-1}m^{-3}s$ for *MT*- and SC- *NP*s, respectively.

The G value of *MT*-NPs is in good agreement with the range determined in previous reports [97, 99], and thus provides an additional consistency check in our work. However, our measured G value for silver *SC*-NPs is about 4 times smaller than that of *MT*-NPs, which suggests a significant enhancement of *e-ph* scattering within the *MT*-NPs due to the existence of twinning boundary.

The time resolved measurements also provide valuable information on the low frequency acoustic vibration modes of NPs that are a unique signature of their structural and mechanical properties that are extremely difficult to observe with spontaneous Raman spectroscopy. In our experiment, low frequency acoustic vibration modes are impulsively excited by a rapid expansion of silver NPs by absorption of a femto-second pump pulse [99]. The vibrations are described as weak oscillations superimposed on a slowly decaying background, due to modulation of electronic properties by coherent mechanical oscillation. These have been recently reported in semiconductor and metallic nanostructures. Figure 2.12A highlights a portion of the data (≥ 5ps) in Figure 2.11A after removing the residual exponential background from the *e-ph* scattering process. The oscillations characteristic of the fundamental breathing mode of acoustic phonon vibration in both *MT*- and *SC*- NPs are clearly revealed. We fit the oscillation pattern with a phenomenological response function: $A(t) = A_0 e^{(-t/\tau_m)} \cos\left(\frac{2\pi t}{T_{br}} + \phi\right)$, where A_0 is amplitude, τ_m is the decay time of energy transfer time from NPs to the local surrounding medium, ϕ is the phase, and T_{br} is the oscillation period. As shown in Figure 2.12B, oscillation periods extracted

from both samples show no dependence on E_{AED} or on solvents in our weak perturbation regime. The averaged periods are 3.55 ± 0.02ps and 4.16 ± 0.02ps, for *SC*- and *MT*- NPs, respectively. The observed acoustic phonon vibration period can be related to the elastic modulus of NPs through $T_{br} = \frac{2\pi R}{\xi_0 \sqrt{Y/\rho}}$, where ξ_0=2.85 for silver, ρ=10.5g/cm^3 is the density of silver, R is radius of NPs and Y is elastic modulus. We find that the elastic modulus, *Y,* of silver NPs increases about 37% from *MT*-NPs (81 ± 5 GPa) to *SC*-NPs (111 ± 7 GPa). While it is generally believed that defects can degrade macroscopic mechanical properties and smaller materials (such as one dimensional nanotubes) have been observed to have mechanical strengths considerably greater than those of their macroscopic counterparts due to a reduction in the number of defects per unit volume [102-106], our results provide the first direct evidence of the dependence of nanomechanics on defects at the nanometer scale.

3.3 Role of Nanocrystallinity on Nanoscale Device Applications

Our time resolved measurements performed on silver *SC*- and *MT*- NPs in the vicinity of LSPR provides fundamental insight into the physics of these nanometer scale systems as well as essential information for NPs based applications. One important application of plasmonic metal NPs is chemical and biological sensing based on the sensitive and stable LSPR spectral response to local environments. While many theoretical and experimental studies have been carried out to improve

NPs configuration to enhance their sensitivity of LSPR response (e.g., zeptomole (10^{-21}mol) sensitivity of silver NPs based optical sensors have been recently achieved for the detection of biomolecules) [68, 69, 107-117]. The dependence of sensitivity on the nanocrystallinity of plasmonic NPs has not yet been reported.

To illustrate the effect of twinning defects on LSPS dielectric sensitivity, we evaluate and compare the LSPR spectra of silver *SC*- and *MT*- NPs collected in various solvent environments. The results are summarized in Figure 2.12. We observe that for all of the solvents investigated the Full Width at Half Maximum (FWHM) of LSPR peaks of *SC*-NPs (0.29±0.01eV) are consistently smaller than that of *MT*-NPs (0.50±0.01eV), which suggests that twinning defects within *MT*-NPs play a critical role in the damping of LSPR of NPs. They significantly enhance scattering process on the basis of the frame of Mie theory (the linear relationship between NP's LSPR energy shift and environmental dielectric constant) [96], and agree with our time resolved measurements in Figure 2.11. Figure 2.13A shows a linear dependence of LSPR energy on refractive index, *n*, for both *SC*- and *MT*- NPs. This is similar to the tendency seen in previous reports of plasmonic based NPs sensor devices [115]. Linear regression yields experimental slopes, *m*, of (-0.55± 0.02) eV/RIU and (-0.33±0.04) eV/RIU, for *SC*-NPs and *MT*-NPs, respectively, where RIU is the refractive index unit. To further evaluate device performance of chemical sensors based on *SC*- and *MT*- NPs we define a "Figure-Of-Merit" (*FOM*) as follows [115]: $FOM = \frac{|m|\ (eV/RIU)}{FWHM\ (eV)}$, and we find that the *FOM* is improved by a factor of three

for SC-NP based devices (1.89 RIU^{-1}) as compared with *MT*-NP based devices (0.66 RIU^{-1}).

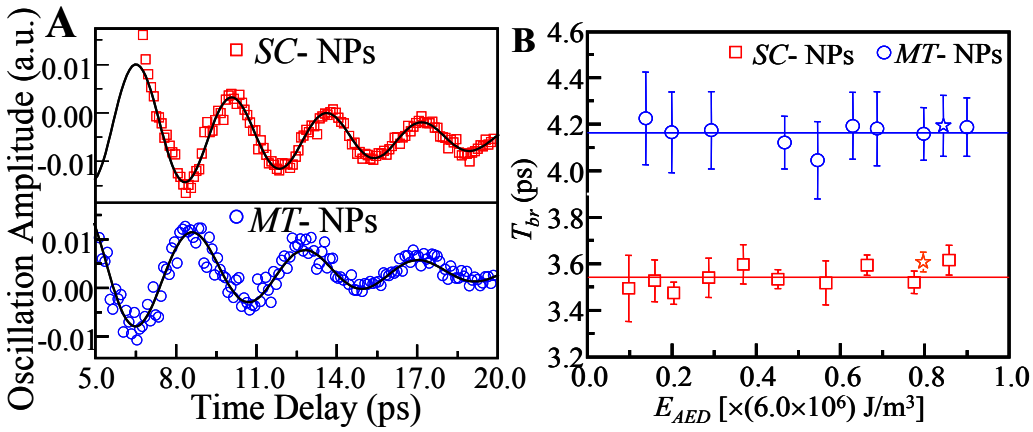

Figure 2.12 Time-resolved measurements of 10.5 nm silver MT- and SC-NPs. (A) Coherent acoustic-phonon oscillation modulation of $\Delta T/T$ data shown in Figure 11A on an enlarged scale, after removing the residual exponential background from the *e-ph* scattering process. Black lines are fits to experimental data. (B) Experimental E_{AED} (the absorbed pump laser energy density) dependence of acoustic-phonon oscillation period (T_{br}) for both *MT*- and *SC*-NPs. Red and blue lines represent the averaged period for *SC*- and *MT*-NPs, respectively. Red and blue stars are data acquired from *SC*- and *MT*-NPs dispersed in toluene, respectively. The error bars are derived from best fit to the experimental data set.

We also investigated the use of *SC*- and *MT*- NPs as molecular rulers, and compared LSPR energy response for molecular adsorbates of different lengths. After measuring the LSPR spectra of 0.5 mM silver NPs dispersed in chloroform, a 0.05 mmol straight chain alkanethiol molecules ($CH_3(CH_2)_xSH$, x=9~17) are injected into a cell under nitrogen and NPs are incubated in the solution for at least 10 hours to achieve stable and full coverage of self-assembled alkanethiol molecules on NPs

surface. Figure 2.13B shows the dependence of the LSPR energy shift (related to LSPR peak energy of NPs without the presence of molecular adsorbates) on alkanethiol chain length, *x*. The observed responses of both *SC*- and *MT*- NPs are linear with the length of the alkanethiol molecules. This agrees with Mie theory calculations performed on spherical NPs, however, the sensitivity of *SC*-NPs of 0.037eV for each additional methylene unit in the adsorbed molecules is almost three times higher than the of *MT*-NPs value of 0.014eV. The mechanism for much higher sensing capability of *SC*-NPs is not clear. One possibility is that occupation (packing density) of ligand and molecular adsorbates on the surface (as shell) of *MT*- NPs (as core) might be different from that of *SC*-NPs due to the existence of different surface crystalline facets in *MT*-NPs, giving a different effective refractive index immediately surrounding the NPs core. However, this effect will only induce constant LSPR peak energy shift instead of a sensitivity change. Further systematic studies will be necessary to provide more information on the sensitivity dependence of nanocrystalline structure which may be important for the future optimization of plasmonic metal NPs based molecular sensing devices.

4. Conclusions

In this chapter I address the important issue in nanoscience and nanotechnology of nanocrystallinty control of metal NPs. Our ability to synthesize mono-dispersed silver NPs with controlled crystalline structure opens up new opportunities, ranging

from fundamental solid state chemistry and physics to ultra-sensitive sensor applications at the nanometer scale. We further show that defect mediated chemical transformations allow a rational design of complex nanostructures if nanometer scale structural disorder is appropriately introduced to suppress or enhance competing mechanisms. Defect engineering can provide a means for precisely tailoring nanometer scale electronic and mechanical properties as well as controlling classical and quantum coupling interactions, ultimately leading to the optimization of device performance of defect-engineered NPs.

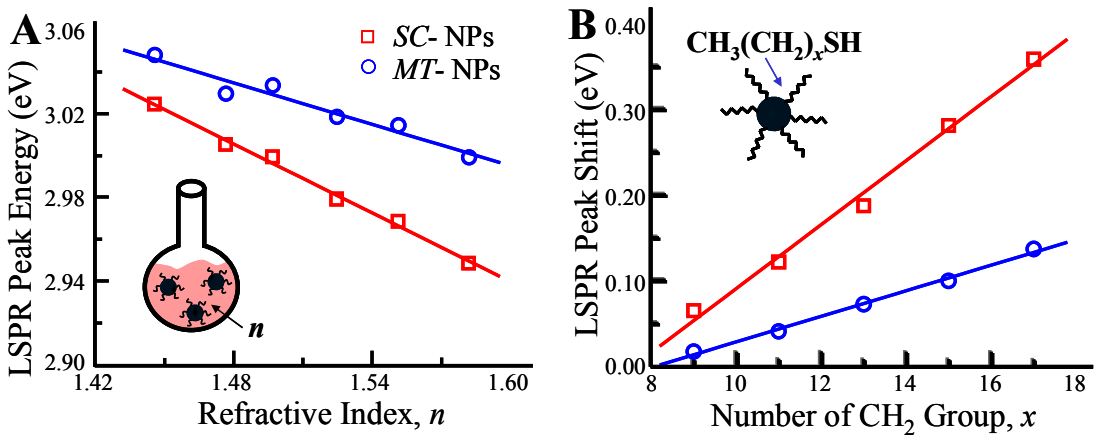

Figure 2.13 LSPR (Localized Surface Plasmon Resonance) energy shift of *MT*- and *SC*- silver NPs: (A) in different solvents with different dielectric constant; (B) with different capping ligand molecules.

Chapter 3: A Versatile Strategy for Precisely Tailored Core@Shell Nanostructures with Single Shell Layer Accuracy: the Case of Metallic Shell [2]

Core@shell nanostructures represent a unique constitution integrating different materials, properties and functionalities into a single unit. This class of nanostructures has shown enormous importance for both fundamental science and technological applications, including enhanced luminescence, biomedical, energy transfer, and fundamental couplings [118-123]. A key challenge here is the precise and tunable control of both core and shell dimensions and chemical compositions independently. So far the most successful examples to address this challenge are limited to certain semiconductor-core@semiconductor-shell structures by taking advantage of material epitaxial nature [124] while other types of core@shell combinations remain substantial technological challenges. In this chapter, I will describe a general well-controlled synthetic strategy to achieve meticulous control of metallic shell growth at the single monolayer level with versatile core nanoparticles (NPs), thus facilitating investigation of their scope for numerous applications. The key to the success of this strategy is to introduce an intermediate phase in a phase transfer reaction to finely tune shell growth process. Three categories of core NPs with distinct functionality, including metallic, magnetic, and semiconductor NPs, are chosen to demonstrate versatility of our approach. Enabled by such, we further highlight importance and tunability of plasmonic, optical and magnetic couplings with shell control.

---

2. This chapter was adapted from: Jiatao Zhang * , Yun Tang * and Min Ouyang. “A Versatile Strategy for Tailored Core@Shell Nanostructures with Single Shell Layer Accuracy: the Case of Metallic Shell”, *Nature Nanotechnoloy*, 2009, submitted. (* contributed equally to this work)

Furthermore, because the metallic shell can act as useful platform for converting to various compounds [7, 125], our methodology represents a facile and highly controllable synthetic pathway for complex nanostructures, thus is important for understanding and manipulating fundamental nanoscale chemical and physical property as well as assembling nanostructures with desirable structure and functionality.

*1. i*PAPER*: Principle and Synthetic Procedure*

Although advances in strategies for synthesizing plain NPs have achieved significant success in controlling size, composition, shape and even crystallinity [31], core@shell nanostructures have only obtained limited progress. Experimental challenges of achieving precise control of core@shell structures mainly include self-nucleation of shell components and inhomogeneous growth over core NPs, which set requirements of both slow growth rate of shell and controllable surface reactivity of core NPs. These requirements in principle could be met by using less active precursors for the shell component and surface chemical modification of core NPs [126-131], which have posed significant limitation to the choice of both core and shell materials. Our strategy, denoted as intermediate phase assisted phase exchange and reaction (*i*PAPER), however relies on controlling phase transfer reaction during the shell growth, as highlighted in Figure 3.1. Phase transfer mechanism has been demonstrated to be an attractive strategy for synthesizing a wide range of NPs

because it combines advantages of both aqueous and organic phase synthesis [132]. While a similar mechanism was also attempted for core@shell synthesis, there is no control of self-nucleation of shell component, thickness and monodispersity due to distinct polarity difference in the interface [133].

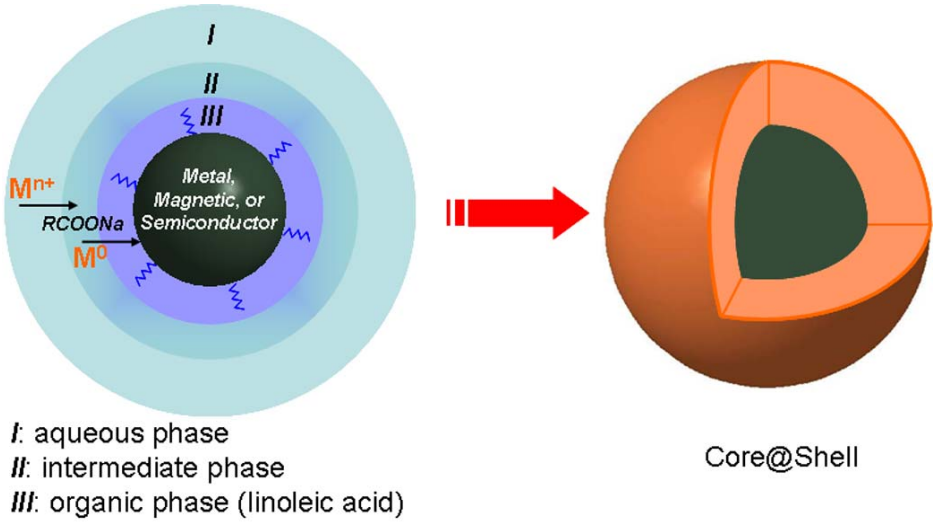

Figure 3.1 Schematics of *i*PAPER strategy for core@metal-shell synthesis.

The key to the success of our *i*PAPER method is the judicious choice of an intermediate phase reagent so that it can coordinate transport of ion (M^{n+}) and atom (M^0) species to govern shell growth dynamics and can have better compatibility with core NPs surface to ensure homogeneous growth. We start with monodispersed core NPs passivated with long chain alkyl ligands (e.g., oleic acid or oleylamine) as seeds that can be dispersed well in fatty acid (phase ***III***). Soluble metallic inorganic salts in distilled water (phase ***I***) are used as precursor for shell growth and can be available

for most transition or main group metal ions, which provide a wide range of shell composition as well as generality of our approach. In order to transfer metal ions from aqueous solution, sodium linoleate (RCOONa) has been demonstrated to be an effective phase transfer agent[17]. Several criteria need to be considered when choosing phase ***II*** reagent: (1) its polarity should be between those of phase ***I*** and ***III***; (2) it should be hydrophilic with charge-polarized heteroatom group; and (3) it should reduce adhesion energy of core NPs to allow dynamic solvation of surfactant molecules at the growth temperature to enable exposure of core NPs surface to shell atoms. Once the phase ***II*** reagent is identified, phase ***I*** with metal ions, sodium linoleate, phase ***II*** and ***III*** reagents are mixed together in a reaction vessel with vigorous stirring to form a macroscopic homogeneous thermostable mixture. Typically, a phase transfer process of metal ions would happen spontaneously in this mixture process via formation of metal linoleate through phase exchange. Appropriate reducing agent is thus introduced to the system to initiate shell growth process, and the shell thickness can be precisely controlled by reagent concentration and reaction time. An organic solvent such as toluene can thus be added to destroy the homogeneous mixture, stop shell growth and extract final core@shell product to the organic phase. To demonstrate versatility of this method we choose Au, FePt and Ag_2Se as representative metallic, magnetic and semiconductor core NPs respectively, and use Ag shell as example to highlight precise control of *i*PAPER technique. However, more combinations of core and shell can be available to further demonstrate generality of *i*PAPER.

*2. Characterization of Core@Shell by i*PAPER

TEM and EDS characterization: Samples for TEM characterization are prepared by adding one drop of core@shell solution in toluene onto 300 mesh copper grids with carbon support film (Ted Pella, 01820). JEOL 2100F and JEM 2100 LaB6 TEM are applied for size, morphology and ensemble EDS characterizations. Single-particle EDS measurement is operated under STEM mode with JEOL 2100F. Size distribution of NPs is determined by counting over 100 NPs based on TEM characterization.

Optical spectroscopy characterization: The UV-Vis spectroscopy measurement is carried out with commercial UV-Vis recording spectrophotometer (Shimadzu, UV-2501PC) with sample in a sealed 5mm- thick fused silica cell.

Magnetic property characterization: Magnetic property measurement of NPs is carried out in a Quantum Design SQUID Magnetometer (MPMS XL-7). The sample for characterization is in powder form and kept in a lock-ring capsule (Size 5, Torpac Inc.). All sample preparations are under nitrogen protection. ZFC and FC curves are typically obtained from 10mg sample with magnetic field of 500 Oe.

3.1 Metallic-Core@Metallic-Shell

Au@Ag is the first example to demonstrate *i*PAPER's principle and synthetic procedure. Different sized Au NPs passivated by oleic acid are synthesized following previous report [132], and are used as core for successive growth of Ag shell. In a typical synthesis of four monolayers of Ag shell with 2.8 nm core, 0.005 mmol Au core NPs are dispersed in the three-phase mixture of 6ml of H_2O, 4ml of ethyl glycol (EG), 0.4ml of oleic acid, and 0.3g of sodium oleate. In this reaction, EG acts as phase ***II*** reagent. After the mixture becomes clear and homogeneous by shaking, 1ml $AgNO_3$ aqueous solution is added drop by drop under vigorous stirring. 0.6ml of ascorbic acid solution is then added drop by drop to act as reducing agent. After 24 hrs' reaction, 10ml of toluene is injected into the mixture to stop reaction and extract Au@Ag to toluene.

Figure 3.2a shows a series of high resolution transmission electron microscope (TEM) images of Au@Ag core@shell structures with identical size of Au core NPs and the shell thickness continuously tuned from one- to nine- monolayers enabled by *i*PAPER.

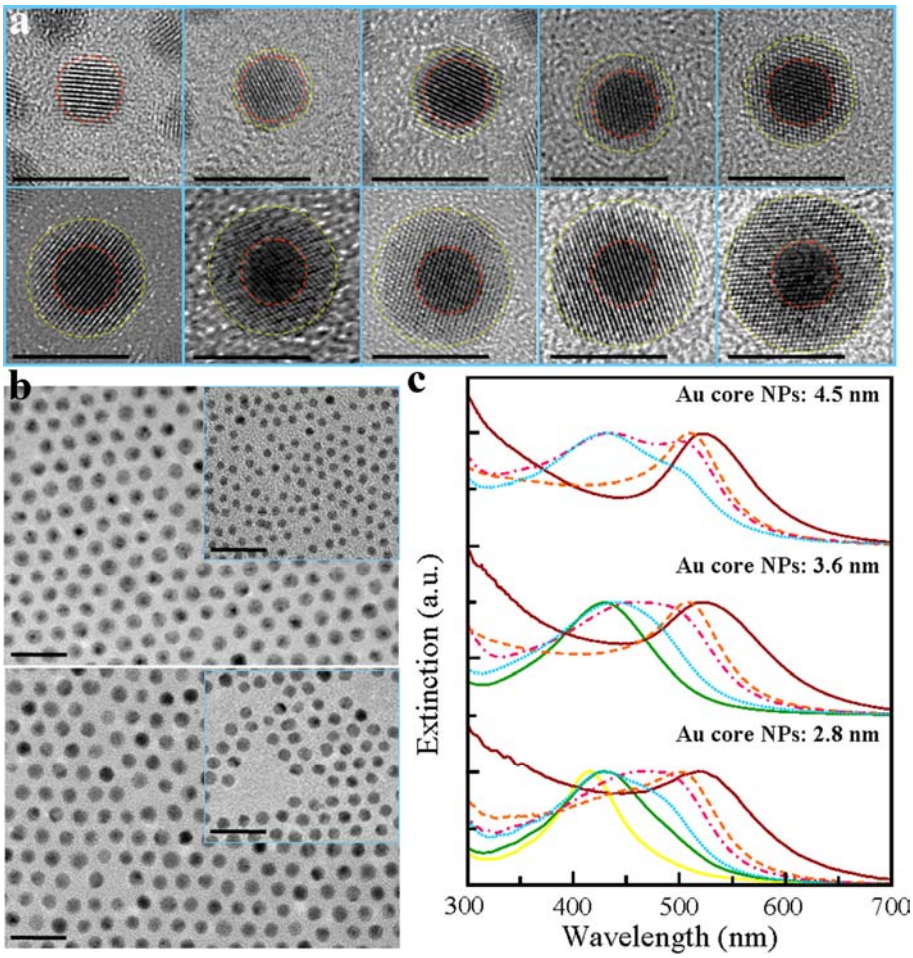

Figure 3.2 Precise and tunable control of Au@Ag nanostructure. a, Series of high resolution TEM images of Au@Ag, highlighting layer-by-layer control of shell thickness from zero- (plain Au core NPs) to nine- monolayers of Ag shell. Red and yellow dashed lines are guides to the eye for core- and shell-boundaries, respectively. Scale bar, 5nm. b, Large scale TEM images of Au@Ag with same overall size of 6.8 ± 0.3 nm after shell growth but from different Au core NPs, highlighting uniformity and independent core control. (TOP) Au@Ag prepared from core size of 2.8 ± 0.2 nm (Inset). (Bottom) Au@Ag prepared from core size of 4.5 ± 0.3 nm (Inset). Scale bar, 20nm. c, Evolution of optical spectroscopy of Au@Ag with different core size and shell thickness. Spectra from same Ag shell thickness are represented by same color and line pattern: dark red for plain Au core NPs; dash orange for one monolayer of Ag shell; dash-dot pink for two monolayers of Ag shell; dot blue for three monolayers of Ag shell; green for four monolayers; yellow for five monolayers. Maximum SPR peak intensity is normalized to the unit for comparing peak position and spectra are shifted vertically to show the difference between different core sizes.

Among of all bimetallic core@shell structures reported so far, Au@Ag system represents the one that has been studied most, however, for size below 10nm in which quantum effect can get pronounced there are no unambiguous reports of Au@Ag core@shell structures so far, which was partially due to the lack of control of miscibility between Au and Ag over the whole composition range in such size regime. In addition, since well-defined core NPs are applied as seed for successive shell growth, core and shell sizes can thus be independently tuned. Figure 3.2b compares large scale TEM images of two uniform Au@Ag structures with same overall size, but obtained from two distinct sized core NPs (Figure 3.3), further highlighting the quality and the monolayer shell tunability of bimetallic core@shell nanostructures enabled by *i*PAPER.

As compared with monometallic NPs, our ability of precise control of core@shell nanostructures facilitates novel pathways to improve stability and quality, and to understand and fine tune nanoscale property and functionality because of synergistic effect, including for example tunable catalytic and plasmonic properties. Because of dielectric confinement Au NPs as well as some other noble metals have shown pronounced surface plasmon resonance (SPR) effect, giving their optical property dramatically different from that of bulk. Figure 3.2c highlights evolution of SPR with both core size and shell thickness at the single monolayer level. We observe that SPR features of Au@Ag are significantly modulated layer-by-layer by Ag shell, and for shell thicker than five monolayers the SPR features of core@shell nanostructures are mainly contributed from silver component. However, while fine

spectra structures of SPR depend on both Au core and Ag shell, for the same shell thickness with different core sizes the overall peak features show the same, which further confirm shell layer control of *i*PAPER.

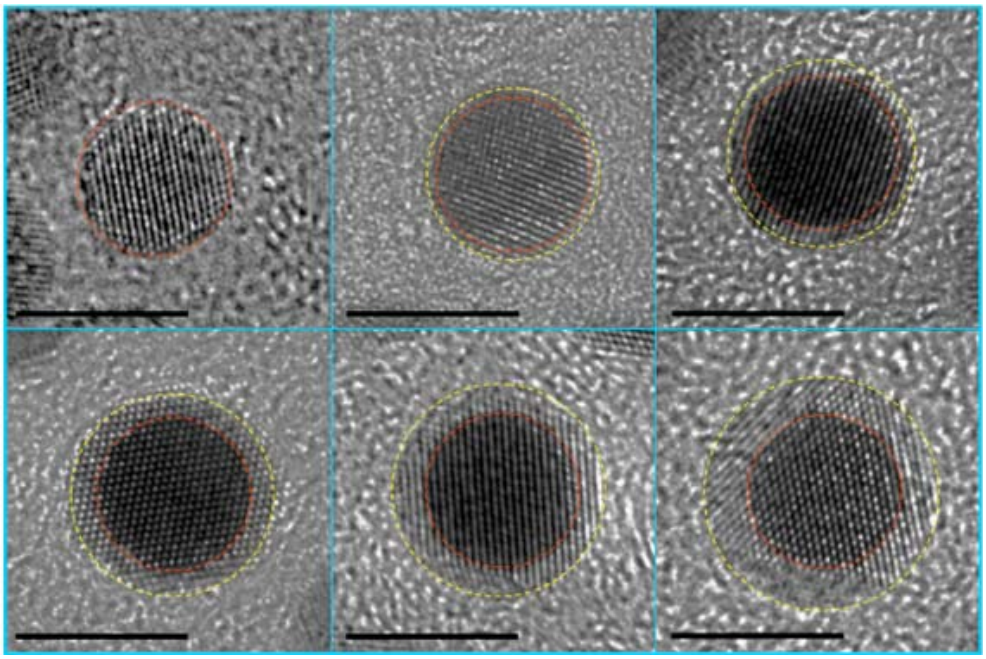

Figure 3.3 High resolution TEM images of Au@Ag with layer-by-layer control of Ag shell by *i*PAPER strategy. The size of Au core NPs is 4.5 ± 0.3 nm. Images from top left to bottom right correspond to *0*- to *5*- monolayers of Ag shell. Red and yellow dashed circles are guides to eye to highlight boundary of core and shell, respectively. Scale bars, 5nm.

Same control can also be applied to other systems possessing such as catalytic functionality (Figure 3.4), which might facilitate our future understanding and control of nanoscale catalysis by investigating monolayer shell dependence.

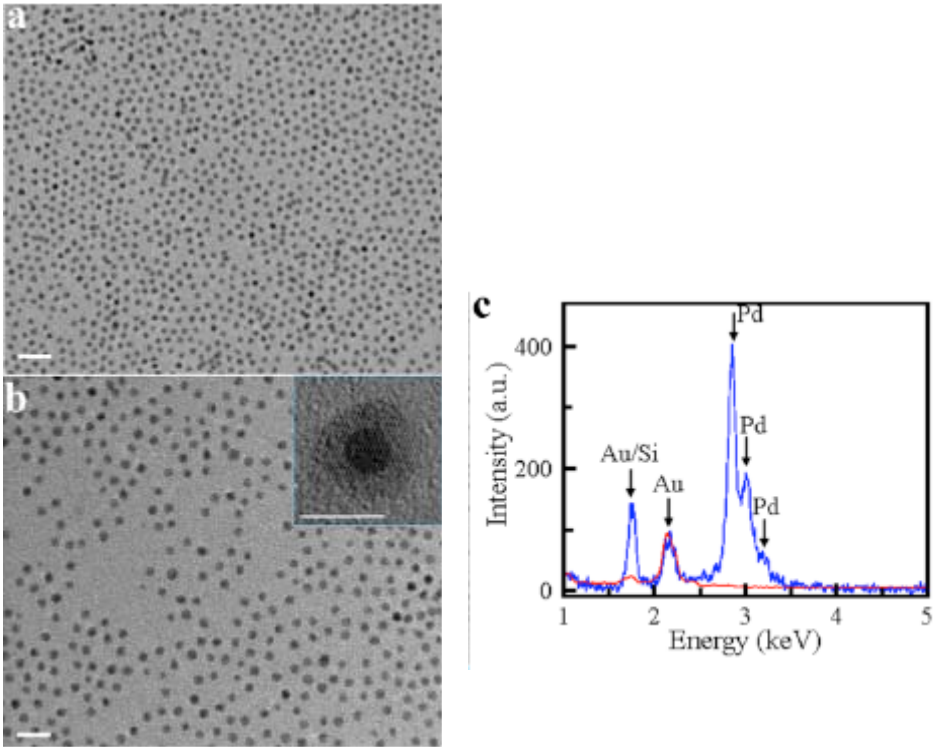

Figure 3.4 Synthesis and characterization of Au@Pd by *i*PAPER strategy. a, Large scale TEM image of 2.8 ± 0.2nm Au NPs. Scale bar, 20nm. b, Large scale TEM image of Au@Pd synthesized from Au core NPs shown in a. Scale bar, 20nm. Inset, high resolution TEM image of single Au@Pd, highlighting core and shell features. Scale bar, 5nm. c, Ensemble EDS measurements of plain Au core NPs (red) with Au@Pd (blue). Intensities of Au peak at 2.15 keV are normalized to be the same in order to compare peaks contributed from Pd element.

3.2 Magnetic-Core@Metallic-Shell

We further extend our *i*PAPER strategy to achieve similar precise control of magnetic core@shell nanostructures. Figure 3.5 shows the FePt@Ag synthesized by *i*PAPER.

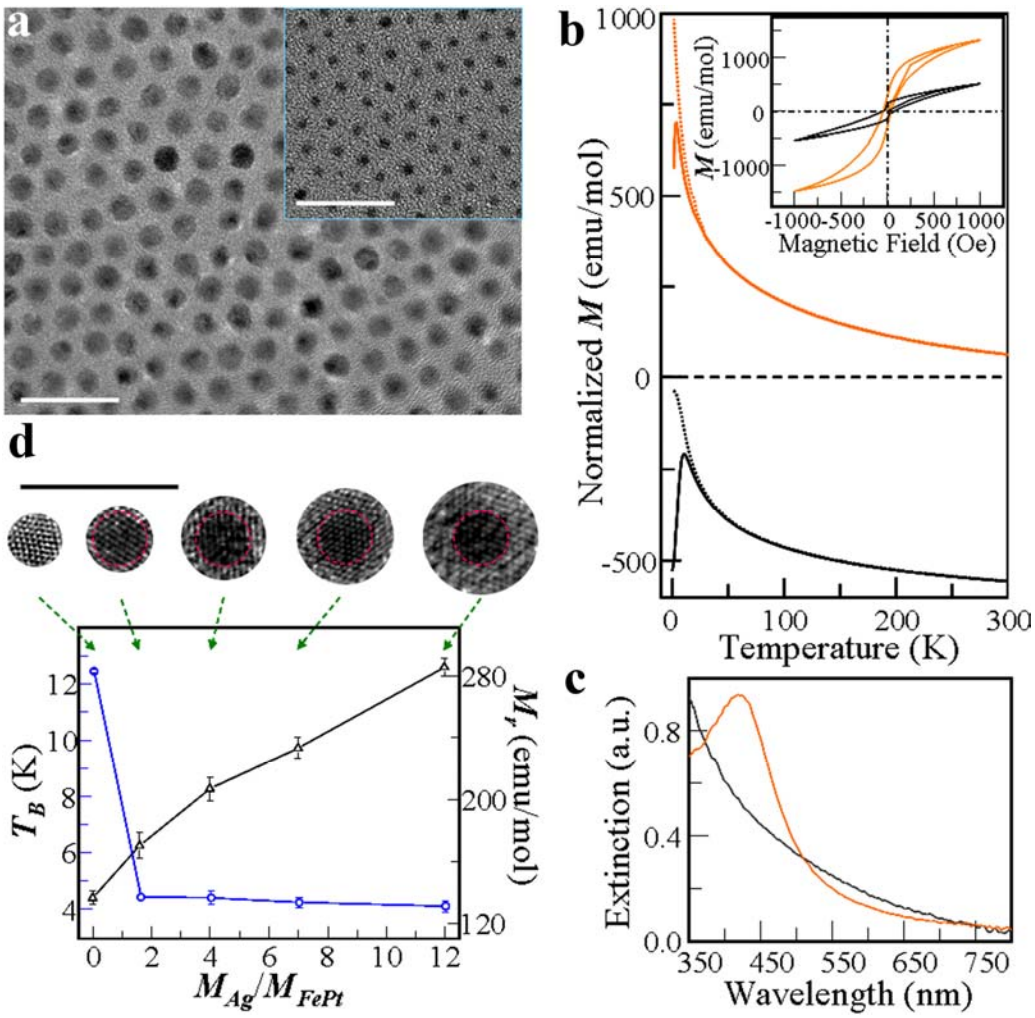

Figure 3.5 Precise and tunable control of FePt@Ag nanostructure. a, Large scale TEM image of 4.2 ± 0.2 nm FePt@Ag with three monolayers of Ag shell and 2.0 ± 0.1 nm FePt core (Inset). Scale bar, 10 nm. b, Zero-field cooling (ZFC) (solid line) and field cooling (FC) (dot line) magnetization curves of FePt NPs (lower, black) and FePt@Ag (upper, orange), respectively. Inset, normalized magnetization hysteresis loops at 3K: orange for FePt@Ag and black for FePt NPs. c, Optical extinction spectra of FePt NPs (black) and FePt@Ag with three monolayers of Ag shell (orange). d, Dependence of T_B (blue) and M_r (black) on Ag shell thickness which is represented by molar ratio between Ag shell (M_{Ag}) and FePt core (M_{FePt}). High resolution TEM images of FePt@Ag samples for magnetic property measurements are also shown, showing layer-by-layer control of thickness from zero- (plain core FePt NPs) to four- monolayers of Ag shell. Pink dashed circles are guides to the eye for the interface between core and shell. Scale bar, 5nm.

FePt core NPs are obtained by following Sun's method [79], and *N*, *N*-Dimethylformamide (DMF) is chosen as appropriate phase ***II*** reagent. In a typical synthesis of three monolayers of Ag shell with 2.8nm FePt core, 1mg of FePt NPs is added into the mixture solution of 6ml of H_2O, 4ml of DMF, 0.4ml of oleic acid and 0.3g of sodium oleate. The mixture is clear and homogeneous after sonification. 1ml of $AgNO_3$ is then added drop by drop to the mixture. After heating at 85°C with stirring for 14hrs 10ml toluene is added to stop and extract final product of FePt@Ag. Even though growth of a non-magnetic shell onto magnetic core NPs has been demonstrated to modify surface property as well as integrate additional functionality [129, 130, 134], systematic shell-layer control with unambiguous structural characterization at the single monolayer level should be crucial for unrevealing fundamental magnetism and thus finely tuning nanoscale magnetization [135], but has been lacking.

Existence of Ag shell in our FePt@Ag is evident by dramatic size increase as compared with that of plain core FePt NPs (Figure 3.5a), and can be further identified by high resolution TEM images with various shell thickness (Figure 3.5d), which shows accurate control and tunability at the single monolayer level as achieved in Figure 3.2a. Because of small size (as compared with bulk domain dimension) FePt core NPs typically manifest superparamagnetic behavior with blocking temperature (T_B) of 13K as former reports [79]. After the growth of Ag shell, FePt@Ag remains superparamagnetism but with smaller T_B (Figure 3.5b). Furthermore, as compared with featureless optical absorption from FePt core NPs, existence of metallic Ag shell

adds new optical functionality with pronounced SPR peak at 420 nm (Figure 3.5c). It has been proposed that magneto-optical effect can be remarkably enhanced near the SPR resonance, future study of our tunable FePt@Ag structure might offer unique magneto-optical devices similarly observed in metallic multilayers of nanometer scale thickness [136]. Furthermore, by introducing different shell composition, such as catalytic shell (for example, FePt@Pd in Figure 3.6), magnetic core@shell nanostructures enabled by our *i*PAPER approach should find immediate use for many applications including catalysis, fuel cell, bioimaging and etc.

While many works have been carried out over last few years on the understanding of magnetism of magnetic NPs, fundamental issues, such as origin of T_B, surface effect and interfacial proximity effect remain open questions, and some experimental observations were controversial due to inherent complexity and ill-control of structure. Importantly, availability of precise shell layer control should allow us to investigate magnetic property at the molecular level, as shown in Figure 3.5d. Magnetic property measurements of FePt@Ag with different shell thickness show that the T_B decrease dramatically right after the first monolayer growth, thereafter the T_B maintains a stable value. Mechanism of T_B of magnetic NPs has been argued over long period. Two main mechanisms have been proposed: one is due to collective inter-particle coupling [137, 138] and the other is related to anisotropy of nanostructures [139]. Our observation of strong dependence of one single non-magnetic shell layer is different from theoretical simulation on inter-particle distance [140], suggesting that collective coupling might not be the major contribution to

observed decrease of T_B. On the other hand, existence of Ag layer might induce relaxation of surface Fe and Pt atoms to reduce anisotropy and thus reduce T_B. Furthermore, low temperature hysteresis loop measurement of FePt NPs with different Ag layer thickness show continual increase of remnant field (M_r) with shell layer thickness. While it will require more experimental work in order to gain thorough understanding of this observation (for example, systematic study of different core size and shell composition), one possible explanation of observed enhancement of magnetization with the increase of shell thickness might be related to the stretching of inter-atomic distance inside magnetic core NPs due to shell-core interaction, which has been predicted to increase magnetic moments per atom [141]. If this mechanism is confirmed it might open up opportunity to manipulate nanoscale magnetism by choosing different shell materials to either stretch or contract inter-atomic bonds of magnetic NPs, which can be readily realized by our *i*PAPER technique.

3.3 Semiconductor-Core@Metallic-Shell

While precise control of bimetallic and magnetic-metallic core@shell nanostructures has shown exciting tunability and complex functionality, the uniqueness so far is mainly due to classic dielectric confinement.

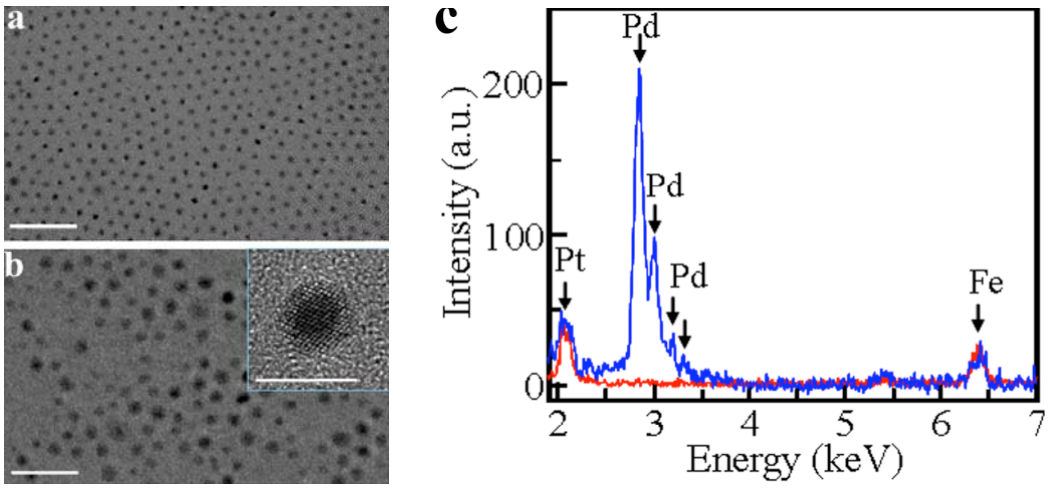

Figure 3.6 Synthesis and characterization of FePt@Pd by *i*PAPER strategy. a, Large scale TEM image of 2.0 ± 0.1 nm FePt NPs. Scale bar, 20nm. b, Large scale TEM image of 3.7 ± 0.4 nm FePt@Pd synthesized from FePt core NPs shown in a. Scale bar, 20nm. Inset, high resolution TEM image of single FePt@Pd, highlighting core and shell features. Scale bar, 5nm. c, Ensemble EDS measurements of plain FePt core NPs (red) and FePt@Pd (blue). Intensities of Pt peak at 2.06 keV are normalized to be the same in order to compare peaks contributed from Pd element.

Another important class of nanoscale core@shell heterostructures should be the integration of quantum confined semiconductor and metal, which might offer opportunity to investigate quantum and classic coupling interactions. The reverse structures (i.e., metal core and semiconductor shell such as Au@PbS [128]) have been reported, but there has been no success on the semiconductor core and metallic shell. However, from the view point of additional functionality of such as SPR contributed from noble metal component, it would be a better structural arrangement if metal is in the shell configuration. Figure 3.7a compares size evolution from plain semiconductor Ag_2Se core NPs to Ag_2Se@Ag nanostructure.

Ag_2Se NPs are prepared following a modified method [137], and used as core NPs without further processing. Ethanol is chosen as phase ***II*** reagent. In a typical synthesis of three monolayers of Ag shell with 4.8 nm Ag_2Se core, 0.8 mg of Ag_2Se NPs is dispersed in mixture solution of 6ml of H_2O, 4ml of ethanol, 0.4ml of oleic acid, and 0.3g of sodium oleate by sonification for 10mins. 1ml of $AgNO_3$ and 0.6ml of ascorbic acid are then added subsequently drop by drop. The reaction continues for 24hrs to achieve Ag_2Se@Ag structure. 10ml toluene is added to stop and extract final product of Ag_2Se@Ag.

As compared with Figures 3.2 and 3.5, the core@shell feature in Ag_2Se@Ag is not straightforward even from high resolution TEM images due to similar electron scattering cross section between Ag and Se atoms. In order to confirm core and shell features, we carry out single-particle energy dispersive X-ray spectroscopy (EDS) measurements in the center and the edge regions under the scanning TEM (STEM) mode (Figure 3.7b). A clear absence of Se component in the edge unambiguously supports the existence of core@shell structure. Importantly, Ag shell can also be precisely controlled, which is evident by the continuous increase of silver peak in the large scale EDS measurement (Figure 3.7c). In order to explore potential coupling effect we compare optical extinction spectra of Ag_2Se@Ag possessing different shell layers with those from separated plain Ag_2Se and Ag NPs (Figure 3.7d). There are a few unique features that can be immediately identified: (i) significantly enhanced optical extinction throughout a broad optical range which can be attributed to field enhancement by the shell contributed SPR [128]; (ii) peak features between 300 and

450nm can not be simply described as the linear combination between non-interacting Ag_2Se and Ag NPs that have been observed in the reverse structures [128, 134], which might suggest new coupling interactions unique in semiconductor-core and metal-shell configuration; and (iii) monotonic evolution of peaks with the increase of Ag shell layer thickness. More thorough understanding of coupling between semiconductor core and metallic shell as exhibited in the Figure Figure 3.7d is currently under investigation by time resolved experiments.

Also, different core and shell compositions for semiconductor-core@metallic-shell can be achieved by *i*PAPER, such as PbSe@Ag and PbSe@Pt are shown in Figure 3.8 and Figure 3.9.

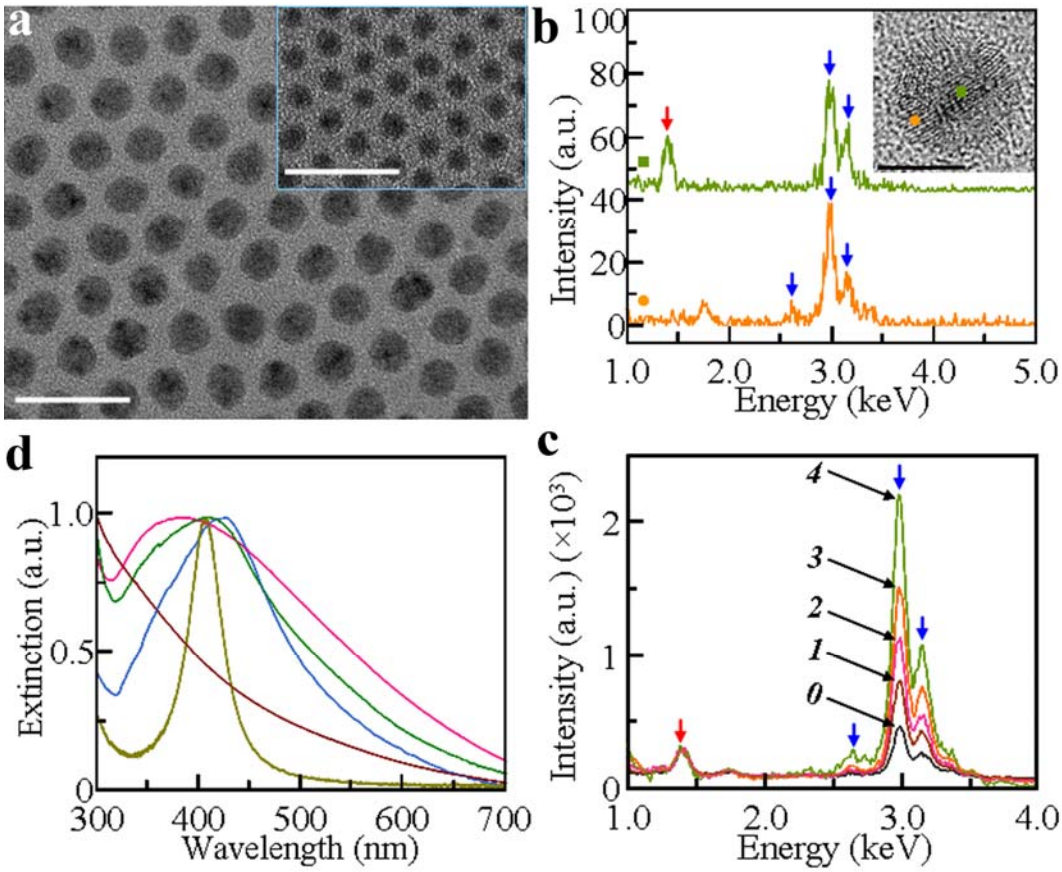

Figure 3.7 Precise and tunable control of Ag_2Se@Ag nanostructure. a, Large scale TEM image of Ag_2Se@Ag with three monolayers of Ag shell and core size of 4.8 ± 0.2 nm (Inset). Scale bar, 20nm. b, EDS spectra taken in the center (green) and the edge (orange) of a single Ag_2Se@Ag. Blue and red arrows highlight peaks contributed from Ag and Se components, respectively. A peak appeared in the orange EDS spectra at 1.75 keV is due to Si element contributed from commercial carbon thin films. Inset, high resolution TEM image of Ag_2Se@Ag indicating where the EDS spectra were taken. Scale bar, 5nm. c, Ensemble EDS spectra of Ag_2Se@Ag with different shell layer thickness. In order to compare intensity of Ag peaks (blue arrows), Se peaks (red arrow) are normalized to possess the same intensity for all shell thickness. d, Evolution of optical extinction features with Ag shell layer thickness: brown for plain Ag_2Se NPs; pink for one monolayer of Ag shell; green for two monolayers of Ag shell; blue for three monolayers of Ag shell; dark yellow for plain Ag NPs. In order to compare peak positions peak intensities are normalized to the unit.

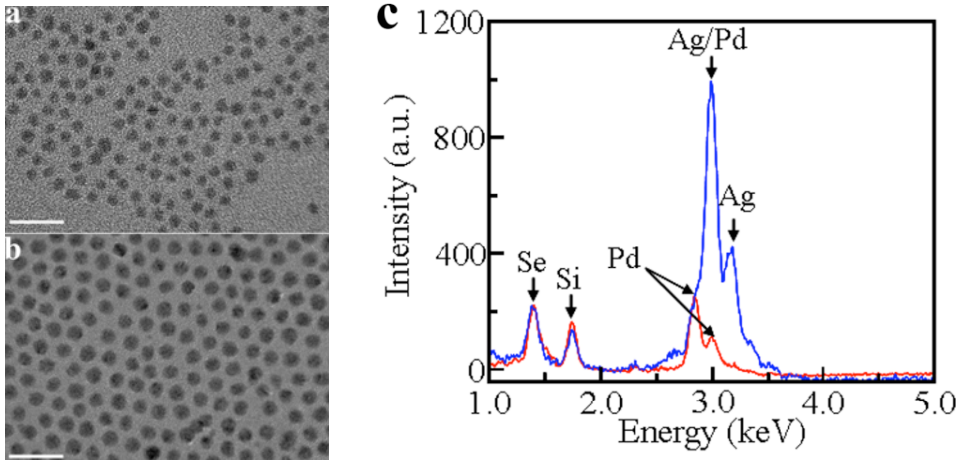

Figure 3.8 Synthesis and characterization of PdSe@Ag by *i*PAPER strategy. a, Large scale TEM image of 4.0 ± 0.2 nm PdSe NPs. Scale bar, 20nm. b, Large scale TEM image of 5.1 ± 0.3 nm PdSe@Ag synthesized from PdSe core NPs shown in a. Scale bar, 20nm. c, Ensemble EDS measurements of plain PdSe core NPs (red) and PdSe@Ag (blue). Intensities of Se peak at 1.39 keV are normalized to be the same in order to compare peaks contributed from Ag.

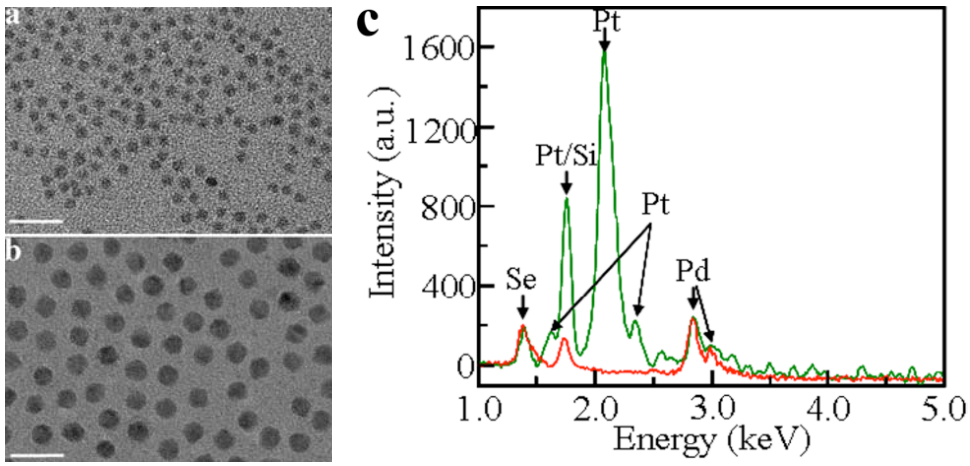

Figure 3.9 Synthesis and characterization of PdSe@Pt by *i*PAPER strategy. a, Large scale TEM image of 4.0 ± 0.2 nm PdSe NPs. Scale bar, 20nm. b, Large scale TEM image of 7.9 ± 0.5nm PdSe@Ag synthesized from PdSe core NPs shown in a. Scale bar, 20nm. c, Ensemble EDS measurements of plain PdSe core NPs (red) and PdSe@Ag (green). Intensities of Se peak at 1.39 keV are normalized to be the same in order to compare peaks contributed from Pt.

4. Conclusions

Our *i*PAPER approach represents a new strategy to achieve unprecedent control of core@metal-shell nanostructures with advantages including: (1) generality and flexibility for both core and shell components that can facilitate versatile applications of core@shell; (2) independent control of both core and shell growth that can increase the tunability of nanostructures; and (3) precise control of the metallic shell at the single monolayer level that makes it possible to tailor nanoscale property and functionality in a very accurate manner. The importance of such precise control has been highlighted by showing the single shell-layer dependence of optical, plasmonic and magnetic properties of as-prepared core@shell structures. Such control should be critical in the development of understanding many fundamental physics at the nanoscale as well as optimization of device applications.

Chapter 4: Pressure-Induced Spin Metastability in Semiconductor Quantum Dots [3]

Semiconductor quantum dots (QDs) have been applied as model systems to study various fundamental physics at the nanoscale, including solid-state phase transformation [142-144]. QDs also represent attractive building blocks for scalable solid-state implementations of quantum information processing by using spins of electrons and excitons as qubits [145]. While many recent advances have been achieved toward a thorough understanding of spin confined within QDs [146-148], crucial issues such as stability of spin states as well as manipulation of spin and spin-orbit coupling require more work, mainly due to the experimental challenges involved. The application of hydrostatic pressure represents an important means to modify key material parameters that could not be easily achieved by other methods, therefore offers a unique opportunity to explore various fundamental spin properties and interactions. In this chapter, I will describe the dependence of spin coherence dynamics on artificial lattice structures of semiconductor QDs by a new experimental method combining ultrafast optical orientation methods with diamond-anvil cell (DAC) techniques. Spin confined within QDs is observed to be robust up to several gigapascals, while electron and exciton Landé *g*-factors show a novel bi-stable characteristics prior to the first-order structural transition. This observation is attributed to the existence of a theoretically predicted metastable intermediate state at

3. This chapter was adapted from: Yun Tang, Alexander F. Goncharov, Viktor V. Struzhkin, Russell J. Hemley and Min Ouyang. "Pressure-induced Spin Metastability in Semiconductor Quantum Dots", *Nature Material*s, 2009, under review.

the nanoscale, for which there has been no previous experimental support. The results further reveal pressure enhanced fundamental exchange interactions for large-sized quantum dots with sizable anisotropy. Therefore, these findings shed insight into underlying mechanisms of long-debated nanoscale solid-state transformations in semiconductors [142-144], and are also important for understanding structure-spin correlations as well as engineering nanoscale structures to achieve desired spin property for the future development of spin based quantum devices.

1. Experimental Method

1.1 Two-color Time-resolved Faraday Rotation Experiments under High Hydrostatic Pressure

The experiment scheme of two-color time-resolved Faraday rotation (TRFR) is shown in Figure 4.1. QDs sample with DAC (Figure 4.2) is located in the center of a pair of permanent magnets with controllable separation. Magnetic field strength in sample position is calibrated with a Hall-effect Gaussmeter. A commercial Coherent optical parametric amplifer (OPA) with a 250-kHz repetition rate produces ~100femtosecond laser pulse with tunable wavelength ranging from 480nm to 720nm and is used as pump beam. A home-made OPA with similar laser output is synchronized with the first OPA, and applied as a probe beam, allowing pump-probe experiments at multiple wavelengths. In a typical experiment, the tunable circularly polarized output of the first OPA is adjusted to match with specific QDs energy state,

selectively generating spins oriented along the laser propagation direction. When the in-plane magnetic field is applied, the optically injected spins comprise a coherent superposition of states quantized along the field direction and separated in energy by the Zeeman splitting. As the system evolves with time, the energy difference between the spin states produces a quantum beating of spin magnetization along the optical path, which can be quantized by measuring the rotation of polarization plane of linearly polarized probe beam at different time delay Δt (the zero delay time is corrected for the chirp of OPA laser). To avoid Auger process and biexciton effects the number of excited electron-hole pairs is typically kept more than an order of magnitude lower than the number of QDs in the focus volume.

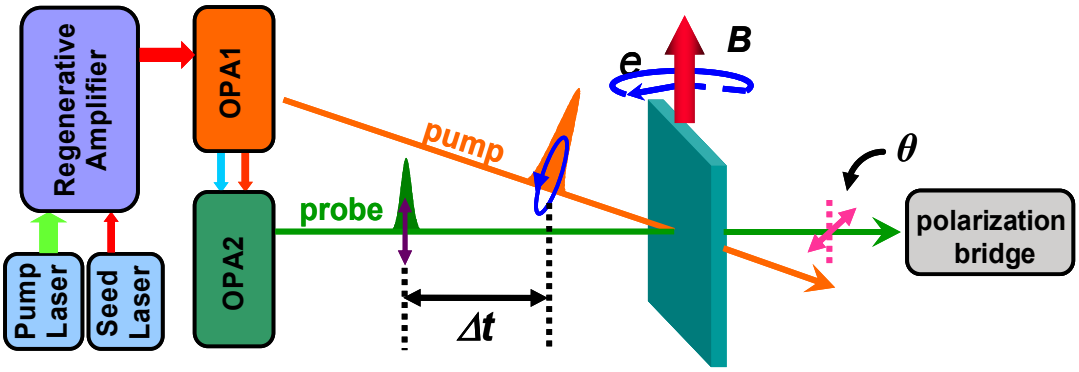

Figure 4.1 Two-color Time-Resolved Faraday Rotation (TRFR)

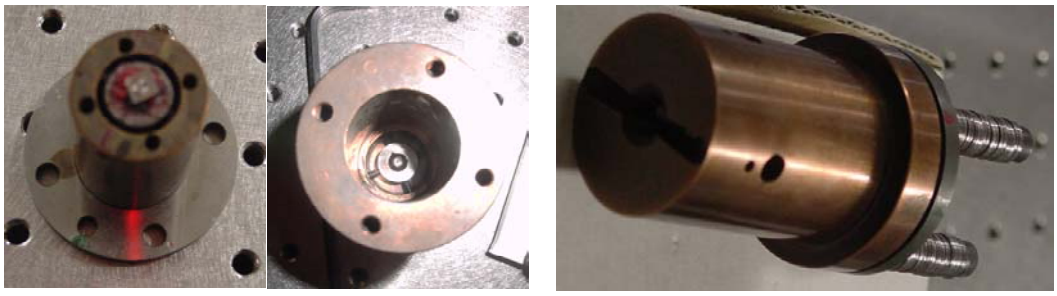

Figure 4.2 Photos of opened (left two) and closed (right) DAC cell.

1.2 Determination of *g*-factors

We determined the *g*-factors at different pressure based on the following routine: (1) The ν_L(s) of every single TRFR trace at a fixed magnetic were calculated by both fast Fourier FFT of and curve fitting to TRFR trace of spin precession; (2) Magnetic field *H* was varied and corresponding TRFR trace was recorded (typically more than six different magnetic fields were taken in order to calculate a *g*-factor). And for each magnetic field, the same procedure as described in (1) was taken to obtain corresponding ν_L(s); (3) The plot of ν_L(s) versus *H* could thus be obtained. The precise *g*-factor could thus be obtained by linear fitting.

1.3 High Pressure Effects

Sizeable birefringence effect of the two diamonds in the cell under load needed to be carefully compensated before reliable spin measurements could be obtained. In order to avoid hystersis effects associated with structural phase, in most of cases measurements of spin coherence dynamics were carried out after each pressure increased up to a value below the first-order phase transition pressure, and then on decompression. The compression and decompression data agreed well. In addition, usually data taken at the same pressure over various periods showed no difference, indicating that our observations were stable and not dependent on history.

2. Experiment and Discussion

CdSe QDs with diameters tunable from 2.5 to 7.0 nm were synthesized via a modified chemical method [21], possessing narrow size distribution of 4% and high crystallinity with the wurtzite structure under ambient conditions (Figure 4.3). These chemically synthesized QDs were originally capped/stabilized with a monolayer of surfactant, trioctylphosphine oxide, and were re-dissolved in 4-ethylpyridine as a pressure medium up to 10 GPa [143]. Pressure was determined by standard ruby fluorescence technique with a non-magnetic Be-Cu high pressure cell [149]. Our TRFR (Figure 4.1) technique was applied to measure spin coherence dynamics under pressure (Figure 4.3a) [145]. Briefly, a circularly polarized laser beam with tunable energy was used to excite spin polarization of CdSe QDs at a selected energy level. At a delay time Δt, a linearly polarized probe pulse with independent tunable photon energy measured the spin magnetization along the laser propagation direction by monitoring rotation of its linear polarization orientation (θ). When an in-plane magnetic field (H) was applied, spin processed about the field direction, which led to an oscillatory Faraday rotation at the sample dependent Larmor frequency (ν_L). This process can be described by $Ae^{-\frac{\Delta t}{T_2^*}}\cos(2\pi\nu_L\Delta t+\phi)$, where A is the amplitude, T_2^* is the transverse spin lifetime, and ϕ is the phase. A custom-made UV-visible spectrometer with fs-whitelight was used for linear optical absorption spectroscopy measurement.

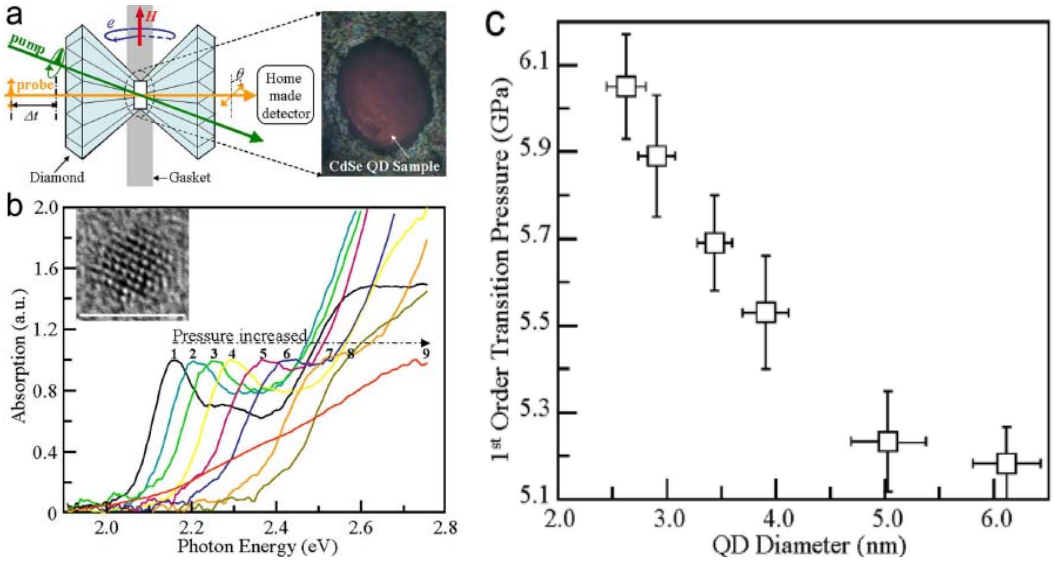

Figure 4.3 All optical spin resonance measurements of semiconductor QDs under pressure. a, Experimental setup. b, Linear optical absorption spectra of 3.4 nm CdSe QDs under selected hydrostatic pressure labeled by different number and color (1: 0.1 MPa; 2: 1.0 GPa; 3: 1.9 GPa; 4: 2.8 GPa; 5: 3.1 GPa; 6: 3.5 GPa; 7: 4.7 GPa; 8: 5.5 GPa; 9: 6.0 GPa). The inset shows a typical high-resolution transmission electron microscope image of CdSe QDs with wurtzite structure. Scale bar: 5nm. The QDs manifest spherical symmetry with the aspect ratio of 1. c, Size dependence of first order structural transition pressure obtained from b.

At low pressure linear absorption spectra of QD samples clearly exhibited discrete electronic states, which were in accord with previous calculations (Figure 4.3b) [150, 151]. When the pressure was slowly increased to a critical value absorption of CdSe QDs suddenly became featureless with the absorption changing continuously over a broad energy range. The origin of featureless optical absorption structure at high pressure was reported before and was attributed to a first-order solid-solid phase transition from wurtzite (with direct bandgap) to rock-salt structure (with indirect bandgap), first identified by X-ray diffraction measurements (XRD) [143].

This critical pressure could be used as a reference to characterize structural phase transition as a function of QD size (Figure 4.3c). Qualitatively, this size dependence agreed well with previous experimental hystersis measurements and thermodynamics considerations of the transformation [142, 143], and provided a cross-check on the experiments reported here.

Importantly, our TRFR measurements clearly revealed spin coherence dynamics of electrons and excitons confined within CdSe QDs under pressure (Figure 4.4a). Two Larmor precession frequencies could be distinguished from Fast Fourier transform (FFT) as well as beating pattern presented in raw TRFR data, which led to two different Landé *g*-factors based on the relation: $g = \frac{\mu_B H}{h \nu_L}$, where μ_B is Bohr magnet and h is Planck constant. Following the previous report under ambient condition [147] as well as our experimental result of size dependence of both *g*-factors (Figure 4.5), we can assign unambiguously observed two *g*-factors at low pressure to the electron (lower) and the exciton (higher), respectively.

We further characterized in detail both electron and exciton *g*-factors as a function of pressure (Figure 4.4b). Surprisingly, a novel bi-stable characteristic of the *g*-factors was clearly observed: Both electron and exciton *g*-factors remained stable over a certain pressure range above ambient conditions, and then increased with pressure and stabilized at different values up to the onset of the rock-salt phase. This observed *g*-factor transition was further found to show QD size dependence by assigning transition pressure to the midpoint of two bi-stable *g*-factors (Figure 4.4b

and Figure 4.6a). The monotonic increase in *g*-factor transition pressure with decreasing QD size suggests that this *g*-factor transition was a pressure-driven intrinsic effect of the QDs

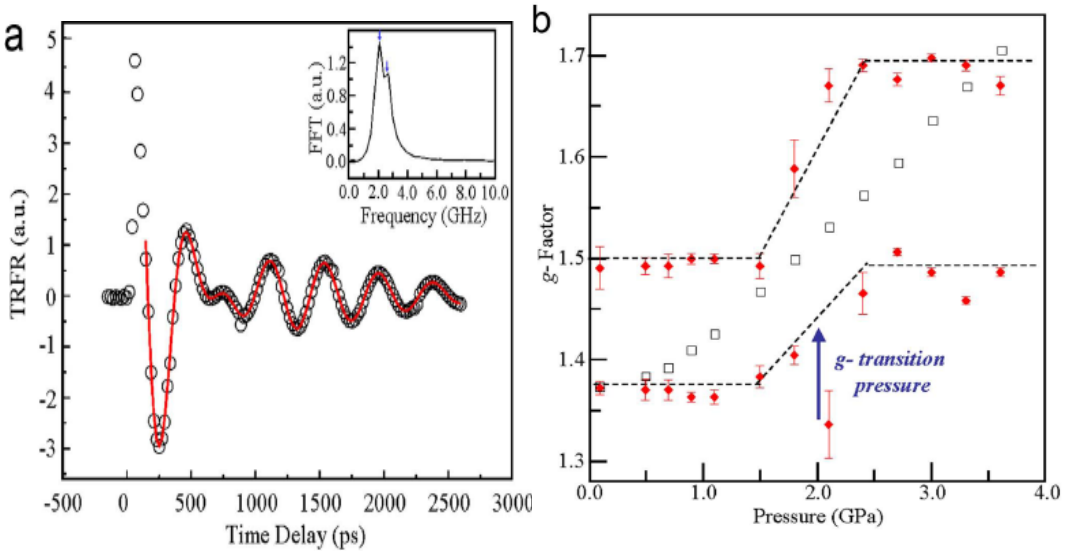

Figure 4.4 Spin coherence dynamics of 3.4 nm CdSe QDs under hydrostatic pressure. a, Typical TRFR data at 1.2 GPa. Circle: experimental data with H=0.21 T. Red solid curve: theoretical fit with two Larmor precession frequencies. The inset shows FFT of TRFR data revealing two distinct Larmor frequencies (1.98 GHz and 2.23 GHz). b, Dependence of electron (lower) and exciton (upper) *g*-factors on applied hydrostatic pressure, showing a novel *g*-factor transition before the first-order structural phase transition occurred. Dashed lines are guides to the eye for the evolution of experimental *g*-factors (red diamonds). Squares are theoretical calculations of pressure dependence of electron *g*-factor by assuming continual lattice deformation of ambient wurtzite phase. In the calculation, the pressure dependence of E_g and R were determined from linear optical absorption measurement. Pressure dependence of E_p and Δ_{SO} were obtained from theory prediction [165, 166]. The best fit of ambient *g*-factor was obtained with a=1.7 eV•nm^2, which were close to the accepted literature value [151].

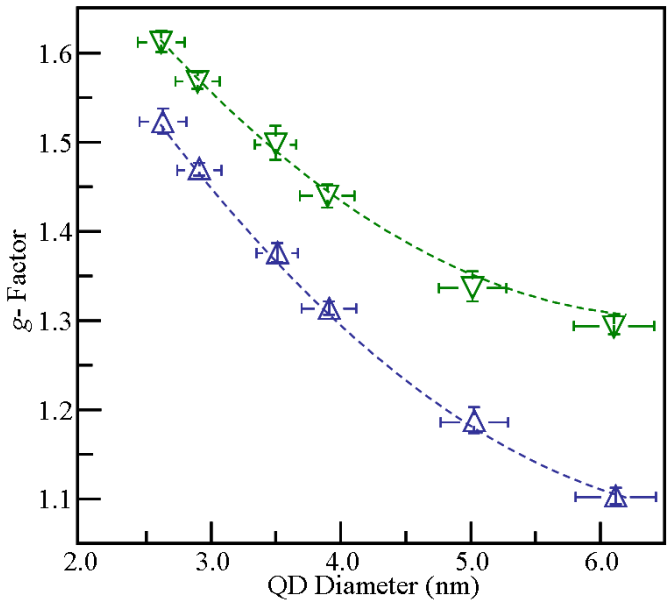

Figure 4.5 Size dependence of electron and exciton *g*-factors under ambient condition. Each *g*-factor was determined based on the procedure described in the Methods section. Two curve fittings were based on the assignment of electron (blue up triangles) and exciton (green down triangles) *g*-factors [173-175]

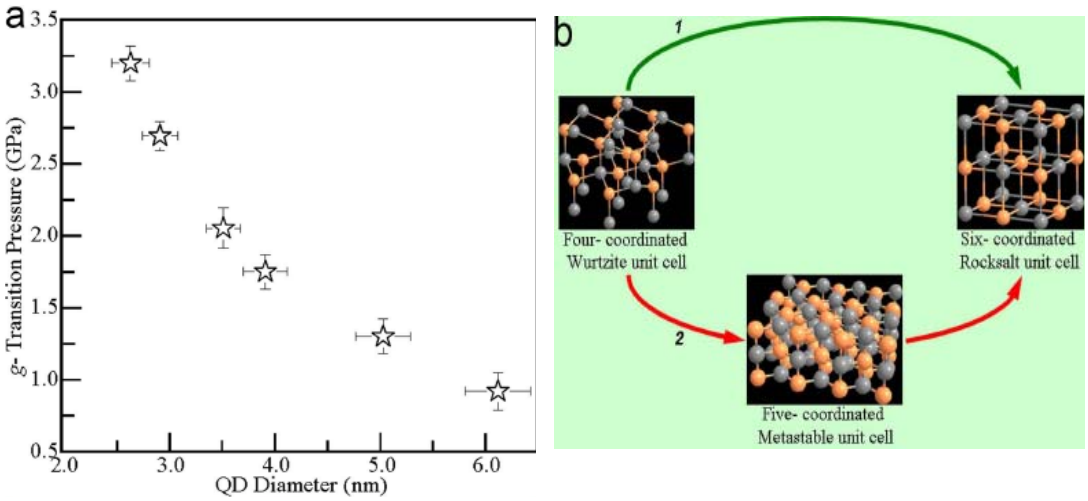

Figure 4.6 Landé *g*-factor transition at intermediate pressure. a, QD size dependence of *g*-factor transition pressure. b, Schematics of two different underlying transformation mechanisms of first-order phase transition. A five-coordinated structure (*P63mmc* space group) is used to represent metastable intermediate structure in path *2*.

As compared with the Figure 4.3c, the observed *g*-factor transition happened under a much smaller pressure; therefore it could not explicitly arise from the conventional first-order structural transition that has been confirmed by XRD measurements.

In order to gain insight of pressure-induced evolution of *g*-factors, the transformation path needs to be examined carefully. Due to the lack of effective experimental characterizations, the underlying mechanism of the first-order phase transition remains an unresolved issue. Furthermore, since the wurtzite/zinc-blende structure and rock-salt structure represent the most stable forms of most of the four- and six- coordinated binary compounds respectively, understanding the transition mechanism of CdSe QDs can be essential for manipulation of structural energetics of different semiconductor nanostructures to improve materials synthesis and to achieve desired materials functionality and property in a controlled manner. So far, two different mechanisms have been proposed (Figure 4.6b): the first is based on a continual deformation model, assuming high correlated atom motions during transformation [151-155]; the second is a two-step process, in which a long-lived metastable intermediate phase with a hypothetic five-coordinated structure exists before the first-order phase transition occurs [156-160]. Even though a metastable intermediate state was suggested based on shock wave compression experiments with bulk semiconductors [161-163], direct experimental evidence of such metastable states at the nanoscale has been lacking. Instead, earlier reports of high-pressure XRD measurements of CdSe QDs leaned to support continual deformation model because

of no detectable changes of XRD peaks before first-order transition [142-144]. As compared with experimental techniques based on structural characterization, our experiment provides unique opportunity to directly measure electronic and excitonic effective *g*-factors with a high degree of precision under pressure. This *g*-factor probe plays a central role in gaining fundamental understanding of electronic band structure as well as inter-band optical processes. Thus our measurements offer a valuable alternative insight (from the viewpoint of electronic structure) for underlying nanoscale solid-state transformation path.

From perturbation theory electron *g*-factor of spherical QD can be generalized in terms of fundamental band structure parameters, including size dependent bandgap E_g, the Kane matrix element E_p, and the spin-orbit splitting Δ_{SO} [147, 164-166]:

$$g_e(R) = g_0 - \frac{2}{3}\frac{E_p \Delta_{SO}}{\left(E_g + \frac{a}{R^2} + \Delta_{SO}\right)\left(E_g + \frac{a}{R^2}\right)}$$

where R is radius of the QDs and a is a fitting parameter in the simplest parabolic approximation . If the continual deformation model is correct a smooth increase of g_e factor is expected (Figure 4.4b), which is obviously in conflict with bi-stable *g*-factors characteristics observed during the high pressure transformation. Therefore, our observed bi-stable *g*-factor characteristics strongly suggest the existence of a long-lived metastable intermediate state during the transformation process, and the distinct *g*-factors correspond to different electronic states induced by pressure. In particular,

our measured *g*-factor transient pressure range is qualitatively consistent with the ~2 GPa pressure range of the onset of the theoretically predicted intermediate state [159].

While the *g*-factor transition was observed for all the QDs we investigated (as summarized in Figure 4.6a), there existed subtle differences between small- and large- sized CdSe QDs: For all large-sized QDs (≥ 5nm in diameter) we consistently observed three *g*-factors at higher pressure (Figure 4.7a and Figure 4.8), which suggested that this observation should be an intrinsic size related effect. In order to reveal such fine effect, we further investigated correlation between energy level scheme and *g*-factors by carrying out additional spectroscopic measurements. In general, optical study of the quantum size levels is very challenging because of inhomogeneous broadening and cannot be achieved simply by linear absorption measurements (Figure 4.3b). In contrast, TRFR has been demonstrated to be not only a unique and sensitive experimental probe for spin coherence dynamics but also a precise spectroscopic technique for directly identifying individual exciton transitions that reveal the fine electronic energy level scheme (Figure 4.7) [167-130]. For example, related TRFR spectroscopic study of colloidal CdS@CdSe quantum dot-quantum well system has revealed its fine energy levels, which showed consistency with ***k•p*** perturbation calculations [167]. Similarly, we carried out measurement of dependence of TRFR oscillation amplitude on probe energy under different pressure. In these experiments, a wavelength tunable probe with ~5 meV energy resolution was achieved by passing the light through a monochromator after transmission through the DAC. Under ambient conditions, TRFR spectra exhibited pronounced resonances

close to the absorption edges that could not be seen in linear absorption spectra and could be further assigned to fine energy level transition evaluated with ***k•p*** calculations (Figure 4.7c) [167]. While all the resonance peaks appeared under ambient conditions remained as the pressure was increased, two more new resonance peaks could be immediately identified with small amplitude and became more pronounced at higher pressure, which agreed well with the increased number of *g*-factors within the same pressure range. In contrast, we carried out same measurements for small-sized QDs and such control experiment showed no new resonance peaks during the entire transformation path.

Therefore, we attributed our observed increased number of *g*-factors to the pressure-enhanced fundamental exchange interactions in large-sized QDs [170], based on following facts: (i) For chemically synthesized QDs it has been shown that while smaller size QDs possessed very symmetrical spherical shape larger size QDs started manifesting anisotropy [21]. This can also be clearly seen by comparing high resolution TEM images in the Figure 4.3b, 4.7b and Figure 4.8, which shows the increase of aspect ratio of QDs with the size.

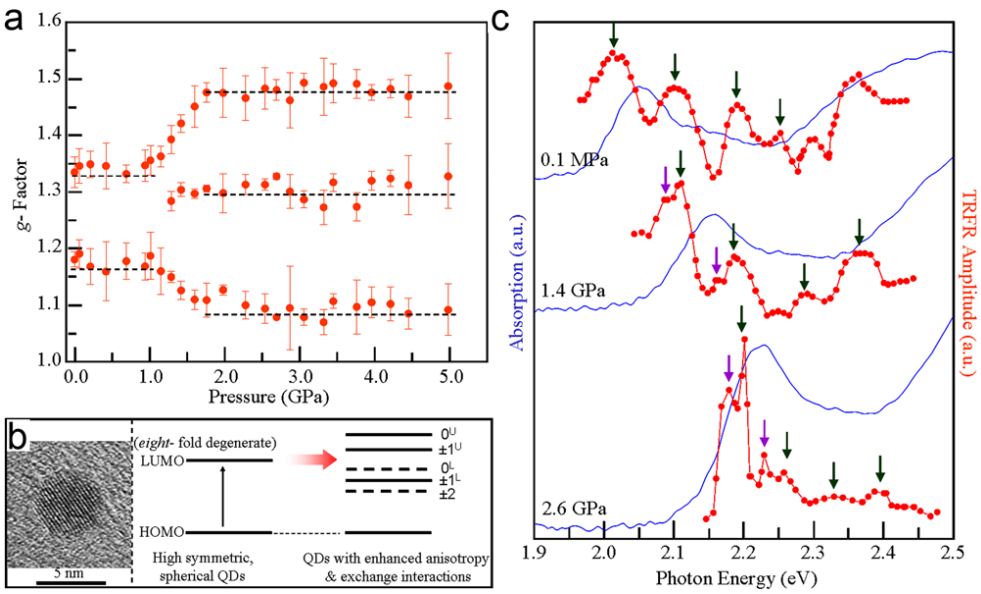

Figure 4.7 Pressure-enhanced exchange interactions in 5.1 nm CdSe QDs. a, Evolution of *g*-factors with applied pressure. b, (Left) Typical high-resolution transmission electron microscope image of a 5.1nm CdSe QDs. Scale bar: 5nm. The QDs manifest structural anisotropy with the aspect ratio of 1.04; (Right) Schematic of degeneracy lifting of the exciton fine band-edge structure (represented by HOMO-LUMO type energy levels) due to enhanced exchange interactions under pressure. Dashed lines are guides to the eye for the evolution of experimental *g*-factors. c, Dependence of TRFR amplitude on probe photon energy under three different pressures. Data were taken at fixed time delay Δt=300ps and normalized by the probe beam power. Green arrows highlight resonance peaks existing in all pressures, and red arrows highlight the appearance of new resonance peaks at higher pressure. For comparison, linear optical absorption spectra for different pressure were also present.

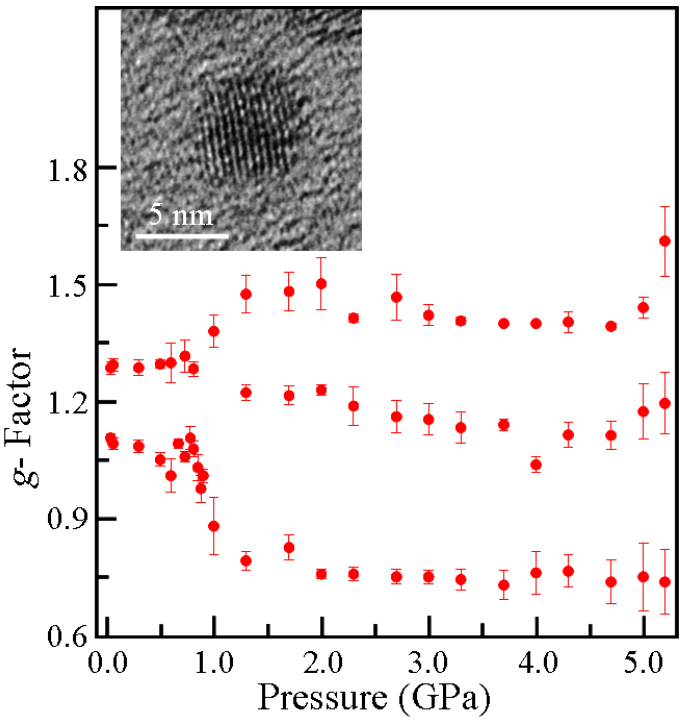

Figure 4.8 Evolution of electron and exciton *g*-factors with applied pressure in 6.2nm CdSe QDs. The inset shows corresponding high resolution transmission electron microscope image of QDs with aspect ratio of 1.07.

Under hydrostatic pressure, the aspect ratio can be significantly enhanced due to different compression ratio along different crystal axis; (ii) The evolution of initially eightfold degenerate ground state in a wurtzite spherical QD could be obtained from theoretical analysis of fine band-edge exciton structure when electron-hole exchange interactions, crystal field and anisotropy effects were considered (Figure 4.7b) [147, 171]. As a result, crystal field splitting and electron-hole exchange interactions would be significantly augmented in the more anisotropic QDs due to stronger confinement [150], thus leading to energy level degeneracy lifting and the *g*-

factors splitting; and (iii) The correlation between energy level splitting and the increased number of g-factors of large sized quantum dots at high pressure was indeed clearly observed in the Figure 4.7c.

3. Conclusions

In summary, investigations of quantum confined spin coherence dynamics of semiconductor QDs under pressure reveal that the spin of semiconductor QDs are very robust up to ~2 GPa. This observation is important for understanding the stability of spin qubits of QDs in the future quantum information processing devices. In contrast to former studies of nanoscale solid-state transformation by XRD and linear optical absorption, our new TRFR-DAC technique provides a unique insight into the transformation process from the viewpoint of electronic state property changes. A surprising pressure-driven *g*- factor transition was observed along the transformation path that could be attributed to the theoretically predicted metastable intermediate state not been explicitly observed yet at the nanoscale. This finding marks an important step towards deep understanding of underlying mechanism of related long debated nanoscale solid-state transformation. Furthermore, the current study reveals pressure enhanced fundamental fine exchange interactions that should provide deepened understanding necessary for future manipulation of spin states by such as interfacial/surface strain layer fabrication [120, 172].

Chapter 5: Summary and Future Outlook

Zero-dimensional Nanoparticles (NPs) are fascinating nanoscale material system because of their small size and large surface to volume ratio. The component, size, shape and structure of NPs are essential to their properties and applications. Our ability of precise and tunable structural control of metal, core@shell and semiconductor NPs provides invaluable opportunity to investigate fundamental nanoscience and to explore their exciting application of novel nanotechnology.

Through our novel strategy of nanoscale crystallinity engineering by chemical functional groups, I showed in the Chapter 2 that the twinning-defect-mediated chemical transformation enabled a rational design of complex nanostructures if nanoscale structural disorder was sensibly introduced to suppress or enhance competing mechanisms. Consequently, this nanocrystallinity engineering would provide a means for precisely tailoring nanoscale electronic and mechanical properties as well as controlling classical and quantum coupling interactions. Significant enhancement of electron–phonon interaction by twinning defects can eventually lead to sizeable modulation of electronic and heat conductivity and/or superconductivity of metals at the nanoscale [176], ultimately leading to the optimization of device performance of crystallinity-engineered NPs.

More generally, more than one functional group R can be simultaneously incorporated into metal phosphine precursors [177], which should enable finer kinetic

control of chemical environment in metal NPs synthesis and further distinguish different multiply twinned species. As discussed in the Chapter 2, the existence of ill-characterized twinning structures is a common feature for most of noble metal NPs. While we focus on silver NPs in the Chapter 2, our method can be readily expanded to other metal nanostructures, including Au and Pt, with the precise control of nanometer scale crystallinity. This would represent a significant advance in the complexity as well as functionality of the building blocks of nanoscience and nanotechnology.

From our progress on the nanocrystallintiy control of silver NPs we have provided three examples to highlight its importance. Another important application of metal NPs (particularly silver NPs discussed in this thesis) is the surface Raman enhancement for bio-imaging and sensing. Recently, Zhuang's group at Harvard University reported the observation of 2-5 orders of magnitude enhancement of Raman activity from polycrystalline silver NPs with grain size down to the electron Fermi wavelength (~1 nm) [178]. Similar measurements comparing Raman activity between identical sized multiply twinned and single-crystalline silver NPs should provide insight into the mechanism of nanoscale Raman activity and provide an optimized optical probe for bio-imaging [179].

In the Chapter 3, I described a very general synthetic strategy, denoted as intermediate phase assisted phase exchange and reaction, to achieve unprecedented control of versatile core@metal shell nanostructures in a very accurate manner.

Because core and shell sizes can be independently controlled, our approach provides aunique way to tune the versatile core@shell nanostructures with tailored property and functionality. We observed for the first time the evolution of surface plasmon resonance of Au@Ag with independent controlled core size and shell thickness at single monolayer level; We identified significantly enhanced optical extinction which can be attributed to field enhancement by the metal shell contributed SPR and the new coupling interactions between semiconductor core and metal shell; We noticed the strong dependence of blocking temperature decrease of magnetic core on one single non-magnetic shell layer and continual increase of remnant field with shell layer thickness, which suggested magnetic core with tunable non-magnetic shell is a potential model for nanoscale magnetism understanding.

It is obvious that more meticulous characterizations of core@shell are needed to investigate nanoscale optics, plasmonics and magnetism in an accurate manner, for examples, time-resolved experiment on fundamental couplings between shell and, systematic SQUID study of different size of magnetic core and non-magnetic or magnetic shell composition. Additional importantly, because metallic shell can be converted to related compounds [7] (Figure 5.1), our *i*PAPER approach also offers a general and constructive method to create wide range of core@shell structures with desired multi-functionality, and thus provide versatile nanoscale building blocks from the bottom-up approach.

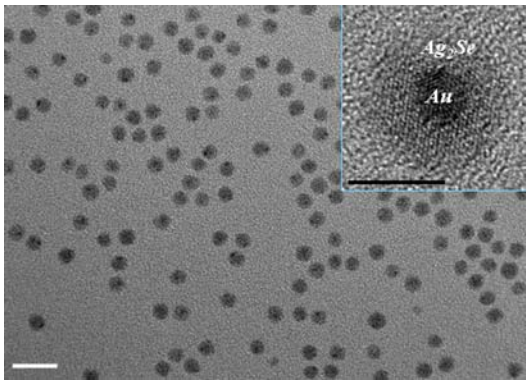

Figure 5.1 Au@Ag_2Se converted from Au@Ag with 2.8 nm Au core and six monolayers of Ag shell. Large scale TEM image of 6.8 ± 0.3 nm Au@Ag2Se. Scale bar, 20nm. Inset, high resolution TEM image of Au@Ag2Se showing clear core and shell structures. Scale bar, 5nm.

Enabled by our unique technique combining of two-color time-resolved Faraday rotation method with diamond-anvil cell technique, consistent examination of pressure induced spin metastable states of semiconductor NPs were discussed in the Chapter 4. A surprising bi-stable characteristic of the Landé g-factors of both electron and exciton was clearly observed, which provided the first experimental supporting for the existence of a theoretically predicted metastable intermediate state before the occurrence of first-order phase transition of semiconductor NPs. This observation marks an important step towards future utilization of quantum information processing based on spin qubits of semiconductor NPs. Looking into the future, a few directions regarding nanoscale structural transformation can be immediately addressed following our progress presented in the Chapter 4, including: *g*-factor behaviors of other II-V or III-V semiconductor NPs with anisotropic morphologies, electron or spin transportation of semiconductor NPs assembles, fundamental electron-electron and electron-phonon couplings in crystallinity engineered metal NPs, and etc.

References

1. Taniguchi, Norio. On the Basic Concept of "Nano-Technology". *Proc. Intl. Conf. Prod. Eng.,* Tokyo, Part II, Japan Society of Precision Engineering (1974), 18-23.

2. Feynman, Richard. There's plenty of room at the bottom: An invitation to enter a new field of physics. *Caltech's Engineering and Science* (1960), 23(5), 22-39.

3. Binnig, G.; Rohrer, H. Scanning tunneling microscopy. *IBM Journal of Research and Development* (1986), 30(4), 355-69.

4. Kroto, H. W.; Heath, J. R.; O'Brien, S. C.; Curl, R. F.; Smalley, R. E. C60: buckminsterfullerene. *Nature* (1985), 318(6042), 162-163.

5. Iijima, Sumio. Helical microtubules of graphitic carbon. *Nature* (1991), 354(6348), 56-58.

6. Rossetti, R.; Nakahara, S.; Brus, L. E. Quantum size effects in the redox potentials, resonance Raman spectra, and electronic spectra of cadmium sulfide crystallites in aqueous solution. *Journal of Chemical Physics* (1983), 79(2), 1086-1088.

7. Tang, Yun; Ouyang, Min. Tailoring properties and functionalities of metal nanoparticles through crystallinity engineering. *Nature Materials* (2007), 6(10), 754-759.

8. Bawendi, M. G. http://nanocluster.mit.edu/.

9. Klimov, Victor I. Semiconductor and Metal nanocrystals: Synthesis and Electronic and Optical Properties. Marcel Dekker: New York, 2004.

10. Brus, L. E. Electron-electron and electron-hole interactions in small semiconductor crystallites: the size dependence of the lowest excited electronic state. *Journal of Chemical Physics* (1984), 80(9), 4403-4409.

11. Bastard, G. Wave Mechanics Applied to Semiconductor Heterostructures. Wiley: New York, 1991.

12. Efros, A. L.; Efros, A. L. Interband light absorption in a semiconductor sphere. *Fizika i Tekhnika Poluprovodnikov* (1982), 16(7), 1209-1214.

13. Brus, L. E. A simple model for the ionization potential, electron affinity, and aqueous redox potentials of small semiconductor crystallites. *Journal of Chemical Physics* (1983), 79(11), 5566-5571.

14. Xia, Jian-Bai. Electronic structures of zero-dimensional quantum wells. *Physical Review B* (1989), 40(12), 8500-8507.

15. Kittel, C. Quantum Theory of Solids. Wiley: New York, 1987.

16. Efros, Al. L.; Rosen, M. Quantum size level structure of narrow-gap semiconductor nanocrystals: Effect of band coupling. *Physical Review B* (1998), 58(11), 7120-7135.

17. Alivisatos, A. P.; Harris, A. L.; Levinos, N. J.; Steigerwald, M. L.; Brus, L. E. Electronic states of semiconductor clusters: homogeneous and inhomogeneous broadening of the optical spectrum. *Journal of Chemical Physics* (1988), 89(7), 4001-4011.

18. Bawendi, M. G.; Wilson, W. L.; Rothberg, L.; Carroll, P. J.; Jedju, T. M.; Steigerwald, M. L.; Brus, L. E. Electronic structure and photoexcited-carrier dynamics in nanometer-size cadmium selenide clusters. *Physical Review Letters* (1990), 65(13), 1623-1626.

19. Guzelian, A. A.; Katari, J. E. B.; Kadavanich, A. V.; Banin, U.; Hamad, K.; Juban, E.; Alivisatos, A. P.; Wolters, R. H.; Arnold, C. C.; Heath, J. R. Synthesis of Size-Selected, Surface-Passivated InP Nanocrystals. *Journal of Physical Chemistry* (1996), 100(17), 7212-7219.

20. Lomascolo, M.; Vergine, A.; Johal, T. K.; Rinaldi, R.; Passaseo, A.; Cingolani, R.; Patane, S.; Labardi, M.; Allegrini, M.; Troiani, F.; Molinari, E. Dominance of charged excitons in single-quantum-dot photoluminescence spectra. *Physical Review B* (2002), 66(4), 041302/1-041302/4.

21. Murray, C. B.; Norris, D. J.; Bawendi, M. G. Synthesis and characterization of nearly monodisperse CdE (E = sulfur, selenium, tellurium) semiconductor nanocrystallites. *Journal of the American Chemical Society* (1993), 115(19), 8706-8715.

22. Qu, Lianhua; Peng, Xiaogang. Control of Photoluminescence Properties of CdSe Nanocrystals in Growth. *Journal of the American Chemical Society* (2002), 124(9), 2049-2055.

23. Hines, Margaret A.; Guyot-Sionnest, Philippe. Bright UV-Blue Luminescent Colloidal ZnSe Nanocrystals. *Journal of Physical Chemistry B* (1998), 102(19), 3655-3657.

24. Murray, C. B.; Sun, Shouheng; Gaschler, W.; Doyle, H.; Betley, T. A.; Kagan, C. R. Colloidal synthesis of nanocrystals and nanocrystal superlattices. *IBM Journal of Research and Development* (2001), 45(1), 47-56.

25. Wehrenberg, Brian L.; Wang, Congjun; Guyot-Sionnest, Philippe. Interband and Intraband Optical Studies of PbSe Colloidal Quantum Dots. *Journal of Physical Chemistry B* (2002), 106(41), 10634-10640.

26. Micic, O. I.; Sprague, J. R.; Curtis, C. J.; Jones, K. M.; Machol, J. L.; Nozik, A. J.; Giessen, H.; Fluegel, B.; Mohs, G.; Peyghambarian, N. Synthesis and Characterization of InP, GaP, and GaInP2 Quantum Dots. *Journal of Physical Chemistry* (1995), 99(19), 7754-7759.

27. Wilson, William L.; Szajowski, P. F.; Brus, L. E. Quantum confinement in size-selected, surface-oxidized silicon nanocrystals. *Science* (1993), 262(5137), 1242-1244.

28. Peng, Xiaogang; Schlamp, Michael C.; Kadavanich, Andreas V.; Alivisatos, A. P. Epitaxial Growth of Highly Luminescent CdSe/CdS Core/Shell Nanocrystals with Photostability and Electronic Accessibility. *Journal of the American Chemical Society* (1997), 119(30), 7019-7029.

29. Dabbousi, B. O.; Rodriguez-Viejo, J.; Mikulec, F. V.; Heine, J. R.; Mattoussi, H.; Ober, R.; Jensen, K. F.; Bawendi, M. G. (CdSe)ZnS Core-Shell Quantum Dots: Synthesis and Optical and Structural Characterization of a Size Series of Highly Luminescent Materials. *Journal of Physical Chemistry B* (1997), 101(46), 9463-9475.

30. Reiss, Peter; Protiere, Myriam; Li, Liang. Core/shell semiconductor nanocrystals. *Small* (2009), 5(2), 154-168.

31. Yin, Yadong; Alivisatos, A. Paul. Colloidal nanocrystal synthesis and the organic-inorganic interface. *Nature* (2005), 437(7059), 664-670.

32. Kumar, Sandeep; Nann, Thomas. Shape control of II-VI semiconductor nanomaterials. *Small* (2006), 2(3), 316-329.

33. Norris, David J.; Efros, Alexander L.; Erwin, Steven C. Doped nanocrystals. *Science* (2008), 319(5871), 1776-1779.

34. San-Miguel, Alfonso. Nanomaterials under high-pressure. *Chemical Society Reviews* (2006), 35(10), 876-889.

35. Chen, Chia-Chun; Herhold, A. B.; Johnson, C. S.; Alivisatos, A. P. Size dependence of structural metastability in semiconductor nanocrystals. *Science* (1997), 276(5311), 398-401.

36. Biju, Vasudevanpillai; Itoh, Tamitake; Anas, Abdulaziz; Sujith, Athiyanathil; Ishikawa, Mitsuru. Semiconductor quantum dots and metal nanoparticles: syntheses, optical properties, and biological applications. *Analytical and*

Bioanalytical Chemistry (2008), 391(7), 2469-2495.

37. Kamat, Prashant V. Quantum Dot Solar Cells. Semiconductor Nanocrystals as Light Harvesters. *Journal of Physical Chemistry C* (2008), 112(48), 18737-18753.

38. Klimov, Victor I. Spectral and dynamical properties of multiexcitons in semiconductor nanocrystals. *Annual Review of Physical Chemistry* (2007), 58, 635-673.

39. Faraday, Michael. Experimental relations of gold (and other metals) to light. *Philosophical Transactions of the Royal Society of London* (1857), 147(1), 145-181.

40. Kelly, K. Lance; Coronado, Eduardo; Zhao, Lin Lin; Schatz, George C. The Optical Properties of Metal Nanoparticles: The Influence of Size, Shape, and Dielectric Environment. *Journal of Physical Chemistry B* (2003), 107(3), 668-677.

41. Mie, G. Contributions to the Optics of Turbid Media, Especially Colloidal Metal Solutions. *Annalen der Physik* (1908), 25, 377-445.

42. Bohren, Craig F.; Huffman, Donald R. Absorption and Scattering of Light by Small Particles. Wiley: New York, 1983.

43. Willets, Katherine A.; Van Duyne, Richard P. Localized surface plasmon resonance spectroscopy and sensing. *Annual Review of Physical Chemistry* (2007), 58, 267-297.

44. Nie, Shuming; Emory, Steven R. Probing single molecules and single nanoparticles by surface-enhanced Raman scattering. *Science* (1997), 275(5303), 1102-1106.

45. Campion, Alan; Kambhampati, Patanjali. Surface-enhanced Raman scattering. *Chemical Society Reviews* (1998), 27(4), 241-250.

46. Voisin, Christophe; Del Fatti, Natalia; Christofilos, Dimitris; Vallee, Fabrice. Ultrafast Electron Dynamics and Optical Nonlinearities in Metal Nanoparticles. *Journal of Physical Chemistry B* (2001), 105(12), 2264-2280.

47. Xue, Can; Mirkin, Chad A. pH-switchable silver nanoprism growth pathways. *Angewandte Chemie, International Edition* (2007), 46(12), 2036-2038.

48. Jain, Prashant K.; Huang, Xiaohua; El-Sayed, Ivan H.; El-Sayed, Mostafa A. Noble Metals on the Nanoscale: Optical and Photothermal Properties and Some Applications in Imaging, Sensing, Biology, and Medicine. *Accounts of Chemical*

Research (2008), 41(12), 1578-1586.

49. Tao, Andrea; Sinsermsuksakul, Prasert; Yang, Peidong. Tunable plasmonic lattices of silver nanocrystals. *Nature Nanotechnology* (2007), 2(7), 435-440.

50. Xia, Younan; Halas, Naomi J. Shape-controlled synthesis and surface plasmonic properties of metallic nanostructures. *MRS Bulletin* (2005), 30(5), 338-348.

51. Soennichsen, Carsten; Reinhard, Bjoern M.; Liphardt, Jan; Alivisatos, A. Paul. A molecular ruler based on plasmon coupling of single gold and silver nanoparticles. *Nature Biotechnology* (2005), 23(6), 741-745.

52. Maier, Stefan A.; Kik, Pieter G.; Atwater, Harry A.; Meltzer, Sheffer; Harel, Elad; Koel, Bruce E.; Requicha, Ari A. G. Local detection of electromagnetic energy transport below the diffraction limit in metal nanoparticle plasmon waveguides. *Nature Materials* (2003), 2(4), 229-232.

53. Jiles, D. C. Introduction to Magnetism and Magnetic Materials. CRC Press: Boca Raton, 1998.

54. Jun, Young-wook; Seo, Jung-wook; Cheon, Jinwoo. Nanoscaling Laws of Magnetic Nanoparticles and Their Applicabilities in Biomedical Sciences. *Accounts of Chemical Research* (2008), 41(2), 179-189.

55. Frey, Natalie A.; Peng, Sheng; Cheng, Kai; Sun Shouheng. Magnetic nanoparticles: synthesis, functionalization, and applications in bioimaging and magnetic energy storage. *Chemical Society Reviews* (2009), ASAP.

56. Park, Jongnam; Joo, Jin; Kwon, Soon Gu; Jang, Youngjin; Hyeon, Taeghwan. Synthesis of monodisperse spherical nanocrystals. *Angewandte Chemie, International Edition* (2007), 46(25), 4630-4660.

57. Peng, Sheng; Wang, Chao; Xie, Jin; Sun, Shouheng. Synthesis and Stabilization of Monodisperse Fe Nanoparticles. *Journal of the American Chemical Society* (2006), 128(33), 10676-10677.

58. Kwon, Soon Gu; Hyeon, Taeghwan. Colloidal Chemical Synthesis and Formation Kinetics of Uniformly Sized Nanocrystals of Metals, Oxides, and Chalcogenides. *Accounts of Chemical Research* (2008), 41(12), 1696-1709.

59. Chen, Yongfen; Johnson, Eric; Peng, Xiaogang. Formation of monodisperse and shape-controlled MnO nanocrystals in non-injection synthesis: self-focusing via ripening. *Journal of the American Chemical Society* (2007), 129(35), 10937-10947.

60. Park, Jongnam; Koo, Bonil; Hwang, Yosun; Bae, Chejin; An, Kwangjin; Park,

Je-Geun; Park, Hyun Min; Hyeon, Taeghwan. Novel synthesis of magnetic Fe2P nanorods from thermal decomposition of continuously delivered precursors using a syringe pump. *Angewandte Chemie, International Edition* (2004), 43(17), 2282-2285.

61. Respaud, M.; Broto, J. M.; Rakoto, H.; Fert, A. R.; Thomas, L.; Barbara, B.; Verelst, M.; Snoeck, E.; Lecante, P.; Mosset, A.; Osuna, J.; Ely, Ould; Amiens, C.; Chaudret, B. Surface effects on the magnetic properties of ultrafine cobalt particles. *Physical Review B* (1998), 57(5), 2925-2935.

62. Kodama, R. H. Magnetic nanoparticles. *Journal of Magnetism and Magnetic Materials* (1999), 200(1-3), 359-372.

63. Lu, An-Hui; Salabas, E. L.; Schuth, Ferdi. Magnetic nanoparticles: synthesis, protection, functionalization, and application. *Angewandte Chemie, International Edition* (2007), 46(8), 1222-1244.

64. Bader, S. D. Colloquium: opportunities in nanomagnetism. *Reviews of Modern Physics* (2006), 78(1), 1-15.

65. Collier, C. P.; Saykally, R. J.; Shiang, J. J.; Henrichs, S. E.; Heath, J. R. Reversible tuning of silver quantum dot monolayers through the metal-insulator transition. *Science* (1997), 277(5334), 1978-1981.

66. Valden, M.; Lai, X.; Goodman, D. W. Onset of catalytic activity of gold clusters on titania with the appearance of nonmetallic properties. *Science* (1998), 281(5383), 1647-1650.

67. Cao, YunWei Charles; Jin, Rongchao; Mirkin, Chad A. Nanoparticles with Raman spectroscopic fingerprints for DNA and RNA detection. *Science* (2002), 297(5586), 1536-1540.

68. Sherry, Leif J.; Jin, Rongchao; Mirkin, Chad A.; Schatz, George C.; Van Duyne, Richard P. Localized Surface Plasmon Resonance Spectroscopy of Single Silver Triangular Nanoprisms. *Nano Letters* (2006), 6(9), 2060-2065.

69. Sherry, Leif J.; Chang, Shih-Hui; Schatz, George C.; Van Duyne, Richard P.; Wiley, Benjamin J.; Xia, Younan. Localized surface plasmon resonance spectroscopy of single silver Nanocubes. *Nano Letters* (2005), 5(10), 2034-2038.

70. Zheng, Nanfeng; Fan, Jie; Stucky, Galen D. One-Step One-Phase Synthesis of Monodisperse Noble-Metallic Nanoparticles and Their Colloidal Crystals. *Journal of the American Chemical Society* (2006), 128(20), 6550-6551.

71. Jin, Rongchao; Cao, Y. Charles; Hao, Encai; Metraux, Gabriella S.; Schatz, George C.; Mirkin, Chad A. Controlling anisotropic nanoparticle growth through

plasmon excitation. *Nature* (2003), 425(6957), 487-490.

72. Wang, Chao; Daimon, Hideo; Onodera, Taigo; Koda, Tetsunori; Sun, Shouheng. A general approach to the size- and shape-controlled synthesis of platinum nanoparticles and their catalytic reduction of oxygen. *Angewandte Chemie, International Edition* (2008), 47(19), 3588-3591.

73. Sun, Jialin; Zhang, Jianhong; Liu, Wei; Liu, Sheng; Sun, Hongsan; Jiang, Kaili; Li, Qunqing; Guo, Jihua. Shape-controlled synthesis of silver nanostructures. *Nanotechnology* (2005), 16(10), 2412-2414.

74. Wiley, Benjamin; Sun, Yugang; Chen, Jingyi; Cang, Hu; Li, Zhi-Yuan; Li, Xingde; Xia, Younan. Shape-controlled synthesis of silver and gold nanostructures. *MRS Bulletin* (2005), 30(5), 356-361.

75. Wiley, Benjamin; Sun, Yugang; Mayers, Brian; Xia, Younan. Shape-controlled synthesis of metal nanostructures: The case of silver. *Chemistry—A European Journal* (2005), 11(2), 454-463.

76. Zeng, Hao; Rice, Philip M.; Wang, Shan X.; Sun, Shouheng. Shape-Controlled Synthesis and Shape-Induced Texture of MnFe2O4 Nanoparticles. *Journal of the American Chemical Society* (2004), 126(37), 11458-11459.

77. Sun, Yugang; Xia, Younan. Shape-Controlled Synthesis of Gold and Silver Nanoparticles. Science (2002), 298(5601), 2176-2179.

78. Murray, C. B.; Kagan, C. R.; Bawendi, M. G. Synthesis and characterization of monodisperse nanocrystals and close-packed nanocrystal assemblies. *Annual Review of Materials Science* (2000), 30, 545-610.

79. Sun, Shouheng; Murray, C. B.; Weller, Dieter; Folks, Liesl; Moser, Andreas. Monodisperse FePt nanoparticles and ferromagnetic FePt nanocrystal superlattices. *Science* (2000), 287(5460), 1989-1992.

80. Baletto, Francesca; Ferrando, Riccardo. Structural properties of nanoclusters: Energetic, thermodynamic, and kinetic effects. *Reviews of Modern Physics* (2005), 77(1), 371-423.

81. Marks, L D. Experimental studies of small particle structures. *Reports on Progress in Physics* (1994), 57(6), 603-649.

82. Nalwa, Hari Singh. Encyclopedia of nanoscience and nanotechnology. American Scientific Publishers: Stevenson Ranch, 2004.

83. Wang, Z. L. Transmission electron microscopy of shape-controlled nanocrystals and their assemblies. *Journal of Physical Chemistry B* (2000), 104(6), 1153-

1175.

84. Wiley, Benjamin; Herricks, Thurston; Sun, Yugang; Xia, Younan. Polyol Synthesis of Silver Nanoparticles: Use of Chloride and Oxygen to Promote the Formation of Single-Crystal, Truncated Cubes and Tetrahedrons. *Nano Letters* (2004), 4(9), 1733-1739.

85. Liu, C. W.; Pan, Hongjun; Fackler, John P., Jr.; Wu, Gang; Wasylishen, Roderick E.; Shang, Maoyu. Studies of [Ag(PPh3)2]NO3, [Ag{P(CH2CH2CN)3}2]NO3 and [Ag{P(C6H4Me-m)3}2]NO3 by x-ray diffraction and solid-state nuclear magnetic resonance. *Journal of the Chemical Society, Dalton Transactions: Inorganic Chemistry* (1995), (22), 3691-3697.

86. Camalli, M.; Caruso, F. Correlation between phosphorus-31 NMR data and structural parameters on Ag(PPH3)3X series. Crystal and molecular structure of tris(triphenylphosphine)-silver(I) tetrafluoroborate and tris(triphenylphosphine)-silver(I) iodide. *Inorganica Chimica Acta* (1987), 127(2), 209-213.

87. Cassel, Anders. Structures of complexes between metals halides and phosphinothioethers or related ligands. IX. Chlorotris(triphenylphosphine)silver. *Acta Crystallographica B* (1981), B37(1), 229-231.

88. Sanghani, Daksha V.; Smith, Peter J.; Allen, David W.; Taylor, Brian F. A reinvestigation of some triphenylphosphine-silver halide complexes and their reaction with stannous chloride: tin-119m Moessbauer and phosphorus-31 FT NMR studies. *Inorganica Chimica Acta* (1982), 59(2), 203-206.

89. Son, Dong Hee; Hughes, Steven M.; Yin, Yadong; Alivisatos, A. Paul. Cation Exchange Reactions in Ionic Nanocrystals. *Science* (2004), 306(5698), 1009-1012.

90. Cabot, Andreu; Puntes, Victor F.; Shevchenko, Elena; Yin, Yadong; Balcells, Lluis; Marcus, Matthew A.; Hughes, Steven M.; Alivisatos, A. Paul. Vacancy Coalescence during Oxidation of Iron Nanoparticles. *Journal of the American Chemical Society* (2007), 129(34), 10358-10360.

91. Yin, Yadong; Erdonmez, Can K.; Cabot, Andreu; Hughes, Steven; Alivisatos, A. Paul. Colloidal synthesis of hollow cobalt sulfide nanocrystals. *Advanced Functional Materials* (2006), 16(11), 1389-1399.

92. Yin, Yadong; Rioux, Robert M.; Erdonmez, Can K.; Hughes, Steven; Somorjai, Gabor A.; Alivisatos, A. Paul., Formation of hollow nanocrystals through the nanoscale Kirkendall Effect. *Science* 2004, 304(5671), 711-714.

93. Borg, Richard J.; Dienes, G. J. An Introduction to Solid State Diffusion. Academic Press: Boston, 1988.

94. Lerme, J.; Celep, G.; Broyer, M.; Cottancin, E.; Pellarin, M.; Arbouet, A.; Christofilos, D.; Guillon, C.; Langot, P.; Del Fatti, N.; Vallee, F. Effects of confinement on the electron and lattice dynamics in metal nanoparticles. *European Physical Journal D* (2005), 34(1-3), 199-204.

95. Arbouet, A.; Voisin, C.; Christofilos, D.; Langot, P.; Del Fatti, N.; Vallee, F.; Lerme, J.; Celep, G.; Cottancin, E.; Gaudry, M.; Pellarin, M.; Broyer, M.; Maillard, M.; Pileni, M. P.; Treguer, M. Electron-Phonon Scattering in Metal Clusters. *Physical Review Letters* (2003), 90(17), 177401/1-177401/4.

96. Link, Stephan; El-Sayed, Mostafa A. Spectral Properties and Relaxation Dynamics of Surface Plasmon Electronic Oscillations in Gold and Silver Nano-dots and Nano-rods. *Journal of Physical Chemistry B* (1999), 103(40), 8410-8426.

97. Voisin, C.; Christofilos, D.; Loukakos, P. A.; Del Fatti, N.; Vallee, F.; Lerme, J.; Gaudry, M.; Cottancin, E.; Pellarin, M.; Broyer, M. Ultrafast electron-electron scattering and energy exchanges in noble-metal nanoparticles. *Physical Review B* (2004), 69(19), 195416/1-195416/13.

98. Christofilos D.; Voisin C.; Del Fatti N.; Vallée F. Femtosecond Nonlinear Optical Spectroscopy of the Acoustic Vibration of Metal Nanoparticles Under High Pressure. *International Journal of High Pressure Research* (2002), 22(2), 277-281.

99. Hartland, Gregory V. Coherent excitation of vibrational modes in metallic nanoparticles. *Annual Review of Physical Chemistry* (2006), 57, 403-430.

100. Hartland, Gregory V. Coherent vibrational motion in metal particles: Determination of the vibrational amplitude and excitation mechanism. *Journal of Chemical Physics* (2002), 116(18), 8048-8055.

101. Hartland, Gregory V.; Hu, Min; Wilson, Orla; Mulvaney, Paul; Sader, John E. Coherent Excitation of Vibrational Modes in Gold Nanorods. *Journal of Physical Chemistry B* (2002), 106(4), 743-747.

102. Zhu, Ting; Li, Ju; Samanta, Amit; Kim, Hyoung Gyu; Suresh, Subra. Interfacial plasticity governs strain rate sensitivity and ductility in nanostructured metals. *Proceedings of the National Academy of Sciences of the United States of America* (2007), 104(9), 3031-3036.

103. Krivtsov, A. M. Molecular Dynamics Simulation of Plastic Effects upon Spalling. *Physics of the Solid State* (2004), 46(6), 1055-1060.

104. Krivtsov, A. M.; Morozov, N. F. On Mechanical Characteristics of Nanocrystals.

Physics of the Solid State (2002), 44(12), 2260-2265.

105. Moriarty, John A.; Vitek, Vaclav; Bulatov, Vasily V.; Yip, Sidney. Atomistic simulations of dislocations and defects. *Journal of Computer-Aided Materials Design* (2003), 9(2), 99-132.

106. Moriarty, John A.; Xu, Wei; Soderlind, Per; Belak, James; Yang, Lin H.; Zhu, Jing. Atomistic simulations for multiscale modeling in bcc. metals. *Journal of Engineering Materials and Technology* (1999), 121(2), 120-125.

107. Zhao, Jing; Das, Aditi; Zhang, Xiaoyu; Schatz, George C.; Sligar, Stephen G.; Van Duyne, Richard P. Resonance Surface Plasmon Spectroscopy: Low Molecular Weight Substrate Binding to Cytochrome P450. *Journal of the American Chemical Society* (2006), 128(34), 11004-11005.

108. Haes, Amanda J.; Zou, Shengli; Zhao, Jing; Schatz, George C.; Van Duyne, Richard P. Localized Surface Plasmon Resonance Spectroscopy near Molecular Resonances. *Journal of the American Chemical Society* (2006), 128(33), 10905-10914.

109. Hicks, Erin M.; Zhang, Xiaoyu; Zou, Shengli; Lyandres, Olga; Spears, Kenneth G.; Schatz, George C.; Van Duyne, Richard P. Plasmonic Properties of Film over Nanowell Surfaces Fabricated by Nanosphere Lithography. *Journal of Physical Chemistry B* (2005), 109(47), 22351-22358.

110. Whitney, Alyson V.; Elam, Jeffrey W.; Zou, Shengli; Zinovev, Alex V.; Stair, Peter C.; Schatz, George C.; Van Duyne, Richard P. Localized Surface Plasmon Resonance Nanosensor: A High-Resolution Distance-Dependence Study Using Atomic Layer Deposition. *Journal of Physical Chemistry B* (2005), 109(43), 20522-20528.

111. Haes, Amanda J.; Haynes, Christy L.; McFarland, Adam D.; Schatz, George C.; van Duyne, Richard P.; Zou, Shengli. Plasmonic materials for surface-enhanced sensing and spectroscopy. *MRS Bulletin* (2005), 30(5), 368-375.

112. Haes, Amanda J.; Zou, Shengli; Schatz, George C.; Van Duyne, Richard P. Nanoscale Optical Biosensor: Short Range Distance Dependence of the Localized Surface Plasmon Resonance of Noble Metal Nanoparticles. *Journal of Physical Chemistry B* (2004), 108(22), 6961-6968.

113. Haes, Amanda J.; Zou, Shengli; Schatz, George C.; Van Duyne, Richard P. A Nanoscale Optical Biosensor: The Long Range Distance Dependence of the Localized Surface Plasmon Resonance of Noble Metal Nanoparticles. *Journal of Physical Chemistry B* (2004), 108(1), 109-116.

114. Malinsky, Michelle Duval; Kelly, K. Lance; Schatz, George C.; Van Duyne,

Richard P. Nanosphere Lithography: Effect of Substrate on the Localized Surface Plasmon Resonance Spectrum of Silver Nanoparticles. *Journal of Physical Chemistry B* (2001), 105(12), 2343-2350.

115. Malinsky, Michelle Duval; Kelly, K. Lance; Schatz, George C.; Van Duyne, Richard P. Chain length dependence and sensing capabilities of the localized surface plasmon resonance of silver nanoparticles chemically modified with alkanethiol self-assembled monolayers. *Journal of the American Chemical Society* (2001), 123(7), 1471-1482.

116. Chan, George H.; Zhao, Jing; Hicks, Erin M.; Schatz, George C.; Van Duyne, Richard P. Plasmonic Properties of Copper Nanoparticles Fabricated by Nanosphere Lithography. *Nano Letters* (2007), 7(7), 1947-1952.

117. Zhao, Jing; Jensen, Lasse; Sung, Jiha; Zou, Shengli; Schatz, George C.; Van Duyne, Richard P. Interaction of Plasmon and Molecular Resonances for Rhodamine 6G Adsorbed on Silver Nanoparticles. *Journal of the American Chemical Society* (2007), 129(24), 7647-7656.

118. Wang, Xiaoyong; Ren, Xiaofan; Kahen, Keith; Hahn, Megan A.; Rajeswaran, Manju; Maccagnano-Zacher, Sara; Silcox, John; Cragg, George E.; Efros, Alexander L.; Krauss, Todd D. Non-blinking semiconductor nanocrystals. *Nature* (2009), 459(7247), 686-689.

119. Bussian, David A.; Crooker, Scott A.; Yin, Ming; Brynda, Marcin; Efros, Alexander L.; Klimov, Victor I. Tunable magnetic exchange interactions in manganese-doped inverted core-shell ZnSe-CdSe nanocrystals. *Nature Materials* (2009), 8(1), 35-40.

120. Smith, Andrew M.; Mohs, Aaron M.; Nie, Shuming. Tuning the optical and electronic properties of colloidal nanocrystals by lattice strain. *Nature Nanotechnology* (2009), 4(1), 56-63.

121. Lal, Surbhi; Clare, Susan E.; Halas, Naomi J. Nanoshell-Enabled Photothermal Cancer Therapy: Impending Clinical Impact. *Accounts of Chemical Research* (2008), 41(12), 1842-1851.

122. Achermann, Marc; Petruska, Melissa A.; Kos, Simon; Smith, Darryl L.; Koleske, Daniel D.; Klimov, Victor I. Energy-transfer pumping of semiconductor nanocrystals using an epitaxial quantum well. *Nature* (2004), 429(6992), 642-646.

123. Hines, Margaret A.; Guyot-Sionnest, Philippe. Synthesis and Characterization of Strongly Luminescing ZnS-Capped CdSe Nanocrystals. *Journal of Physical Chemistry* (1996), 100(2), 468-471.

124. Li, J. Jack; Wang, Y. Andrew; Guo, Wenzhuo; Keay, Joel C.; Mishima, Tetsuya D.; Johnson, Matthew B.; Peng, Xiaogang. Large-Scale Synthesis of Nearly Monodisperse CdSe/CdS Core/Shell Nanocrystals Using Air-Stable Reagents via Successive Ion Layer Adsorption and Reaction. *Journal of the American Chemical Society* (2003), 125(41), 12567-12575.

125. Zeng, Hao; Li, Jing; Wang, Z. L.; Liu, J. P.; Sun, Shouheng. Bimagnetic Core/Shell FePt/Fe3O4 Nanoparticles. *Nano Letters* (2004), 4(1), 187-190.

126. Wang, Chao; Peng, Sheng; Chan, Ryan; Sun, Shouheng. Synthesis of AuAg alloy nanoparticles from core/shell-structured Ag/Au. *Small* (2009), 5(5), 567-570.

127. Shevchenko, Elena V.; Bodnarchuk, Maryna I.; Kovalenko, Maksym V.; Talapin, Dmitri V.; Smith, Rachel K.; Aloni, Shaul; Heiss, Wolfgang; Alivisatos, A. Paul. Gold/iron oxide core/hollow-shell nanoparticles. *Advanced Materials* (2008), 20(22), 4323-4329.

128. Lee, Jong-Soo; Shevchenko, Elena V.; Talapin, Dmitri V. Au-PbS Core-Shell Nanocrystals: Plasmonic Absorption Enhancement and Electrical Doping via Intra-particle Charge Transfer. *Journal of the American Chemical Society* (2008), 130(30), 9673-9675.

129. Xu, Zhichuan; Hou, Yanglong; Sun, Shouheng. Magnetic Core/Shell Fe3O4/Au and Fe3O4/Au/Ag Nanoparticles with Tunable Plasmonic Properties. *Journal of the American Chemical Society* (2007), 129(28), 8698-8699.

130. Kang, Shishou; Miao, G. X.; Shi, S.; Jia, Z.; Nikles, David E.; Harrell, J. W. Enhanced Magnetic Properties of Self-Assembled FePt Nanoparticles with MnO Shell. *Journal of the American Chemical Society* (2006), 128(4), 1042-1043.

131. Wilcoxon, Jess Patrick; Provencio, Paula P. Heterogeneous growth of metal clusters from solutions of seed nanoparticles. *Journal of the American Chemical Society* (2004), 126(20), 6402-6408.

132. Wang, Xun; Zhuang, Jing; Peng, Qing; Li, Yadong. A general strategy for nanocrystal synthesis. *Nature* (2005), 437(7055), 121-124.

133. Chandran, S. Prathap; Ghatak, J.; Satyam, P. V.; Sastry, Murali. Interfacial deposition of Ag on Au seeds leading to AucoreAgshell in organic media. *Journal of Colloid and Interface Science* (2007), 312(2), 498-505.

134. Kim, Hyungrak; Achermann, Marc; Balet, Laurent P.; Hollingsworth, Jennifer A.; Klimov, Victor I. Synthesis and Characterization of Co/CdSe Core/Shell Nanocomposites: Bifunctional Magnetic-Optical Nanocrystals. *Journal of the American Chemical Society* (2005), 127(2), 544-546.

135. Iglesias, Oscar; Batlle, Xavier; Labarta, Amilcar. Exchange bias and asymmetric hysteresis loops from a microscopic model of core/shell nanoparticles. *Journal of Magnetism and Magnetic Materials* (2007), 316(2), 140-142.

136. Abe, Masanori; Suwa, Takeshi. Surface plasma resonance and magneto-optical enhancement in composites containing multicore-shell structured nanoparticles. *Physical Review B* (2004), 70(23), 235103/1-235103/15.

137. Chen, Xi; Sahoo, S.; Kleemann, W.; Cardoso, S.; Freitas, P. P. Universal and scaled relaxation of interacting magnetic nanoparticles. *Physical Review B* (2004), 70(17), 172411/1-172411/4.

138. Allia, Paolo; Coisson, Marco; Tiberto, Paola; Vinai, Franco; Knobel, Marcelo; Novak, M. A.; Nunes, W. C. Granular Cu-Co alloys as interacting superparamagnets. *Physical Review B* (2001), 64(14), 144420/1-144420/12.

139. Mikhaylova, Maria; Kim, Do Kyung; Bobrysheva, Natalia; Osmolowsky, Mikhail; Semenov, Valentin; Tsakalakos, Thomas; Muhammed, Mamoun. Superparamagnetism of Magnetite Nanoparticles: Dependence on Surface Modification. *Langmuir* (2004), 20(6), 2472-2477.

140. Kechrakos, D.; Trohidou, K. N. Magnetic properties of self-assembled interacting nanoparticles. *Applied Physics Letters* (2002), 81(24), 4574-4576.

141. Liu, Feng; Press, M. R.; Khanna, S. N.; Jena, P. Magnetism and local order: Ab initio tight-binding theory. *Physical Review B* (1989), 39(10-B), 6914-6924.

142. Tolbert, S. H.; Alivisatos, A. P. Size dependence of a first order solid-solid phase transition: the Wurtzite to rock salt transformation in CdSe nanocrystals. *Science* (1994), 265(5170), 373-376.

143. Tolbert, Sarah H.; Alivisatos, A. P. The wurtzite to rock salt structural transformation in CdSe nanocrystals under high pressure. *Journal of Chemical Physics* (1995), 102(11), 4642-56.

144. Wickham, Juanita N.; Herhold, Amy B.; Alivisatos, A. P. Shape change as an indicator of mechanism in the high-pressure structural transformations of CdSe nanocrystals. *Physical Review Letters* (2000), 84(5), 923-926.

145. Awschalom, David D.; Loss, Daniel; Samarth, Nitin. Semiconductor Spintronics and Quantum Computation. Springer-Verlag: Berlin, 2002.

146. Wong, Cathy Y.; Kim, Jeongho; Nair, P. Sreekumari; Nagy, Michelle C.; Scholes, Gregory D. Relaxation in the Exciton Fine Structure of Semiconductor Nanocrystals. *Journal of Physical Chemistry C* (2009), 113(3), 795-811.

147. Gupta, J. A.; Awschalom, D. D.; Efros, Al. L.; Rodina, A. V. Spin dynamics in semiconductor nanocrystals. *Physical Review B* (2002), 66(12), 125307/1-125307/12.

148. Ouyang, Min; Awschalom, David D. Coherent Spin Transfer Between Molecularly Bridged Quantum Dots. *Science* (2003), 301(5636), 1074-1078.

149. Hemley, R. J.; Chiarotti, G. L. High Pressure Phenomena. (Proceedings of the International School of Physics "Enrico Fermi" Course CXLVII held 3-13 July 2001 in Varenna, Italy.) IOS Press: Amsterdam, 2002.

150. Efros, Al. L.; Rosen, M. The electronic structure of semiconductor nanocrystals. *Annual Review of Materials Science* (2000), 30, 475-521.

151. Efros, Al. L.; Rosen, M.; Kuno, M.; Nirmal, M.; Norris, D. J.; Bawendi, M. Band-edge exciton in quantum dots of semiconductors with a degenerate valence band: dark and bright exciton states. *Physical Review B* (1996), 54(7), 4843-4856.

152. Limpijumnong, Sukit; Jungthawan, Sirichok. First-principles study of the wurtzite-to-rocksalt homogeneous transformation in ZnO: a case of a low-transformation barrier. *Physical Review B* (2004), 70(5), 054104/1- 054104/4.

153. Sowa, H. A transition path for the pressure-induced wurtzite- to NaCl-type transformation described in Pna2(1). *Acta Crystallographica A* (2005), A61(3), 325-330.

154. Zahn, Dirk; Grin, Yuri; Leoni, Stefano. Mechanism of the pressure-induced wurtzite to rocksalt transition of CdSe. *Physical Review B* (2005), 72(6), 064110/1-064110/7.

155. Wilson, Mark; Hutchinson, Francis; Madden, Paul A. Simulation of pressure-driven phase transitions from tetrahedral crystal structures. *Physical Review B* (2002), 65(9), 094109/1-094109/15.

156. Catti, Michele. First-principles study of the orthorhombic mechanism for the B3/B1 high-pressure phase transition of ZnS. *Physical Review B* (2002), 65(22), 224115/1-224115/8.

157. Grunwald, Michael; Rabani, Eran; Dellago, Christoph. Mechanisms of the Wurtzite to Rocksalt Transformation in CdSe Nanocrystals. *Physical Review Letters* (2006), 96(25), 255701/1-255701/4.

158. Limpijumnong, Sukit; Lambrecht, Walter R. L. Theoretical study of the relative stability of wurtzite and rocksalt phases in MgO and GaN. *Physical Review B*

(2001), 63(10), 104103/1-104103/11.

159. Miao, M. S.; Lambrecht, Walter R. L. Universal Transition State for High-Pressure Zinc Blende to Rocksalt Phase Transitions. *Physical Review Letters* (2005), 94(22), 225501/1-225501/4.

160. Shimojo, Fuyuki; Kodiyalam, Sanjay; Ebbsjo, Ingvar; Kalia, Rajiv K.; Nakano, Aiichiro; Vashishta, Priya. Atomistic mechanisms for wurtzite-to-rocksalt structural transformation in cadmium selenide under pressure. *Physical Review B* (2004), 70(18), 184111/1-184111/6.

161. Knudson, M. D.; Gupta, Y. M. Transformation kinetics for the shock wave induced phase transition in cadmium sulfide crystals. *Journal of Applied Physics* (2002), 91(12), 9561-9571.

162. Sharma, Surinder M.; Gupta, Y. M. Wurtzite-to-rocksalt structural transformation in cadmium sulfide shocked along the a axis. *Physical Review B* (1998), 58(10), 5964-5971.

163. Tang, Z. P.; Gupta, Y. M. Phase transition in cadmium sulfide single crystals shocked along the c axis. *Journal of Applied Physics* (1997), 81(11), 7203-7212.

164. Kiselev, A. A.; Ivchenko, E. L.; Rossler, U. Electron g factor in one- and zero-dimensional semiconductor nanostructures. *Physical Review B* (1998), 58(24), 16353-16359.

165. Kapustina, A. B.; Petrov, B. V.; Rodina, A. V.; Seisyan, R. P. Magnetic absorption of hexagonal crystals CdSe in strong and weak fields. Quasi-cubic approximation. *Physics of the Solid State* (2000), 42(7), 1242-1252.

166. Li, Jingbo; Li, Guo-Hua; Xia, Jian-Bai; Zhang, Jing-Bo; Lin, Yuan; Xiao, Xu-Rui. Optical spectra of CdSe nanocrystals under hydrostatic pressure. *Journal of Physics* (2001), 13(9), 2033-2043.

167. Berezovsky, Jesse; Ouyang, Min; Meier, Florian; Awschalom, David D.; Battaglia, David; Peng, Xiaogang. Spin dynamics and level structure of quantum-dot quantum wells. *Physical Review B* (2005), 71(8), 081309/1-081309/4.

168. Schrier, Joshua; Whaley, K. Birgitta. Tight-binding g-factor calculations of CdSe nanostructures. *Physical Review B* (2003), 67(23), 235301/1-235301/9.

169. Meier, Florian; Awschalom, David D. Faraday rotation spectroscopy of quantum-dot quantum wells. *Physical Review B* (2005), 71(20), 205315/1-205315/9.

170. Nahalkova, P.; Sprinzl, D.; Maly, P.; Nemec, P.; Gladilin, V. N.; Devreese, J. T. Two-phonon assisted exciton spin relaxation due to exchange interaction in spherical quantum dots. *Physical Review B* (2007), 75(11), 113306/1-113306/4.

171. Fu, Huaxiang; Wang, Lin-Wang; Zunger, Alex. Excitonic exchange splitting in bulk semiconductors. *Physical Review B* (1999), 59(8), 5568-5574.

172. Kato, Y.; Myers, R. C.; Gossard, A. C.; Awschalom, D. D. Coherent spin manipulation without magnetic fields in strained semiconductors. *Nature* (2004), 427(6969), 50-53.

173. Gupta, J. A.; Awschalom, D. D.; Efros, Al. L.; Rodina, A. V. Spin dynamics in semiconductor nanocrystals. *Physical Review B* (2002), 66(12), 125307/1-125307/12.

174. Rodina, A. V.; Efros, Al. L.; Alekseev, A. Yu. Effect of the surface on the electron quantum size levels and electron g factor in spherical semiconductor nanocrystals. *Physical Review B* (2003), 67(15), 155312/1-155312/11.

175. Gupta, J.A. Coherence and manipulation of spin states in semiconductor nanostructures, PhD. Thesis, University of California at Santa Barbara, 2002.

176. Grimvall, Goran. Selected Topics in Solid-State Physics, Vol. 16: The Electron-Phonon Interaction in Metals. North-Holland: Amsterdam, 1981.

177. Fackler, J. P.; Liu, C. W. Product class 5: organometallic complexes of silver. *Science of Synthesis* (2004), 3, 663-690.

178. Zheng, Jie; Ding, Yong; Tian, Bozhi; Wang, Zhong Lin; Zhuang, Xiaowei. Luminescent and Raman Active Silver Nanoparticles with Polycrystalline Structure. *Journal of the American Chemical Society* (2008), 130(32), 10472-10473.

179. Schatz, George C.; Young, Matthew A.; Van Duyne, Richard P. Electromagnetic mechanism of SERS. *Topics in Applied Physics* (2006), 103, 19-46.